Supporting Information for

Stimuli-responsive anion transport utilising caged hydrazone-based anionophores

Manzoor Ahmad[a], Martin Flerin[a], Hui Min Tay[a], Amber L. Thompson[a], Fernanda Duarte*[a] and Matthew J. Langton*[a]

Contents

I. Materials and methods

All reagents and solvents were purchased from commercial sources and used without further purification. Lipids were purchased from Avanti polar lipids and used without further purification. Column chromatography was carried out on Merck® silica gel 60 under a positive pressure of nitrogen. Where mixtures of solvents were used, ratios are reported by volume. NMR spectra were recorded on a Bruker AVIII 400, Bruker AVII 500 (with cryoprobe) and Bruker AVIII 500 spectrometers. Chemical shifts are reported as δ values in ppm. Mass spectra were carried out on a Waters Micromass LCT and Bruker microTOF spectrometers. UV-Vis spectra were recorded on a V-770 UV-Visible/NIR Spectrophotometer equipped with a Peltier temperature controller and stirrer, using quartz cuvettes of 1 cm path length. Fluorescence spectroscopic data were recorded using Agilent fluorescence spectrophotometer, equipped with Peltier temperature controller and stirrer. Experiments were conducted at 25°C unless otherwise stated. Vesicles were prepared as described below using Avestin "LiposoFast" extruder apparatus, equipped with polycarbonate membranes with 200 nm pores. GPC purification of vesicles was carried out using GE Healthcare PD-10 desalting columns prepacked with Sephadex G 25 medium. HPLC analysis were carried out using a Thermo Scientific Vanquish Core HPLC and a C-18 reverse phase column (Ascentis, 5 µm, 15 cm x 4.6 mm).

Abbreviations

DCM: Dichloromethane; **DMF:** *N*, *N*-Dimethylformamide; **THF:** Tetrahydrofuran; **DMSO:** Dimethylsulfoxide; **DPPC:** 1,2-dipalmitoyl-sn-glycero-3-phosphocholine; **EYPG:** egg-yolk phosphatidylglycerol; **HRMS:** High resolution mass spectrometry; **LUVs:** large unilamellar vesicles; **MeOH:** Methanol; **POPC:** 1-palmitoyl-2-oleoyl-sn-glycero-3-phosphocholine; rt: Room temperature; **TBACl:** Tetrabutylammonium chloride.

II. Synthesis

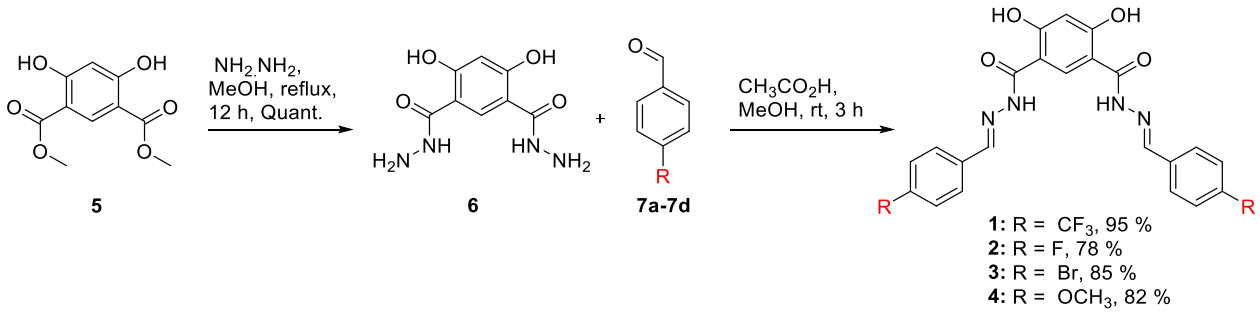

Scheme 1. Chemical synthesis of compounds **1-4**.

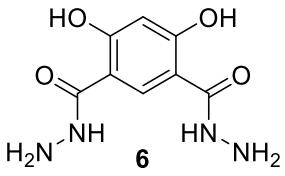

$C_8H_{10}N_4O_4$
Mol. Wt.: 226.19

4, 6-dihydroxyisophthalohydrazide (6): In a 25 mL round bottom flask, dimethyl 4,6-dihydroxyisophthalate **5** (200 mg, 0.88 mmol, 1.0 eq) was refluxed in a mixture of hydrazine hydrate (1.0 mL, 6.63 mmol, 10.0 eq) and methanol (20 mL) for 12 h. The mixture was then allowed to come to room temperature and white solid precipitated out was collected by vacuum filtration to give compound **6** in quantitative yield. 200 mg. **^{1}H NMR (400 MHz, DMSO)** δ 8.30 (s, 1H), 6.63 (s, 8H), 6.00 (s, 1H); **^{13}C NMR (126 MHz, DMSO)** δ 168.4, 167.0, 130.0, 107.0, 104.9; **HRMS (ESI) *m/z*:** $[M+H]^+$ Calcd. for $C_8H_{10}N_4O_4H^+$ 227.0775; Found 227.0738.

General procedure for the synthesis of compounds 1-4:

In a 25 mL round bottom flask, 4, 6-dihydroxyisophthalohydrazide **6** (50 mg, 0.22 mmol, 1 eq) and different aromatic aldehydes (0.44 mmol, 2 eq) were dissolved in a mixture of methanol (20 mL) and acetic acid (1 mL). The reaction was allowed to stir at rt for 3 h. The white precipitate was formed in all the cases which was filtered under vacuum filtration, washed with diethyl ether and pentane to give **1-4** in excellent yields.

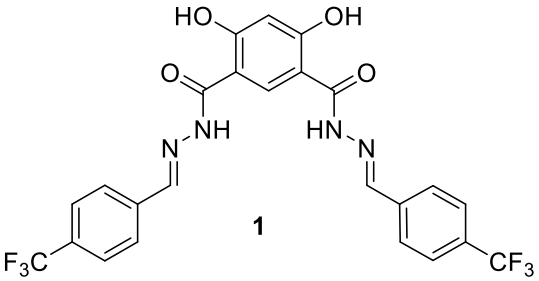

$C_{24}H_{16}F_6N_4O_4$

4,6-dihydroxy-*N*'1, *N*'3-bis((E)-4-(trifluoromethyl)benzylidene)isophthalohydrazide (1): This compound was synthesized by reacting 4, 6-dihydroxyisophthalohydrazide **6** (50 mg, 0.22 mmol, 1 eq) with 4-Trifluoromethybenzaldehyde **7a** (76 mg, 0.44 mmol, 2 equiv). Yield: 95%, 113 mg. **^{1}H NMR (600 MHz, DMSO)** δ 12.35 (s, 2H), 11.94 (s, 2H), 8.55 (s, 3H), 7.97 (d, J = 8.2 Hz, 4H), 7.84 (d, J = 8.3 Hz, 4H), 6.54 (s, 1H); **^{13}C NMR (151 MHz, DMSO)** δ 164.2, 163.3, 146.9, 138.6, 132.5, 130.5-

129.9 (q, *J* = 31.7 Hz) 128.2, 127.2-121.8 (q, *J* = 271 Hz), 126.2-126.1 (q, *J* = 4.5 Hz), 109.9, 104.0; **HRMS (ESI) *m/z*:** $[M+H]^+$ Calcd. for $C_{24}H_{16}F_6N_4O_4H^+$ 539.1149; Found 539.1161.

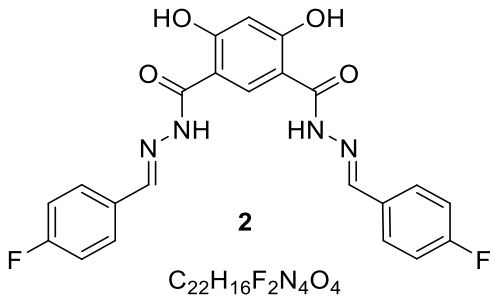

2

$C_{22}H_{16}F_2N_4O_4$

***N*'1, *N*'3-bis((E)-4-fluorobenzylidene)-4,6-dihydroxyisophthalohydrazide (2):** This compound was synthesized by reacting 4, 6-dihydroxyisophthalohydrazide **6** (50 mg, 0.22 mmol, 1 eq) with 4-fluoromethybenzaldehyde **7b** (55 mg, 0.44 mmol, 2 equiv). Yield: 78%, 75 mg. **^{1}H NMR (600 MHz, DMSO)** δ 12.29 (s, 2H), 11.78 (s, 2H), 8.52 (s, 1H), 8.46 (s, 2H), 7.87 – 7.76 (m, 4H), 7.31 (t, *J* = 8.8 Hz, 4H), 6.51 (s, 1H). **^{13}C NMR (151 MHz, DMSO)** δ 164.4, 164.2 (d, J = 117.8 Hz), 162.8, 147.6, 132.0, 131.2, 129.8 (d, J = 10 Hz) 116.4 (d, J = 21.1 Hz), 109.7, 103.9; **HRMS (ESI) *m/z*:** $[M+H]^+$ Calcd. for $C_{22}H_{16}F_2N_4O_4H^+$ 439.1212; Found 439.1204.

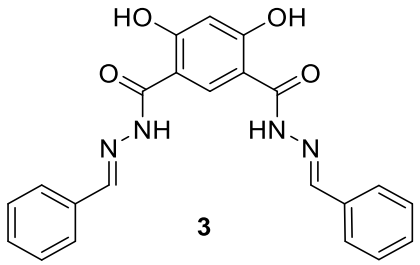

3

$C_{22}H_{18}N_4O_4$

***N*'1, *N*'3-di((E)-benzylidene)-4,6-dihydroxyisophthalohydrazide (3)**: This compound was synthesized by reacting 4, 6-dihydroxyisophthalohydrazide **6** (50 mg, 0.22 mmol, 1 eq) with benzaldehyde **7c** (47 mg, 0.44 mmol, 2 equiv). Yield: 85%, 75 mg. **^{1}H NMR (600 MHz, DMSO)** δ 12.43 (br s, 2H), 11.80 (s, 2H), 8.54 (s, 1H), 8.47 (s, 2H), 7.76 (d, *J* = 7.2 Hz, 4H), 7.50-7.45 (m, 6H), 6.51 (s, 1H); **^{13}C NMR (151 MHz, DMSO)** δ 164.3, 163.5, 148.7, 134.6, 131.9, 130.6, 129.3, 127.6, 109.6, 104.0; **HRMS (ESI) *m/z*:** $[M+H]^+$ Calcd. for $C_{22}H_{18}N_4O_4H^+$ 403.1401; Found 403.1405.

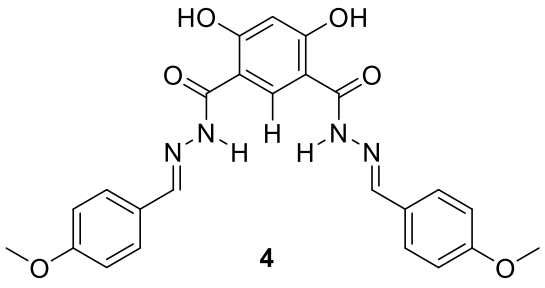

4

$C_{24}H_{22}N_4O_6$

4,6-dihydroxy-*N*'1, *N*'3-bis((E)-4-methoxybenzylidene)isophthalohydrazide (4): This compound was synthesized by reacting 4, 6-dihydroxyisophthalohydrazide **6** (50 mg, 0.22 mmol, 1 eq) with 4-Methoxybenzaldehyde **7d** (60 mg, 0.44 mmol, 2 equiv). Yield: 82%, 84 mg. **^{1}H NMR (600 MHz, DMSO)** δ 12.47 (br s, 2H), 11.71 (s, 2H), 8.52 (s, 1H), 8.40 (s, 2H), 7.70 (d, *J* = 8.6 Hz, 4H), 7.04 (d, *J* = 8.7 Hz, 4H), 6.48 (s, 1H), 3.82 (s, 6H); **^{13}C NMR (151 MHz, DMSO)** δ 164.24, 163.68, 161.44,

148.64, 131.64, 129.31, 127.20, 114.86, 109.47, 104.01, 55.80; **HRMS (ESI) *m/z*:** $[M+H]^+$ Calcd. for $C_{30}H_{36}N_2O_4H^+$ 463.1612; Found 463.1616.

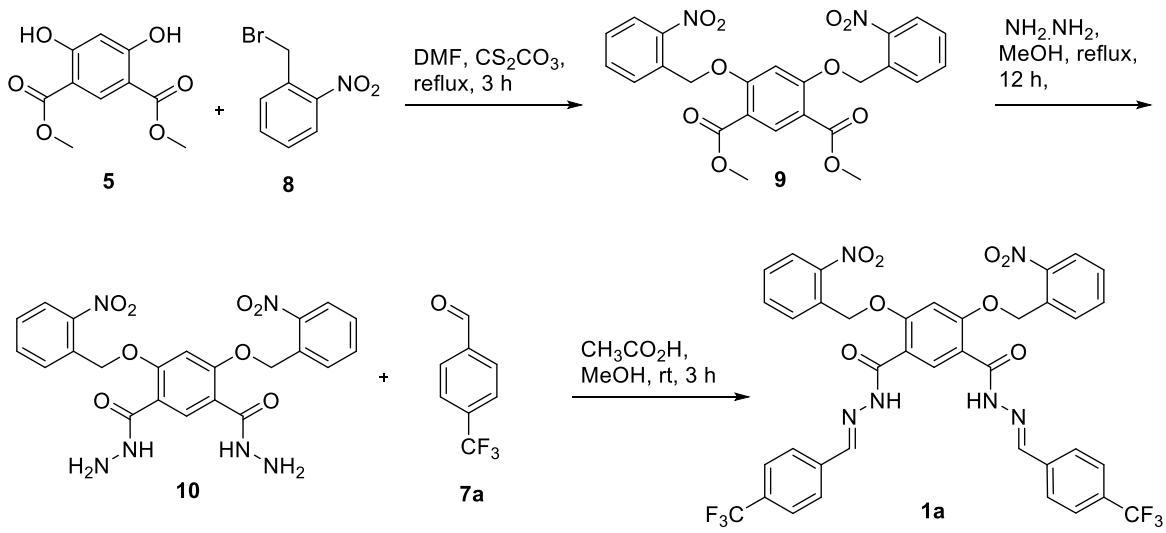

Scheme 2. Chemical synthesis for protransporter **1a.**

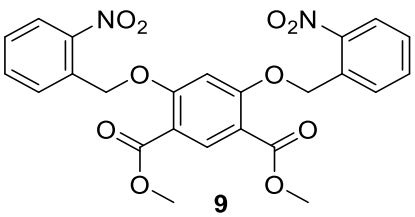

$C_{24}H_{20}N_2O_{10}$

Dimethyl 4,6-bis((2-nitrobenzyl)oxy)isophthalate (9): In a 25 mL round bottom flask, 4,6-dihydroxyisophthalate **5** (50 mg, 0.22 mmol, 1 eq) and 1-(bromomethyl)-2-nitrobenzene **8** (95 mg, 0.44 mmol, 2.0 eq) were dissolved in DMF (10 mL). Caesium carbonate (60 mg, 0.44 mmol, 2.0 eq) was added and the reaction mixture was refluxed for 3 h. After that, water (10 mL) was added to the reaction and the white precipitate formed was collected through vacuum filtration, washed with diethyl ether, pentane to get compound **9** in excellent yield. Yield: 95%, 103 mg. **^{1}H NMR (400 MHz, $CDCl_3$)** δ 8.56 (s, 1H), 8.19 (d, J = 7.9 Hz, 2H), 8.15 (d, J = 8.2 Hz, 2H), 7.71 (t, J = 7.6 Hz, 2H), 7.49 – 7.42 (m, 2H), 6.68 (s, 1H), 5.56 (s, 4H), 3.86 (s, 6H); **^{13}C NMR (176 MHz, DMSO)** δ 164.7, 162.4, 147.3, 136.5, 134.7, 132.3, 129.7, 129.5, 125.4, 112.1, 100.0, 67.9, 52.4; **HRMS (ESI) *m/z*:** $[M+H]^+$ Calcd. for $C_{24}H_{20}N_2O_{10}H^+$ 497.1191; Found 497.1185.

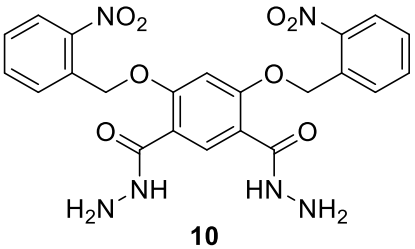

$C_{22}H_{20}N_6O_8$

4,6-bis((2-nitrobenzyl)oxy)isophthalohydrazide (10): In a 25 mL round bottom flask, Dimethyl 4,6-bis((2-nitrobenzyl)oxy)isophthalate **9** (100 mg, 0.26 mmol) was dissolved in a mixture of hydrazine

hydrate (8 mL) and methanol (50 mL). The reaction mixture was refluxed for 48 h. After completion of the reaction, the solvent was removed under rotary evaporator. To remove the excess of hydrazine hydrate, toluene was added to form an azeotropic mixture that was concentrated under high vacuum at 70 ºC. The crude reaction mixture was used for the next reaction without any purification.

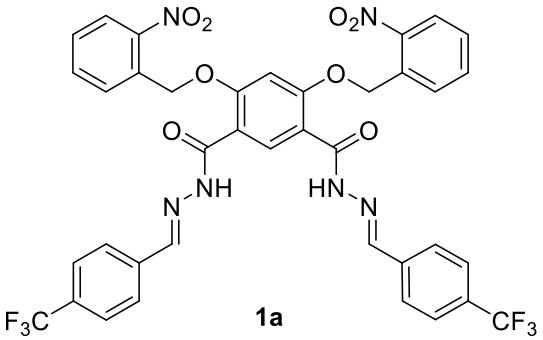

1a

$C_{38}H_{26}F_6N_6O_8$

4,6-bis((2-nitrobenzyl)oxy)-N'1,N'3-bis((E)-4-(trifluoromethyl) benzylidene)isophthalohydrazide (1a): In a 25 mL round bottom flask, 4,6-bis((2-nitrobenzyl)oxy)isophthalohydrazide **10** (crude mixture, 100 mg, 0.20 mmol, 1 eq) and 4-trifluoromethylbenzaldehyde **7a** (70 mg, 0.40 mmol, 2.0 eq) were dissolved in a mixture of methanol (20 mL) and acetic acid (1 mL) and the reaction was allowed to stir for 3 h at room temperature. After the completion of the reaction, excess of solvent was removed under rotary evaporator and the crude was extracted with water (30 mL) and ethyl acetate (20 mL × 3). The organic layers were collected and dried with magnesium sulphate. The solvent was removed and the crude mixture was purified by column chromatography over silica gel (*Eluent*: 2% methanol in dichloromethane) to furnish **1a** as a white solid. Yield: 40%, 60 mg. **^{1}H NMR (400 MHz, CD_3CN)** δ 10.71 (s, 2H), 8.73 (s, 1H), 8.15 (d, *J* = 7.9 Hz, 2H), 8.07 (s, 2H), 7.88 (d, *J* = 8.6 Hz, 4H), 7.77 (d, *J* = 8.6 Hz, 4H), 7.72-7.68 (m, 3H), 7.64-7.59 (m, 3H), 6.69 (s, 1H), 5.78 (s, 4H); **^{1}H NMR (500 MHz, DMSO, 80 °C)** δ 11.47 (s, 2H), 8.23 (s, 2H), 8.08 (bs, 2H), 7.76 (bs, 13H), 7.59 (bs, 2H), 6.95 (s, 1H), 5.68 (s, 4H);); **^{19}F NMR (377 MHz, DMSO-d_6)** δ -60.93; **HRMS (ESI) *m/z*:** $[M+H]^+$ Calcd. for $C_{38}H_{26}F_6N_6O_8H^+$ 809.1789; Found 809.1820.

Note: The compound **1a** exits as different rotamers in DMSO-d_6 at 25 °C in slow exchange as suggested by the ^{1}H NMR spectrum where small other peaks are visible. At high temperature however the spectrum should simplify, and we observed only single peaks at 80 °C in the fast exchange regime, confirming that the compound exists in different conformations rather than a mixture of different compounds. Moreover, we also observed that such a process of mixed conformations is solvent dependent – the ^{1}H NMR in actenonitrile-d_3 shows only single peaks. We were unable to obtain a ^{13}C NMR spectrum, despite use of a cryoprobe, due to low solubility and precipitation of the sample. However, identity and purity are confirmed by ^{1}H NMR, high resolution mass spectrometry and the X-ray crystal structure.

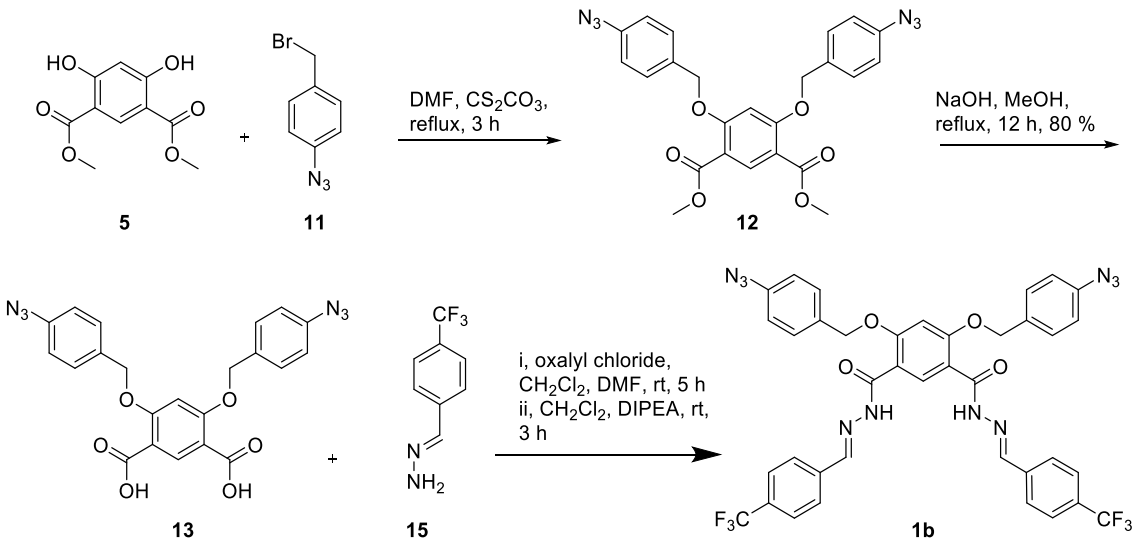

Scheme 3. Chemical synthesis for protransporter **1b.**

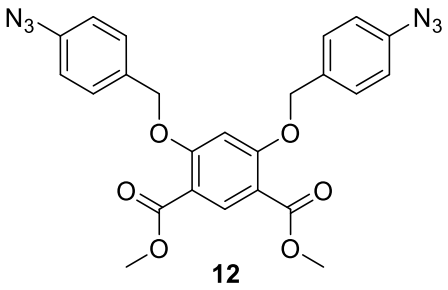

$C_{24}H_{20}N_6O_6$

Dimethyl 4,6-bis((4-azidobenzyl)oxy)isophthalate (12): In a 25 mL round bottom flask, 4,6-dihydroxyisophthalate **5** (100 mg, 0.44 mmol, 1 eq) and 1-azido-4-(bromomethyl)benzene **11**, that itself was synthesized according to the literature procedure[1] (187 mg, 0.88 mmol, 2.0 equiv) were dissolved in DMF (10 mL). Caesium carbonate (120 mg, 0.88 mmol, 2.0 equiv) was added and the reaction mixture was refluxed for 3 h. After that, water (10 mL) was added to the reaction and the white precipitate formed was collected through vacuum filtration, washed with diethyl ether, pentane to get compound **12** in excellent yield. Yield: 88%, 189 mg. ^{1}H NMR (400 MHz, DMSO) δ 8.27 (s, 1H), 7.55 (d, *J* = 8.4 Hz, 4H), 7.17 (d, *J* = 8.4 Hz, 4H), 7.00 (s, 1H), 5.33 (s, 4H), 3.79 (s, 6H); **^{13}C NMR (126 MHz, DMSO)** δ 164.8, 162.8, 139.3, 136.1, 133.6, 129.2, 119.6, 112.0, 100.3, 70.0, 52.2; **HRMS (ESI) *m/z*:** $[M+Na]^+$ Calcd. for $C_8H_{10}N_4O_4Na^+$ 511.1337; Found 511.1340.

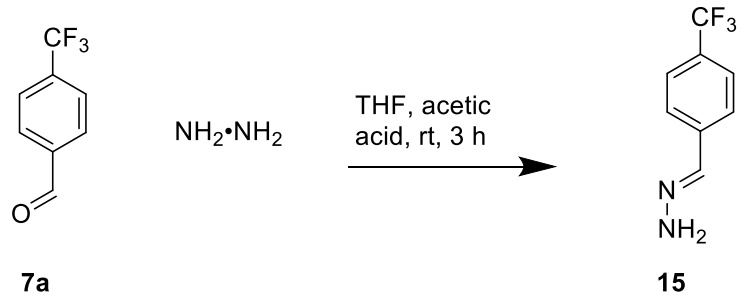

(E)-(4-(trifluoromethyl)benzylidene)hydrazine (15): In a 25 mL round bottom flask, 4-Trifluoromethy **7a** (100 mg, 0.57 mmol, 1 eq) and hydrazine hydrate as 1M solution in THF (2.3 mL,

2.3 mmol, 4 eq) were dissolved in tetrahydrofuran (10 mL). To this mixture acetic acid (1 mL) was added and the reaction was stirred at rt for 3 h. After the completion of the reaction, monitored by TLC, the solvent was removed under rotary evaporator and the crude mixture was extracted with CH_2Cl_2 (20 mL × 3) and dried on magnesium sulphate. The solvent was removed and the crude mixture was used directly without any purification.

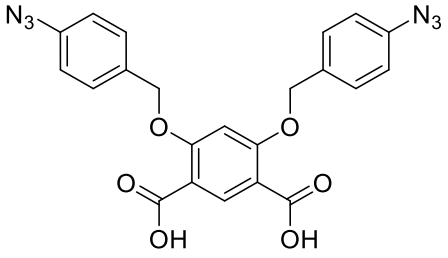

13

$C_{22}H_{16}N_6O_6$

4,6-bis((4-azidobenzyl)oxy)isophthalic acid (13): In a 25 mL round bottom flask, Dimethyl 4,6-bis((4-azidobenzyl)oxy)isophthalate **12** (100 mg, 0.20 mmol) was dissolved in a mixture of Methanol (10 mL), tetrahydrofuran (10 mL), and aqueous sodium hydroxide (2 N, 5 mL). The reaction was refluxed for 12 h at 70 ºC. After the completion of the reaction, monitored by TLC, the solvent was removed under rotary evaporator. The mixture was then acidified by the addition of HCl (2 N) dropwise. The white precipitate formed was collected by vacuum filtration, washed with diethyl ether and pentane to furnish the compound 13 in excellent yield. Yield: 90%, 85 mg. **^{1}H NMR (400 MHz, DMSO)** δ 12.52 (s, 2H), 8.24 (s, 1H), 7.54 (d, *J* = 8.6 Hz, 4H), 7.15 (d, *J* = 8.6 Hz, 4H), 6.93 (s, 1H), 5.30 (s, 4H); **^{13}C NMR (126 MHz, DMSO)** δ 166.2, 162.3, 139.3, 136.4, 133.8, 129.3, 119.6, 113.1, 100.2, 69.8; **HRMS (ESI) *m/z*:** $[M+Na]^+$ Calcd. for $C_8H_{10}N_4O_4Na^+$ 483.1024; Found 483.1020.

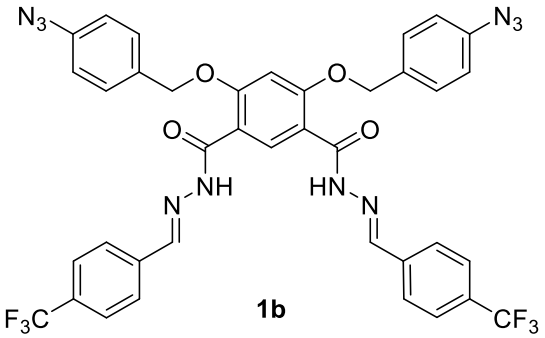

1b

$C_{38}H_{26}F_6N_{10}O_4$

4,6-bis((4-azidobenzyl)oxy)-N'1,N'3-bis((E)-4-(trifluoromethyl)benzylidene)isophthalohydrazide (1b): In an oven dry 25 mL round bottom flask, 4,6-bis((4-azidobenzyl)oxy)isophthalic acid **13** (50 mg, 0.10 mmol, 1 eq) was dissolved in dry Tetrahydrofuran (20 mL). Three drops of DMF were added to the mixture. After that, oxalyl chloride (0.42 mL, 5.43 mmol, 50.0 eq) was added and reaction was stirred at rt for 5 h. After the completion of the reaction, solvent and excess of oxalyl chloride were evaporated under rotary evaporator. The crude was dissolved in dry Tetrahydrofuran (10 mL). **15** (60 mg, 0.30 mmol, 3 eq) and DIPEA (28 mg, 0.21 mmol, 2 eq) were added and the reaction mixture was allowed to stir at rt for 3 h. After the completion of the reaction, excess of solvent was removed under rotary evaporator and the crude was extracted with ethyl acetate (20 mL × 3). The organic layers were collected and dried with magnesium sulphate. The solvent was removed and the crude mixture was purified by column chromatography over silica gel (*Eluent*: 2% methanol in dichloromethane) to furnish

1b as a white solid. Yield: 60%, 51 mg. **^{1}H NMR (500 MHz, DMSO, at 80 °C)** δ 11.42 (s, 2H), 8.20 (s, 2H), 7.88-7.11 (m, 8H), 7.53 (s, 4H), 7.37 (s, 1H), 7.15-7.02 (m, *J* = 27.9 Hz, 5H), 5.35 (s, 4H); **^{19}F NMR (377 MHz, DMSO-d_6)** δ -61.82; **HRMS (ESI) *m/z*:** $[M+H]^+$ Calcd. for $C_{38}H_{26}F_6N_{10}O_4H^+$ 809.1789; Found 809.1820.

Note: As in case of compound **1a**, compound **1b** also exits as different rotamers in DMSO-d_6 at 25 °C. To confirm we again performed a hight temperature analysis and it was observed that the NMR peaks resolved to single peaks at 80 °C. Furthermore, as for **1b**, ^{13}C NMR could not be performed due to low solubility.

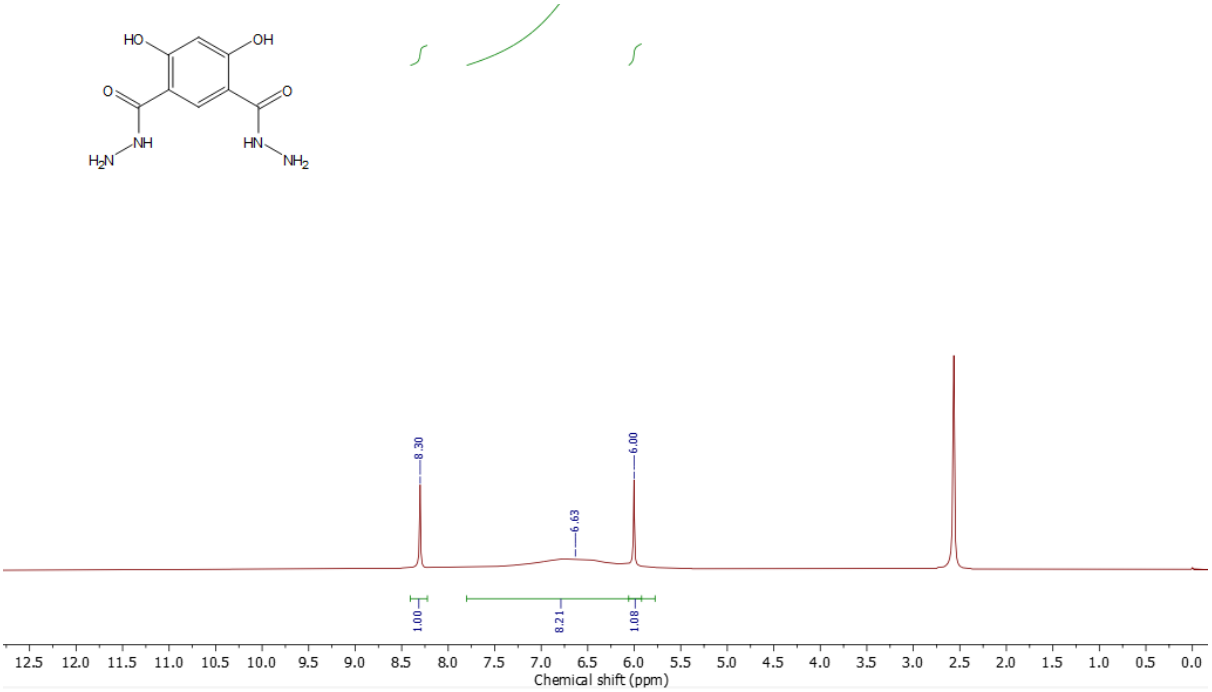

Figure S1: ^{1}H NMR Spectrum of **6** in DMSO-d_6, 298 K

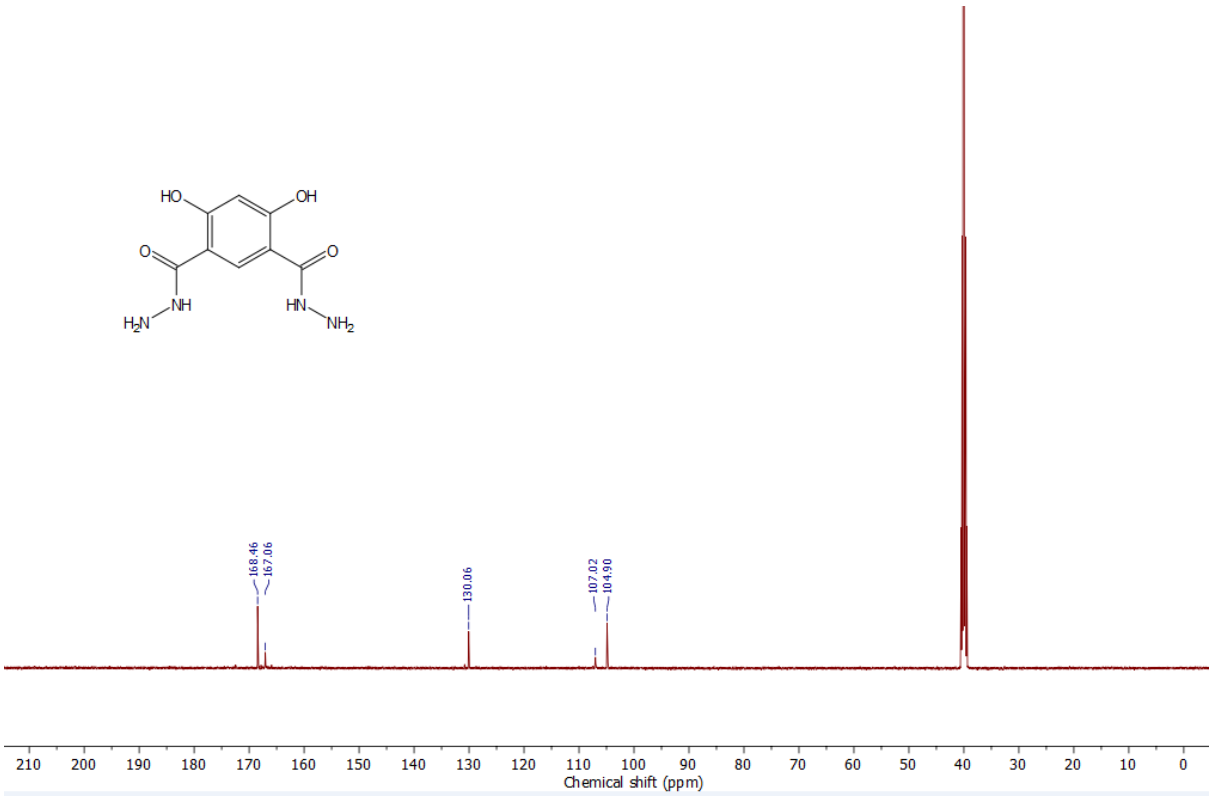

Figure S2: ^{13}C NMR Spectrum of **6** in DMSO-d_6, 298 K

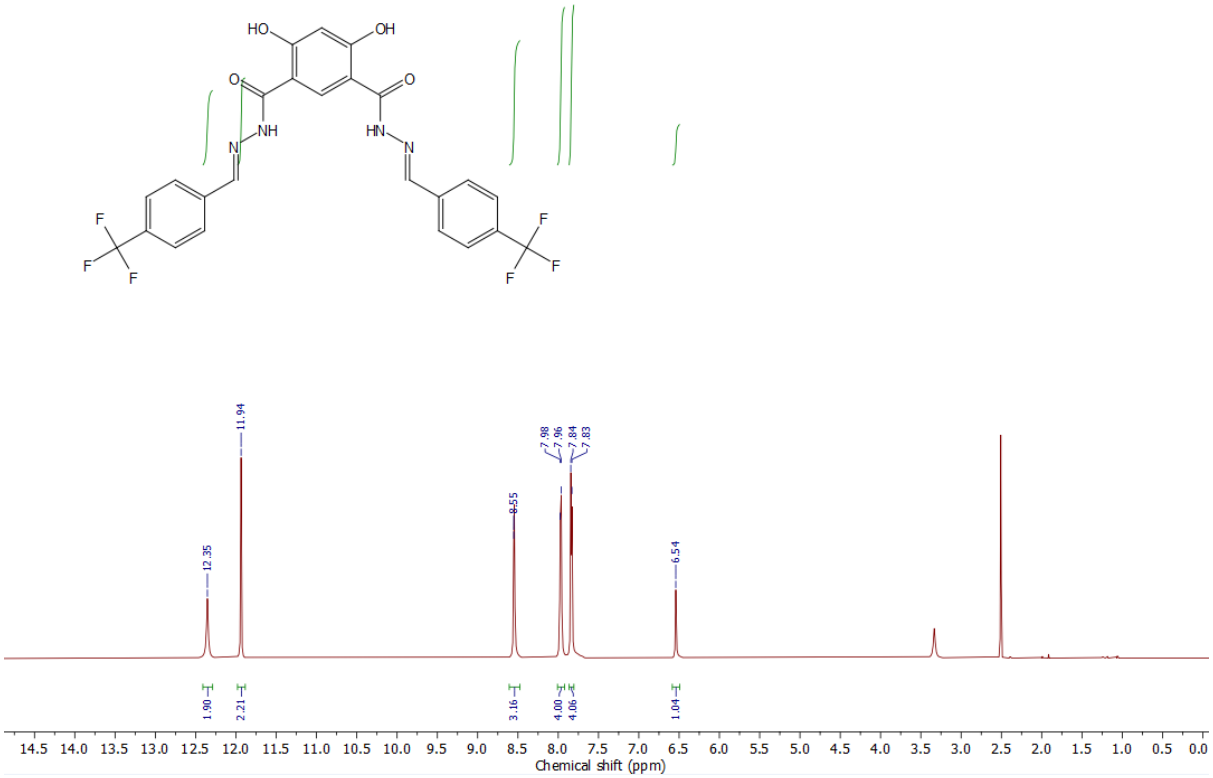

Figure S3: ^{1}H NMR Spectrum of **1** in DMSO-d_6, 298 K

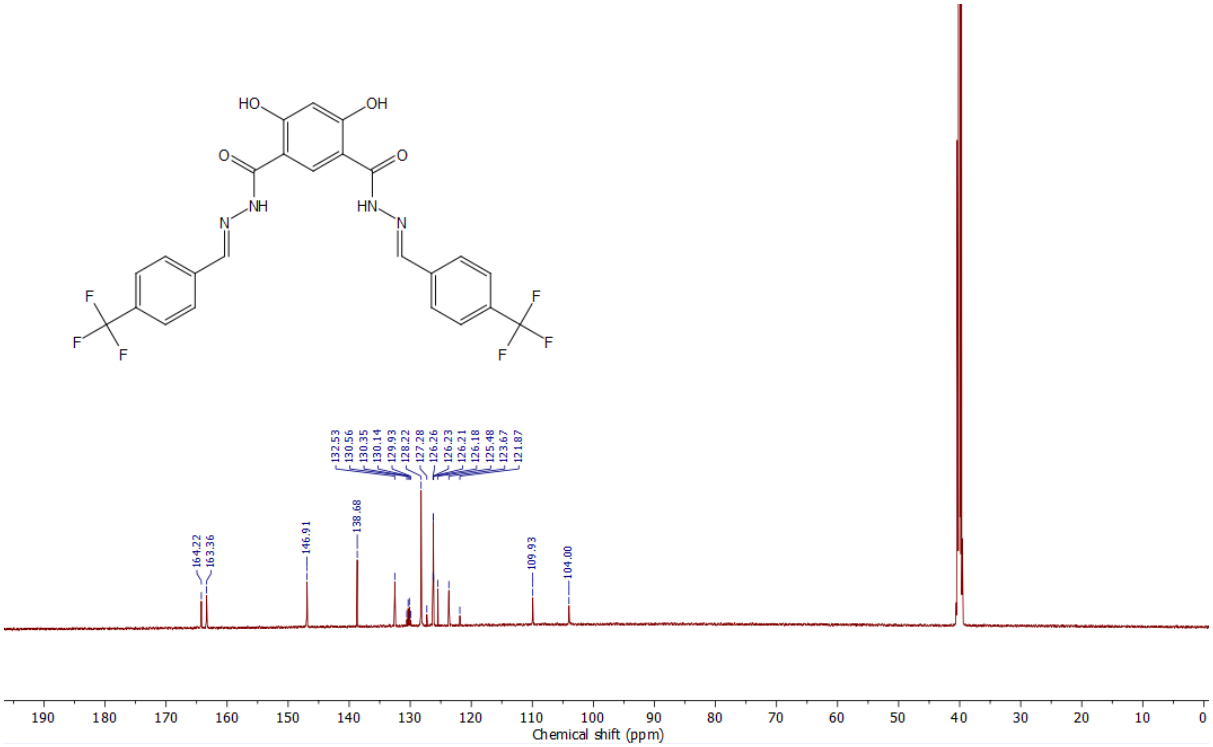

Figure S4: ^{13}C NMR Spectrum of **1** in DMSO-d_6, 298 K

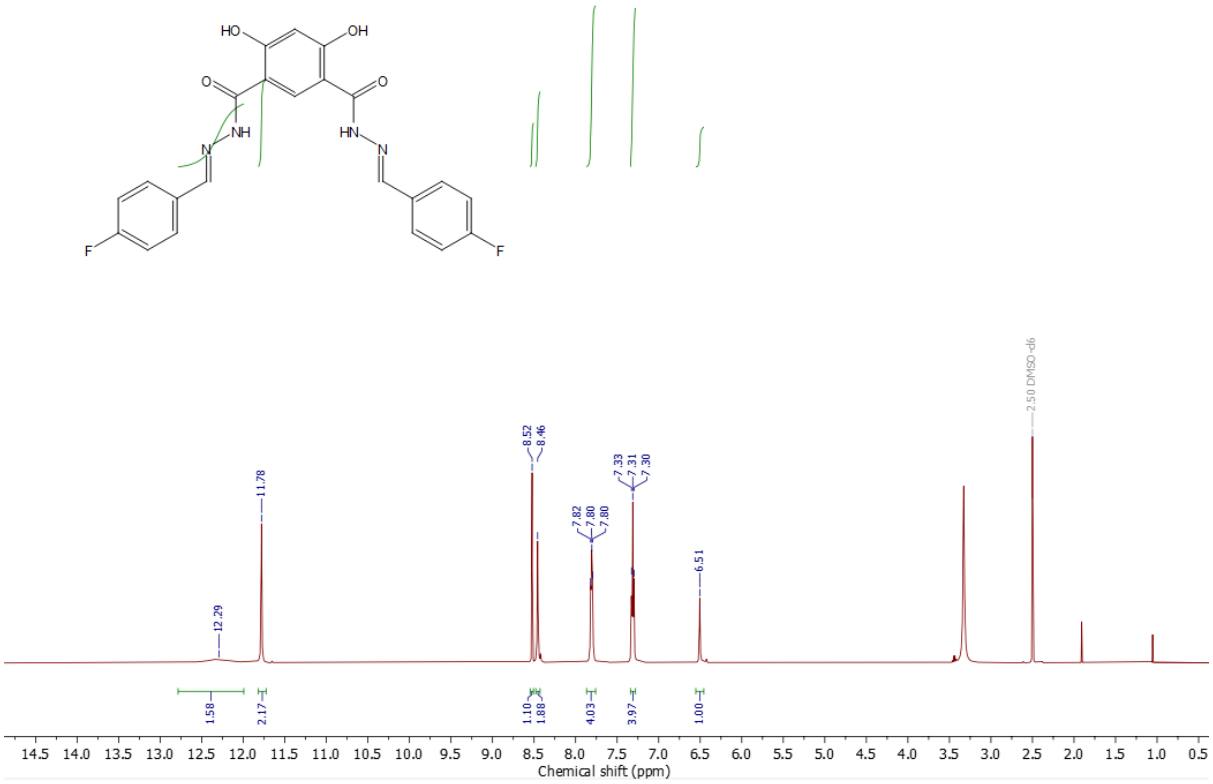

Figure S5: ^{1}H NMR Spectrum of **2** in DMSO-d_6, 298 K

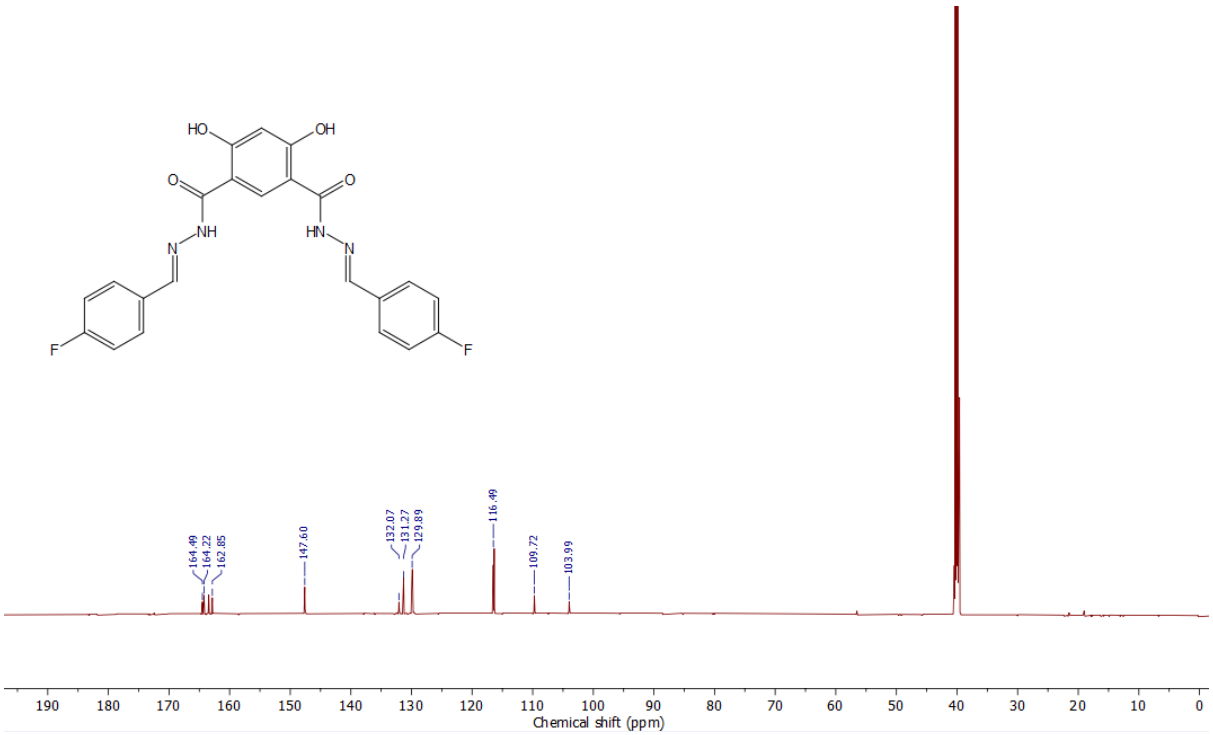

Figure S6: ^{13}C NMR Spectrum of **2** in DMSO-d_6, 298 K

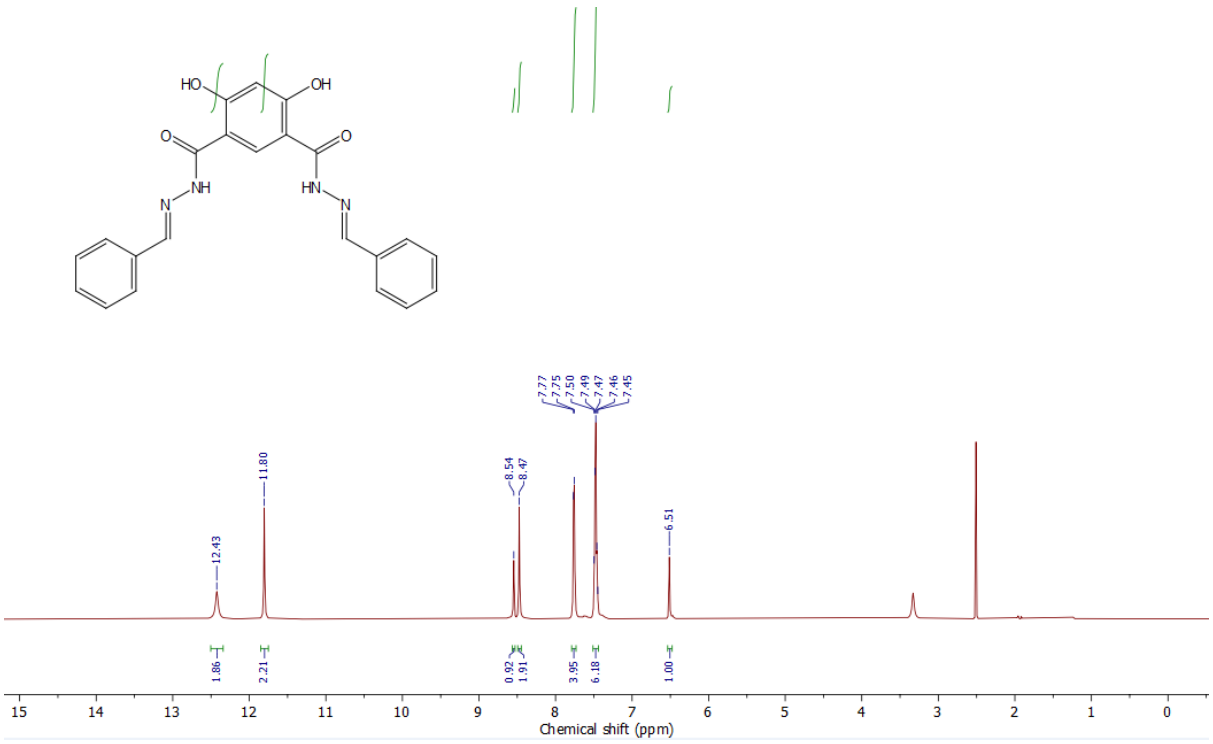

Figure S7: ^{1}H NMR Spectrum of **3** in DMSO-d_6, 298 K

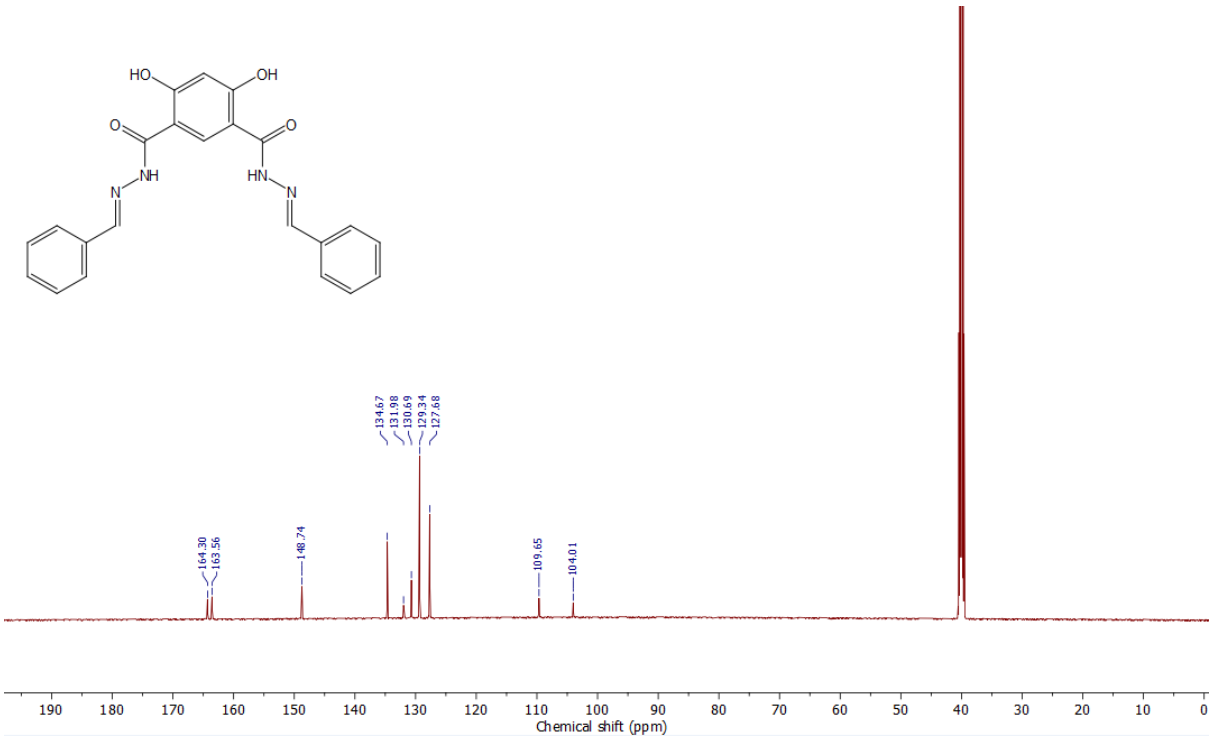

Figure S8: ^{13}C NMR Spectrum of **3** in DMSO-d_6, 298 K

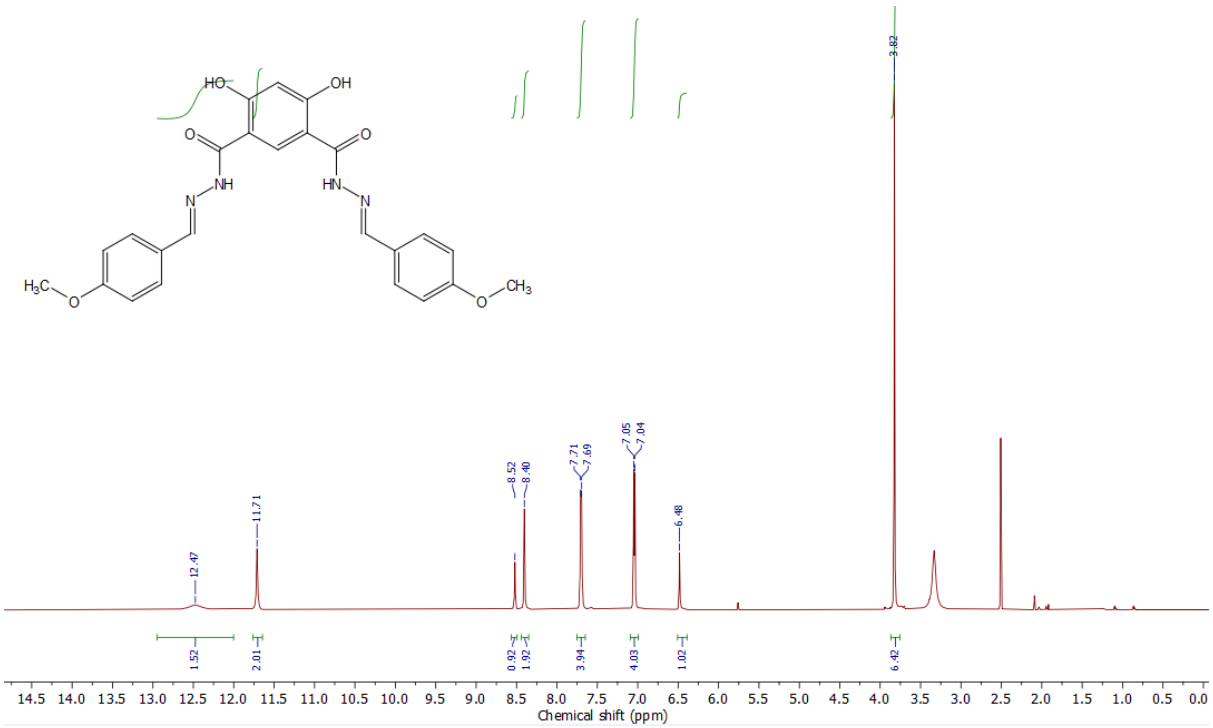

Figure S9: ^{1}H NMR Spectrum of **4** in DMSO-d_6, 298 K

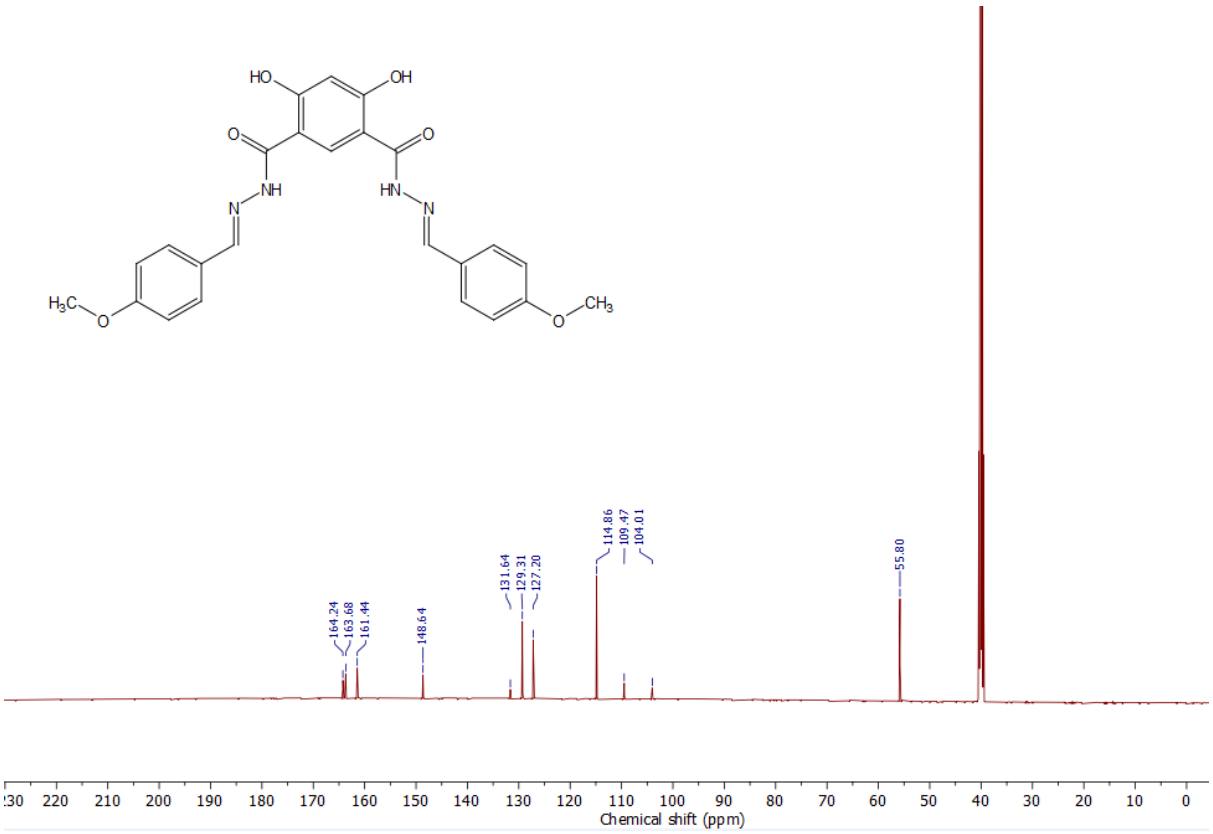

Figure S10: ^{13}C NMR Spectrum of **4** in DMSO-d_6, 298 K

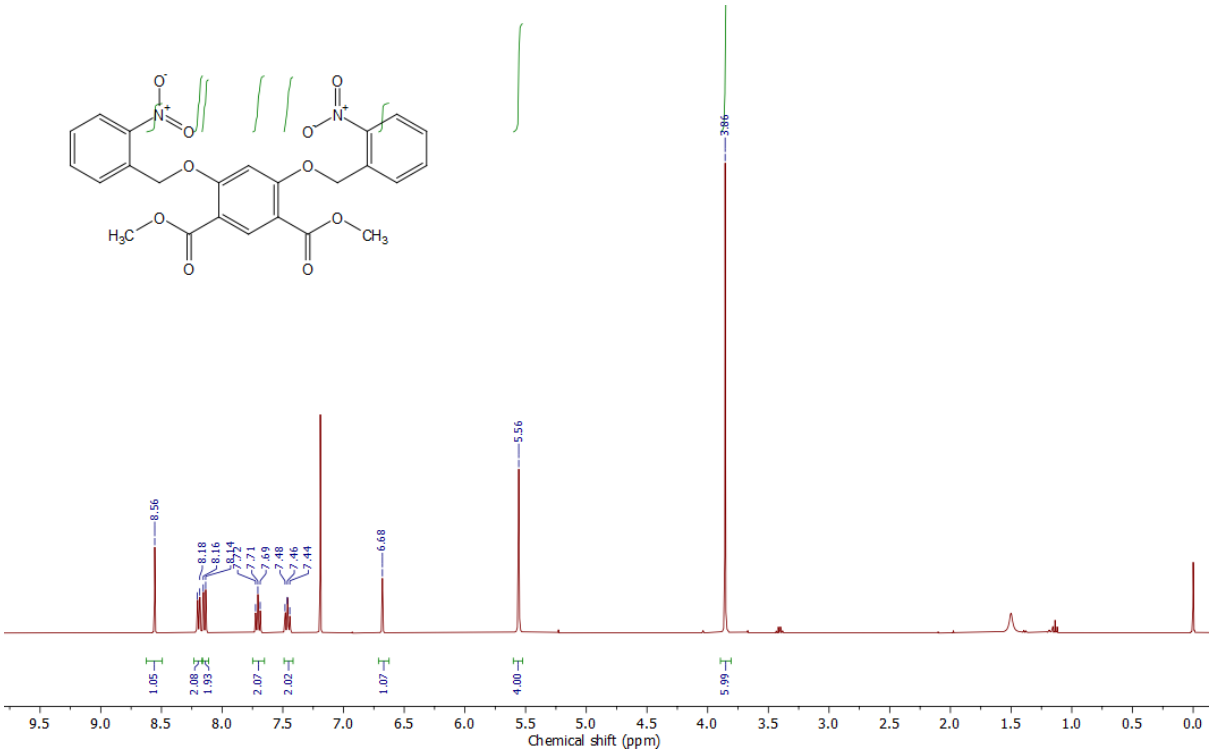

Figure S11: ^{1}H NMR Spectrum of **9** in $CDCl_3$, 298 K

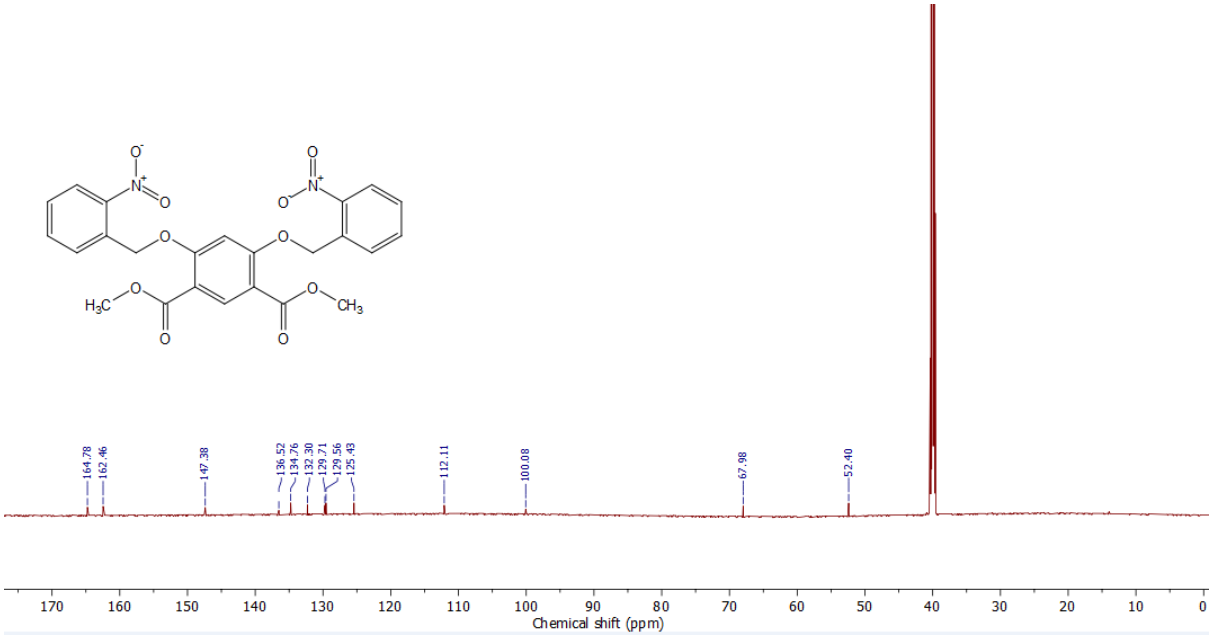

Figure S12: ^{13}C NMR Spectrum of **9** in DMSO-d_6, 298 K

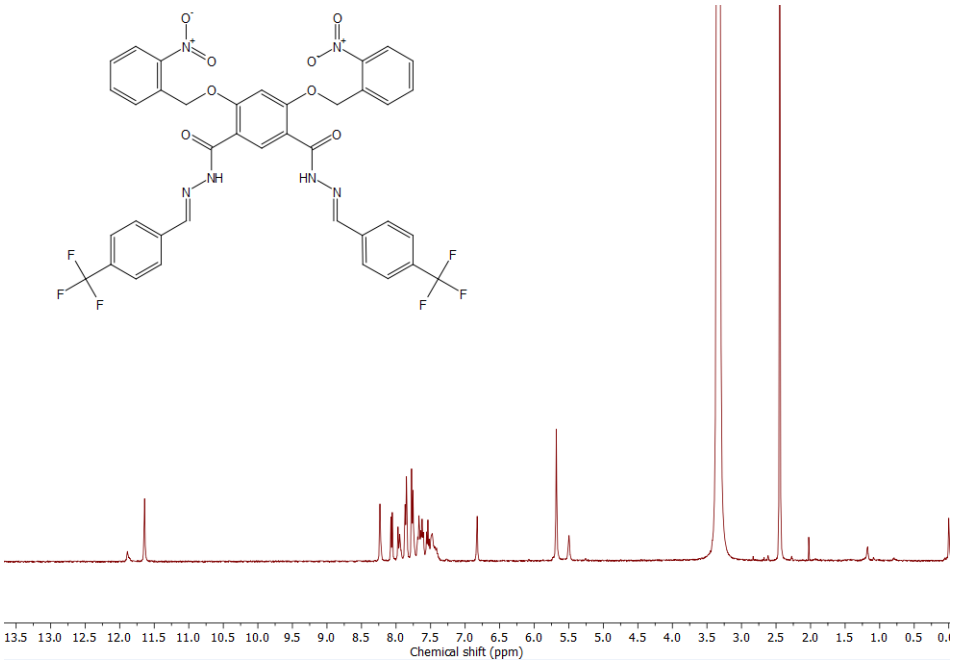

Figure S13: ^{1}H NMR Spectrum of **1a** in DMSO-d_6, 298 K

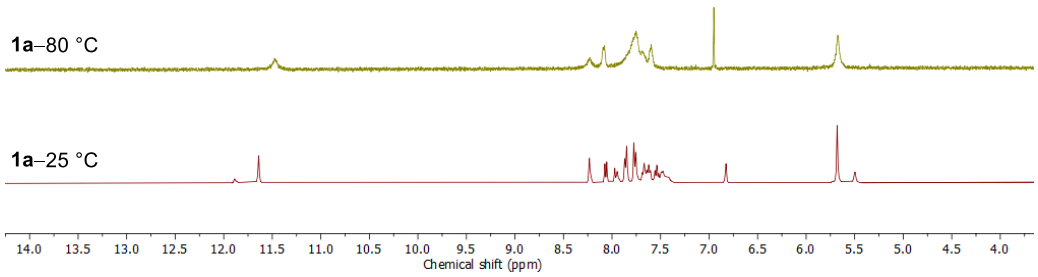

Figure S14: ^{1}H NMR Spectrum of **1a** in DMSO-d_6, at 25°C and 80°C 298 K

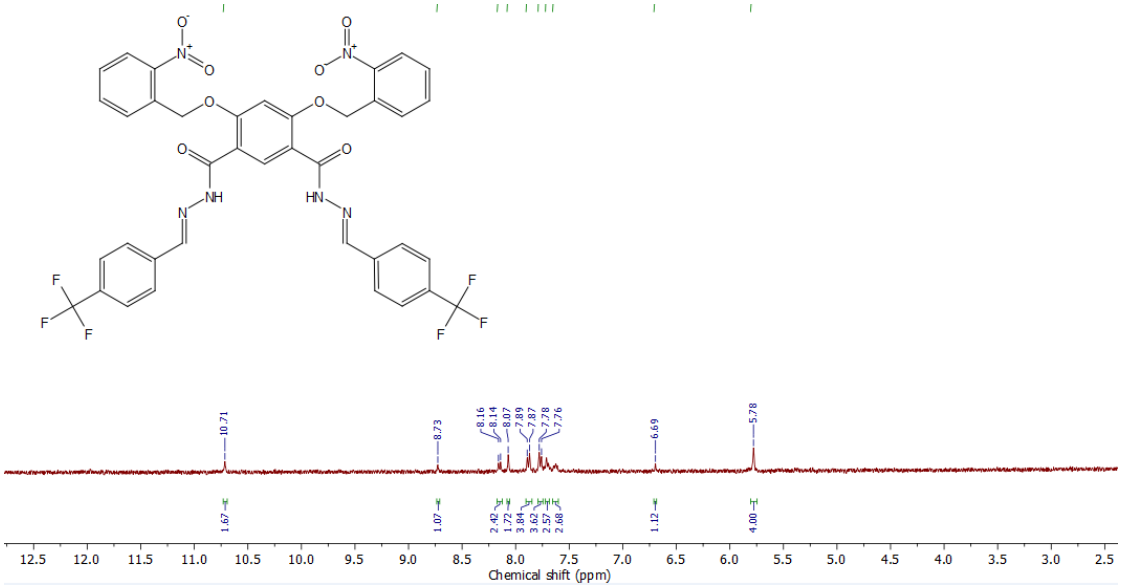

Figure S15: ^{1}H NMR Spectrum of **1a** in CD_3CN, 298 K

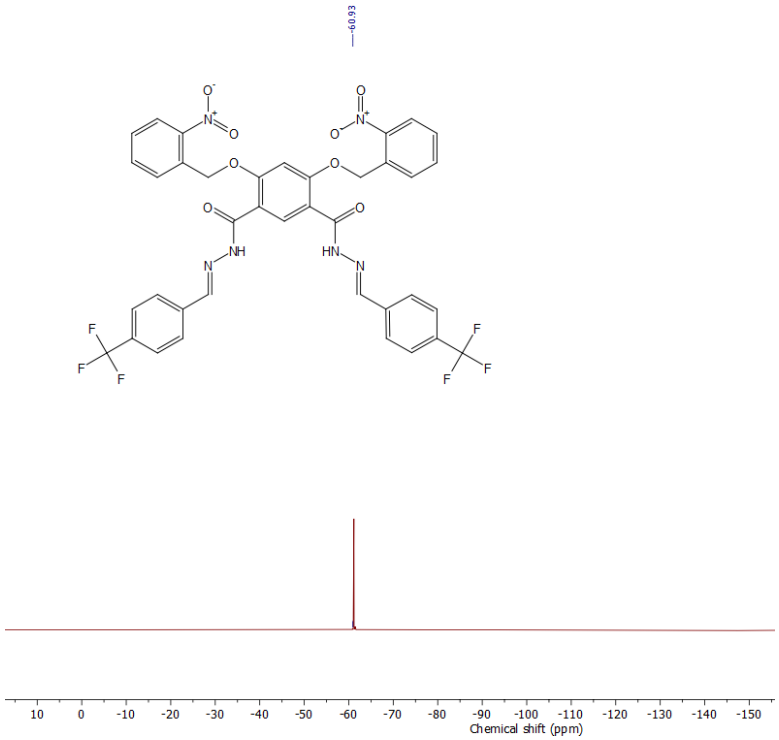

Figure S16: ^{19}F NMR Spectrum of **1a** in DMSO-d_6, 298 K.

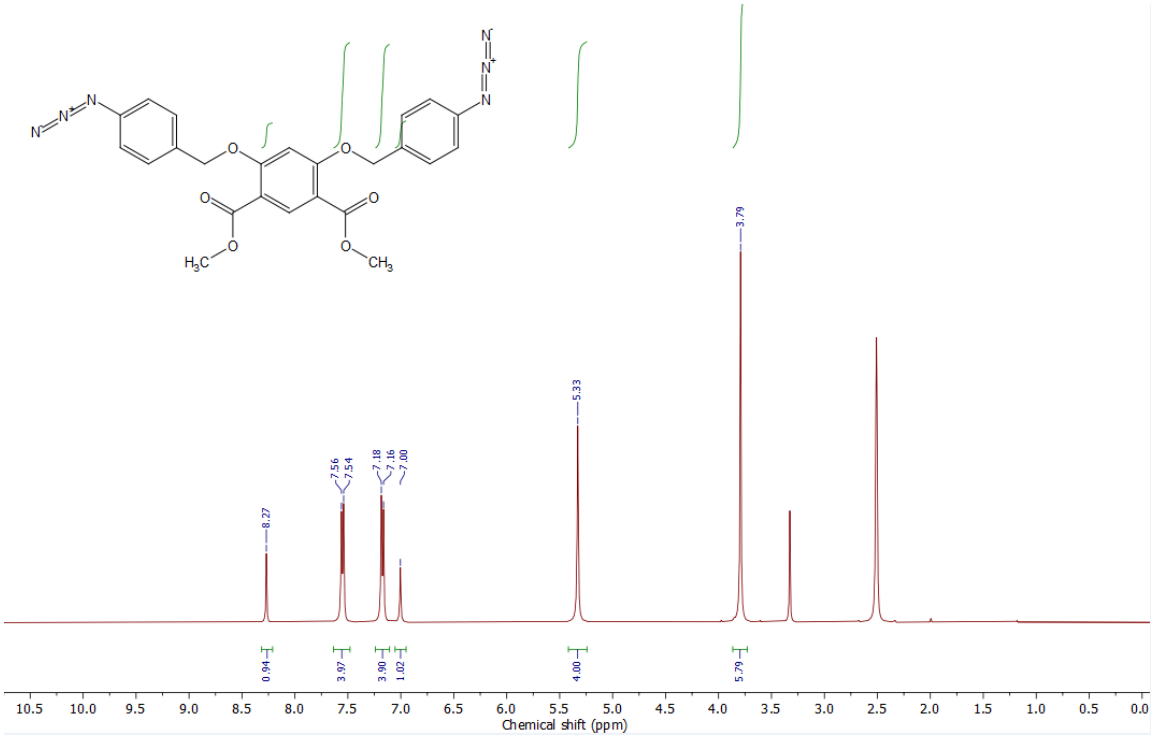

Figure S17: ^{1}H NMR Spectrum of **12** in DMSO-d_6, 298 K

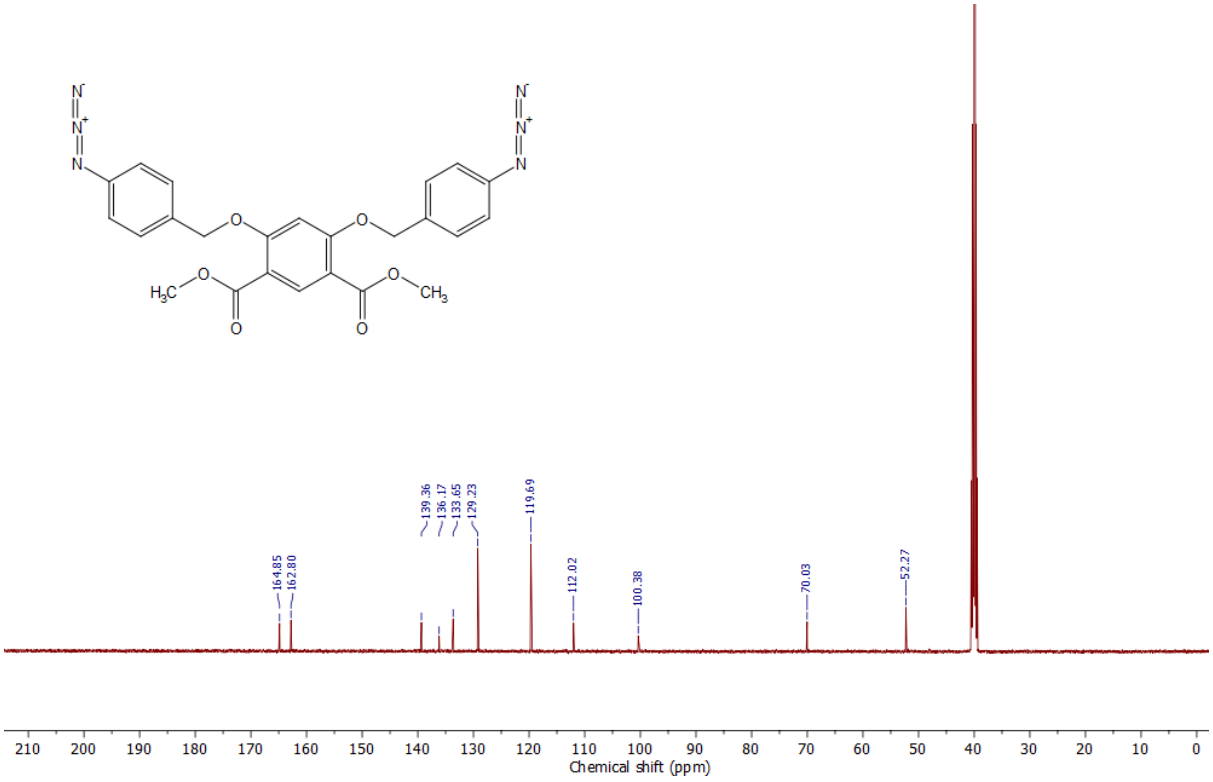

Figure S18: ^{13}C NMR Spectrum of **12** in DMSO-d_6, 298 K

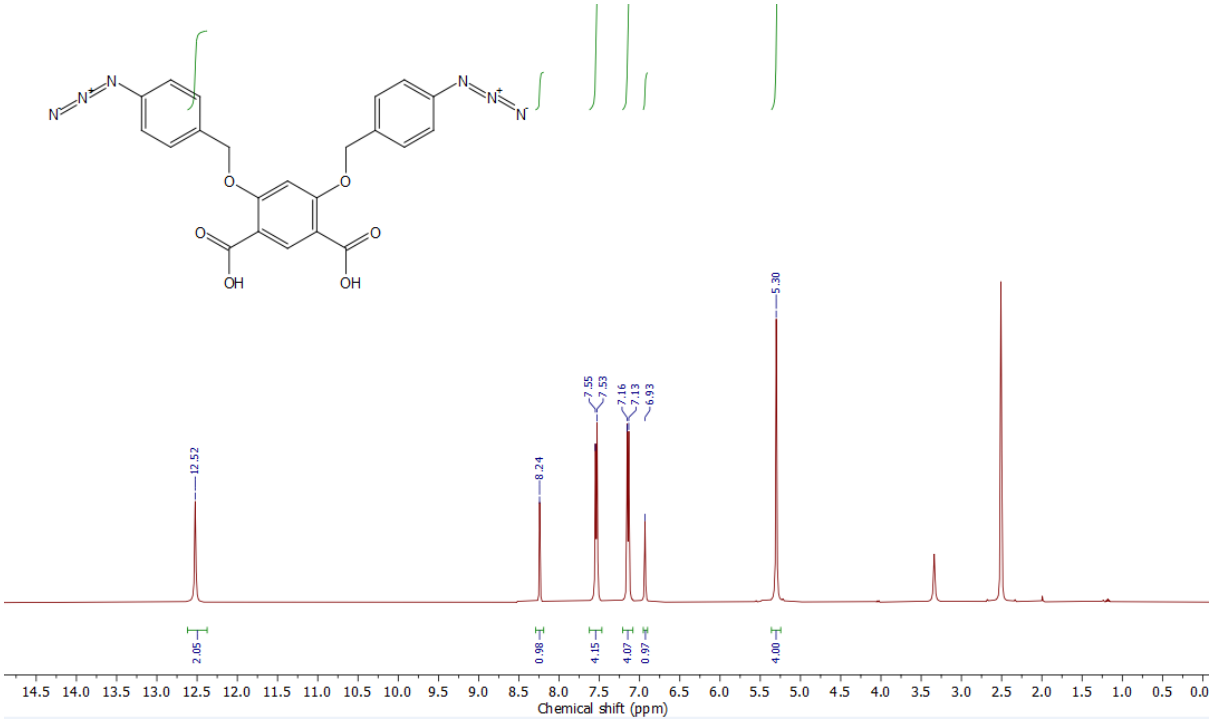

Figure S19: ^{1}H NMR Spectrum of **13** in DMSO-d_6, 298 K

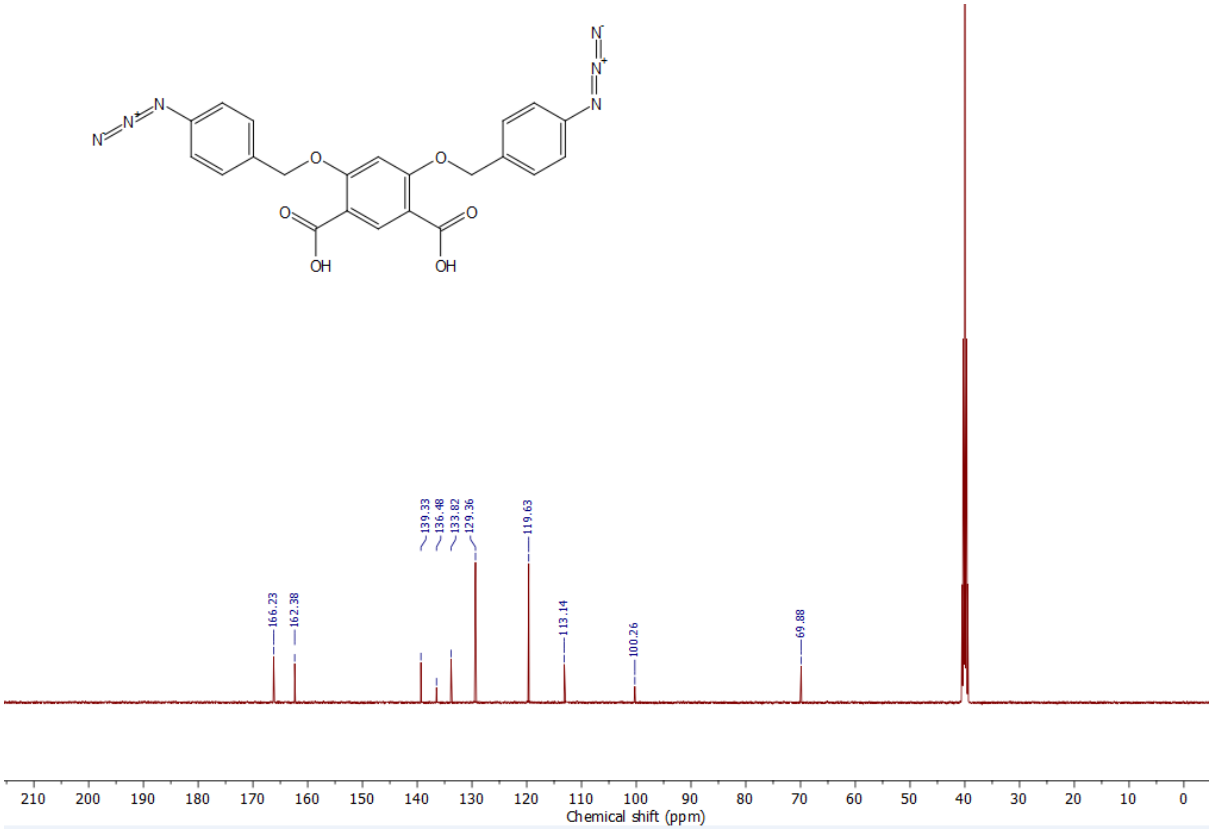

Figure S20: ^{13}C NMR Spectrum of **13** in DMSO-d_6, 298 K

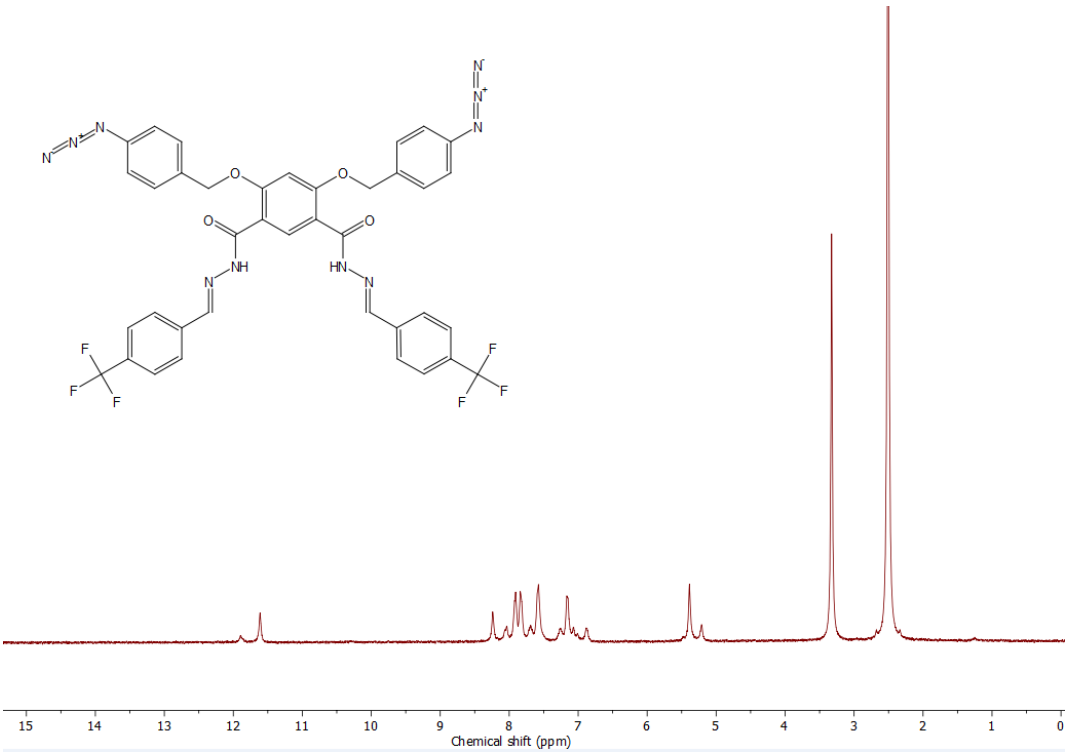

Figure S21: ^{1}H NMR Spectrum of **1b** in DMSO-d_6, 298 K

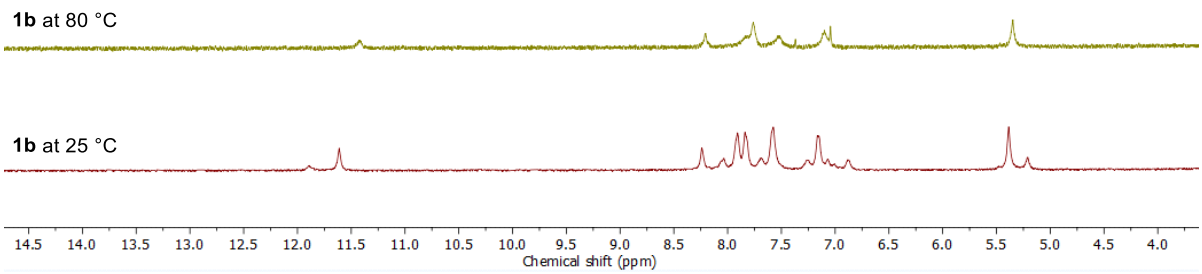

Figure S22: ^{1}H NMR Spectrum of **1b** in DMSO-d_6, at 25°C and 80°C 298 K

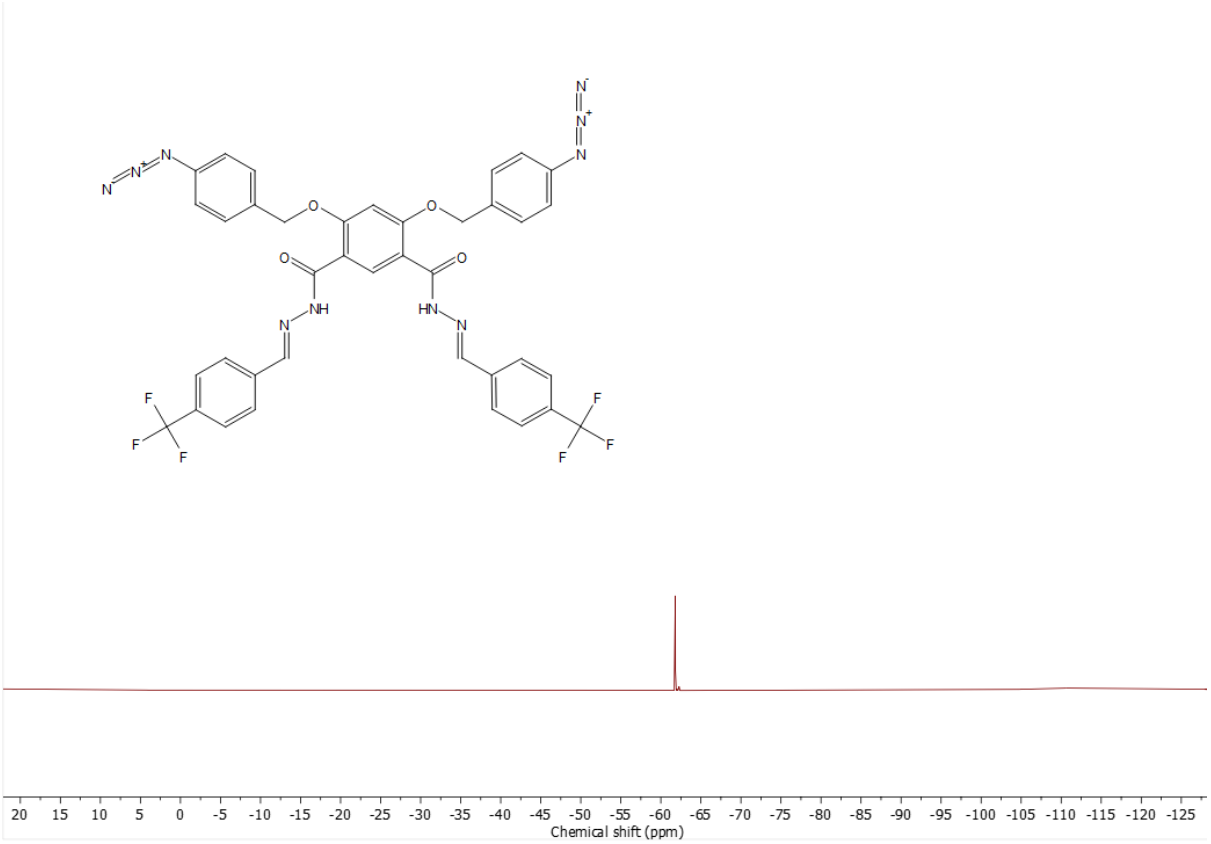

Figure S23: ^{19}F NMR Spectrum of **1b** in DMSO-d_6, 298 K

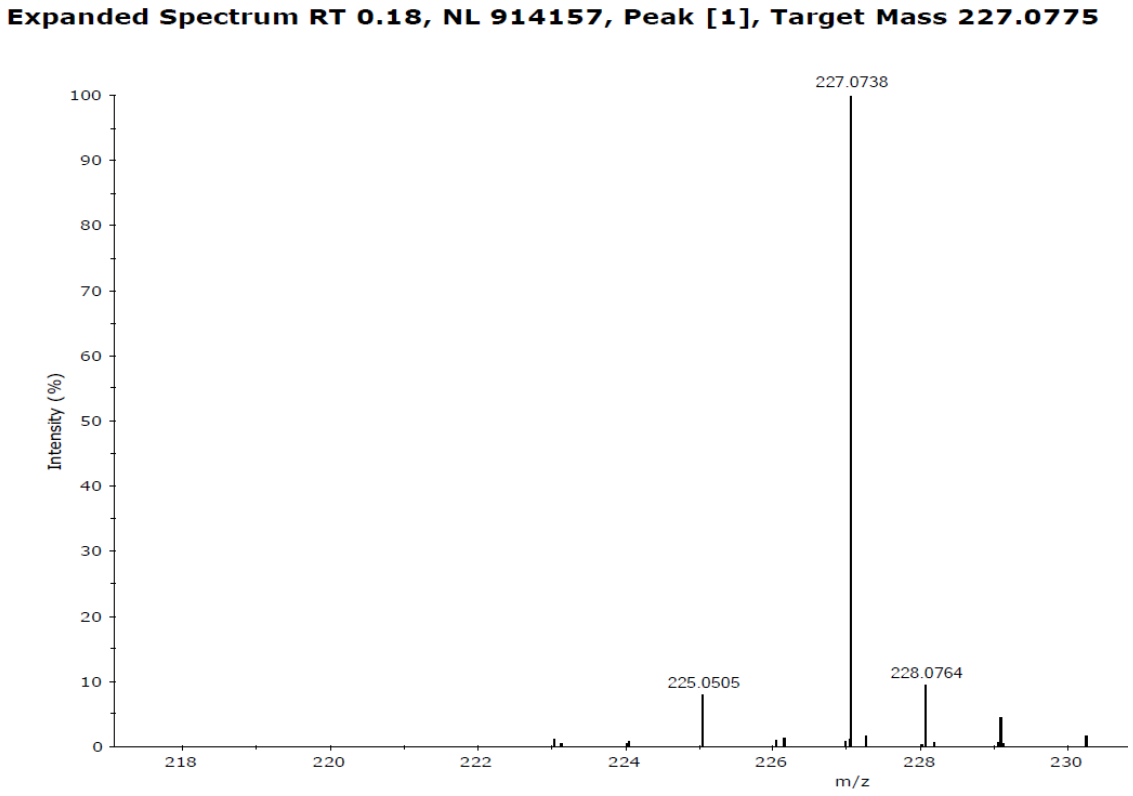

Figure S24: HRMS spectrum of **6**.

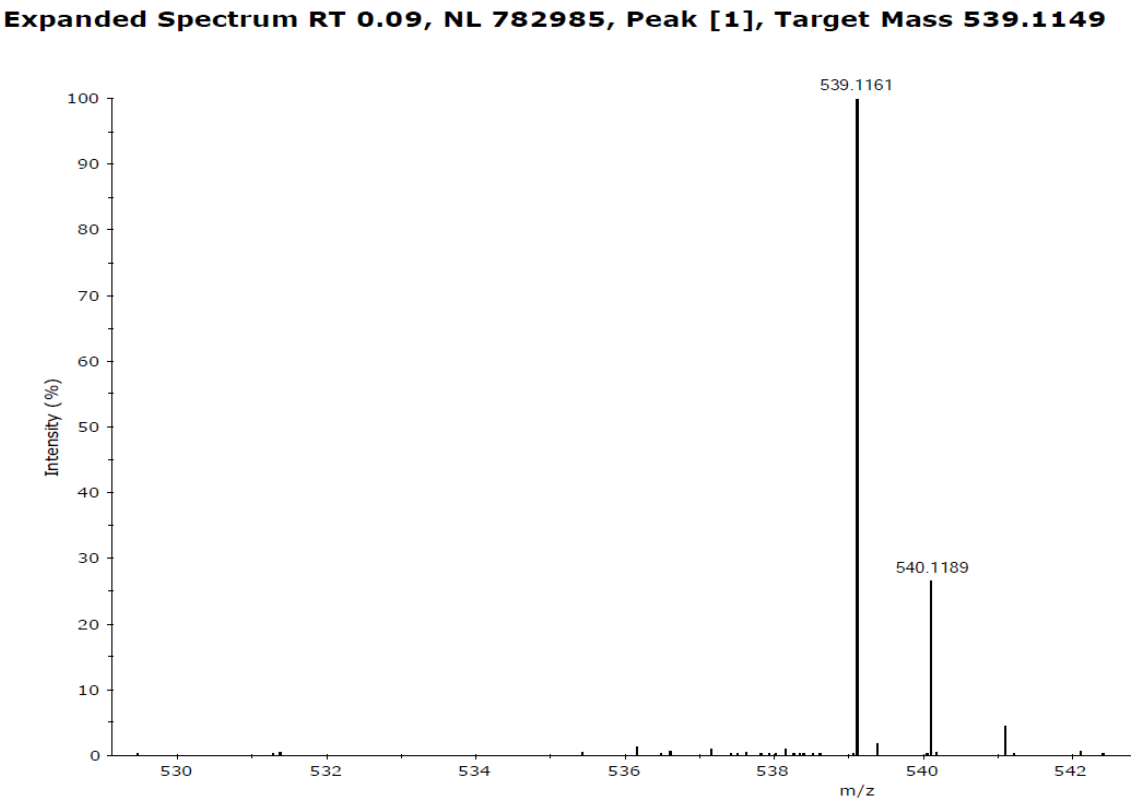

Figure S25: HRMS spectrum of **1**.

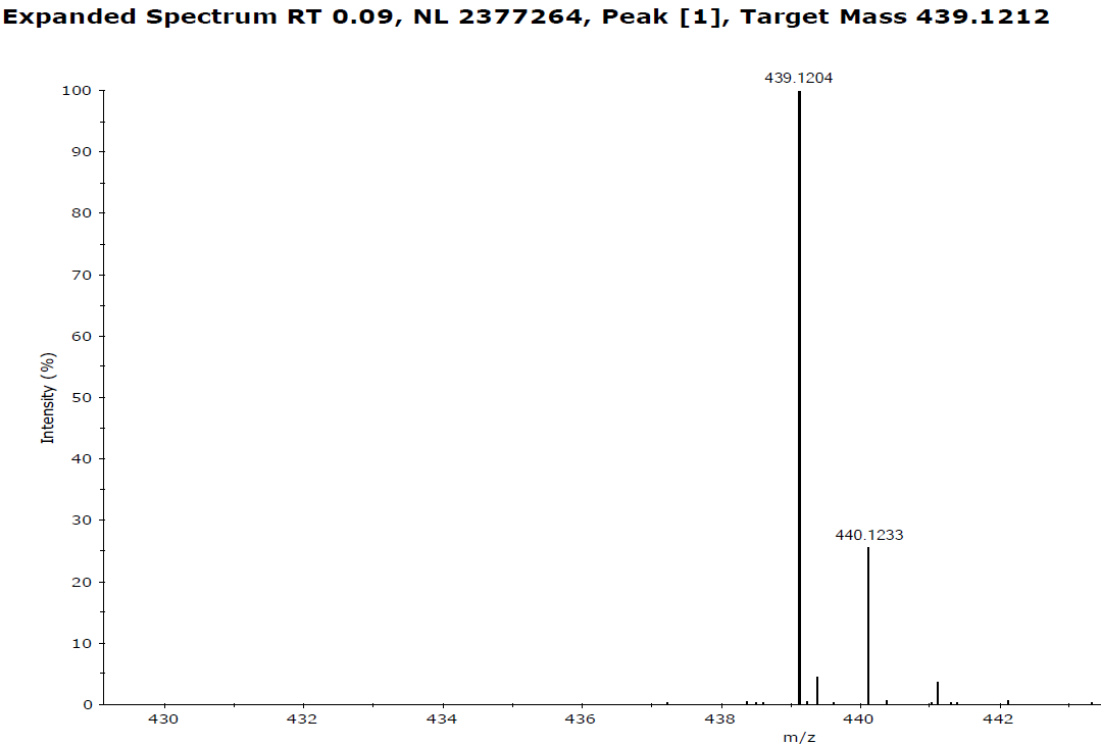

Figure S26: HRMS spectrum of **2**.

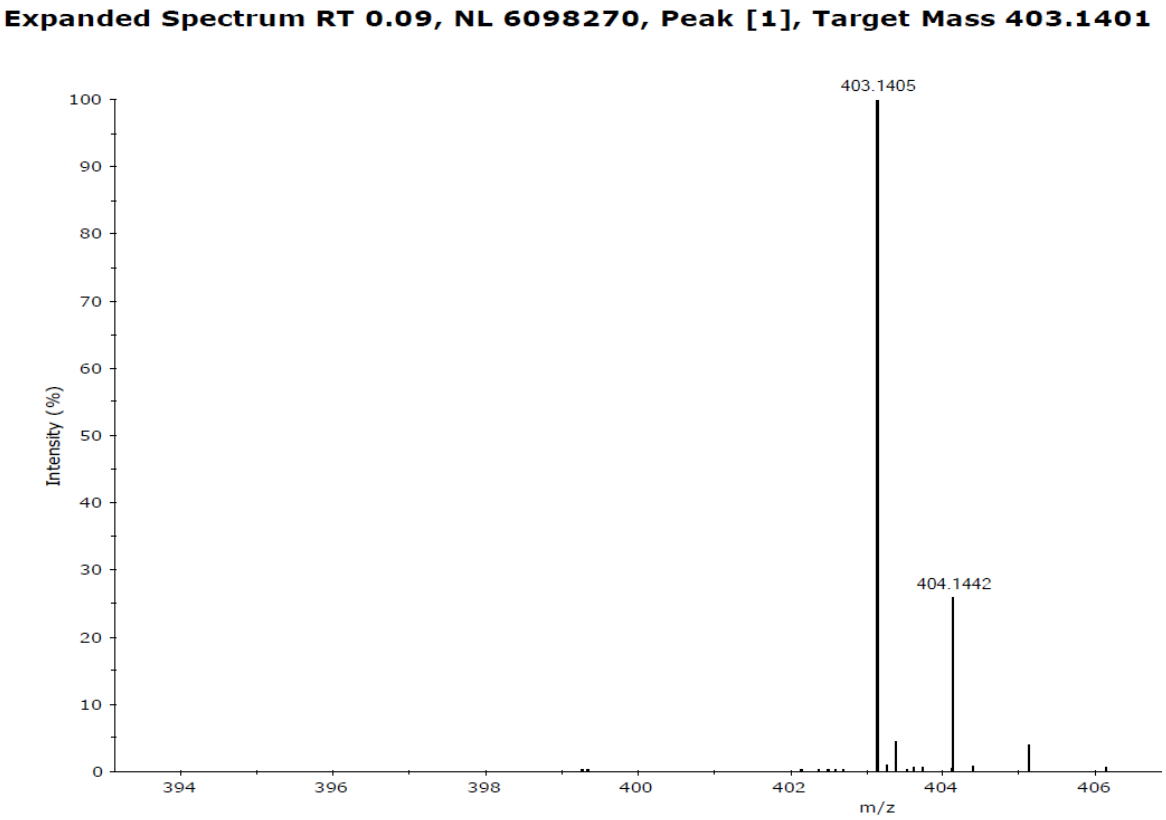

Figure S27: HRMS spectrum of **3**.

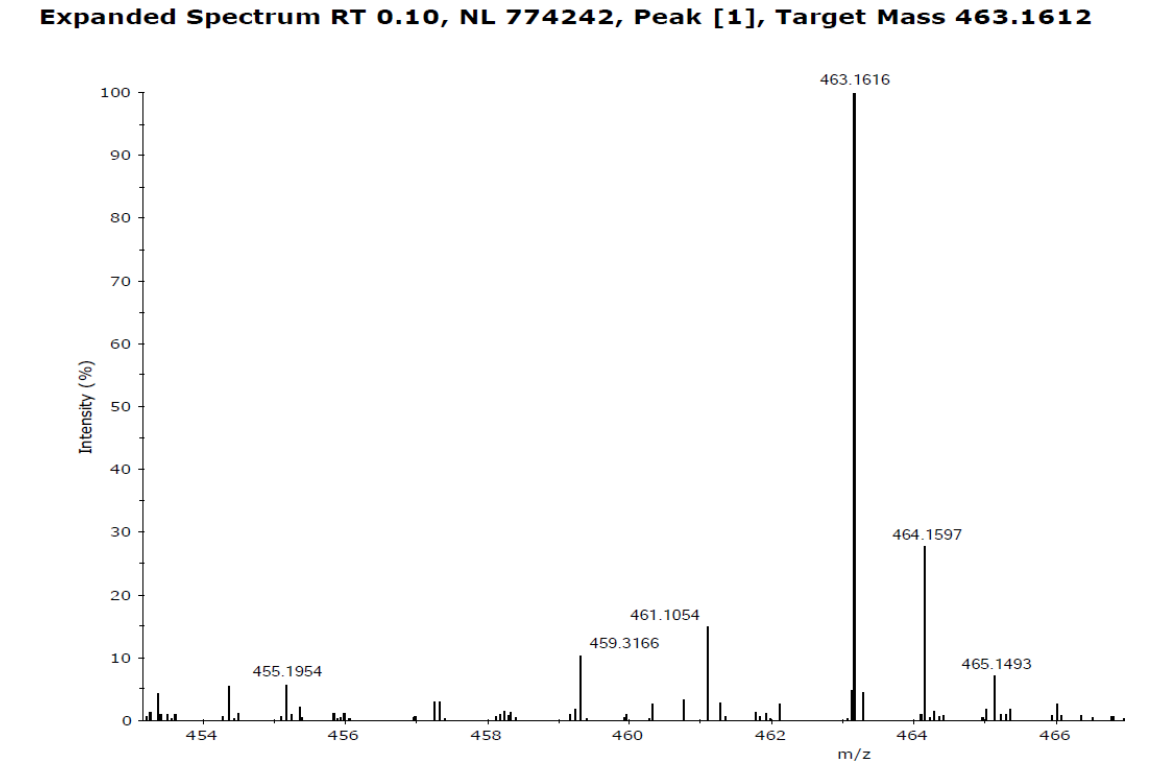

Figure S28: HRMS spectrum of **4**.

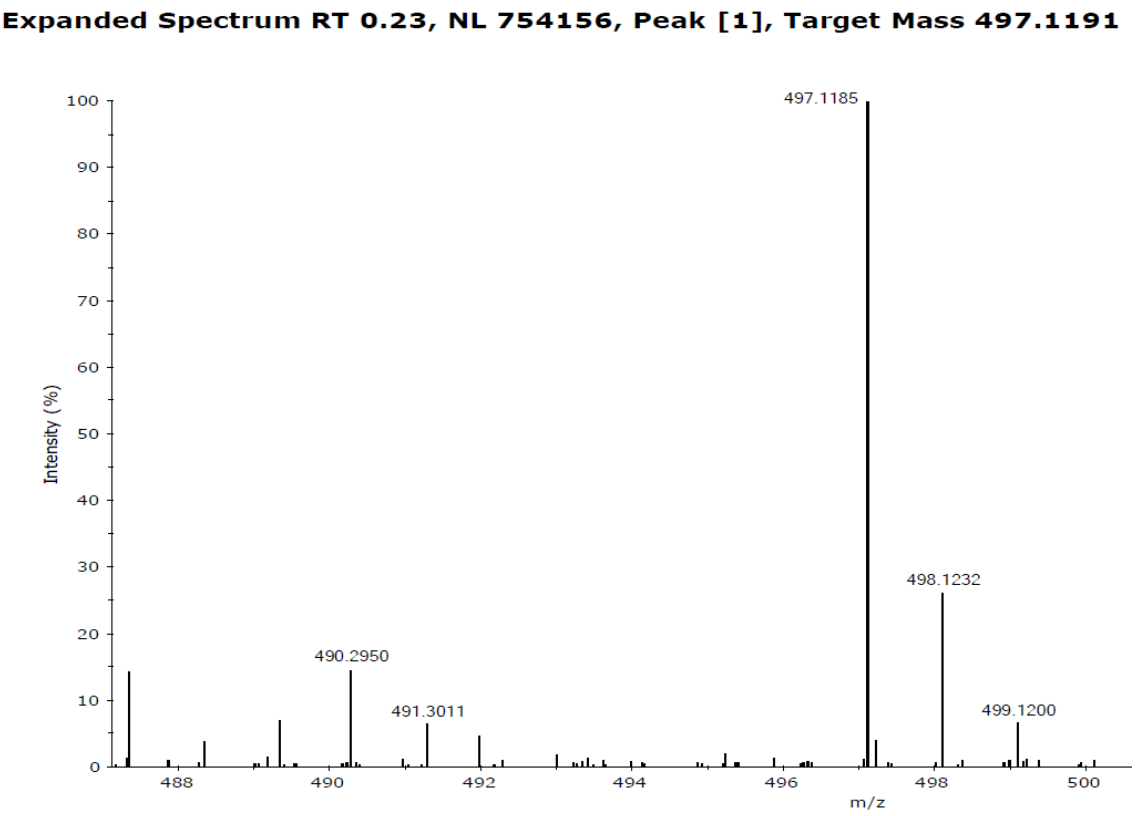

Figure S29: HRMS spectrum of **9**.

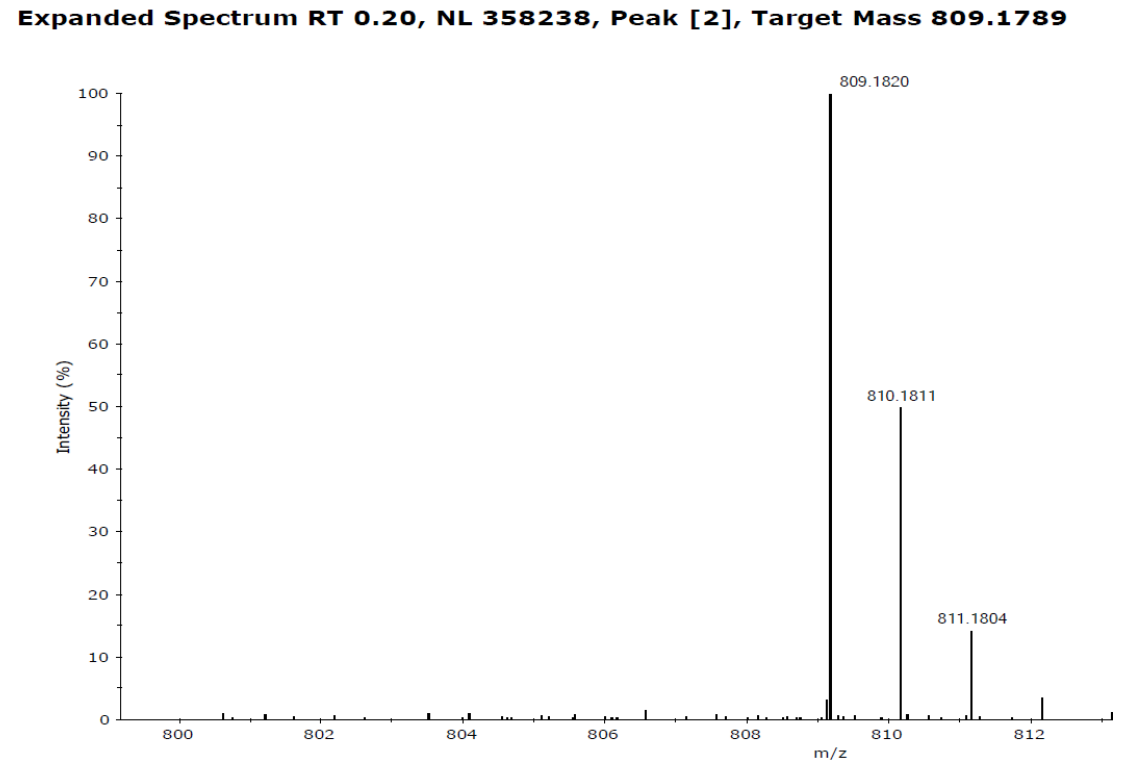

Figure S30: HRMS spectrum of **1a**.

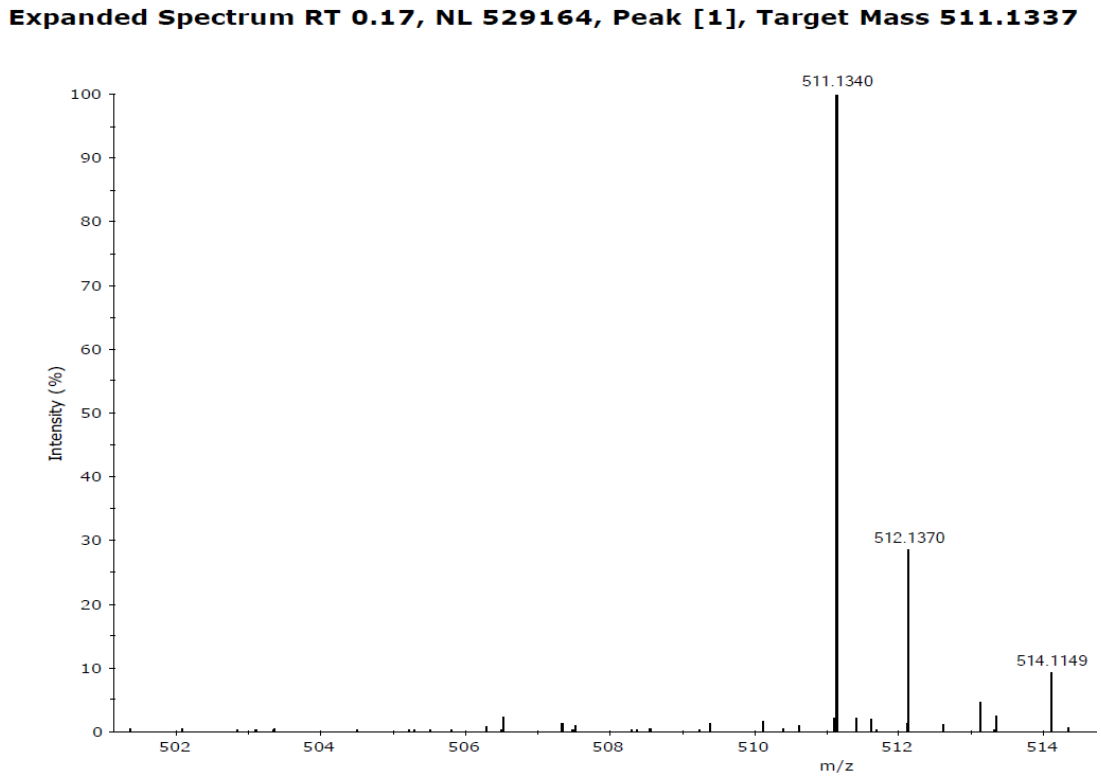

Figure S31: HRMS spectrum of **12**.

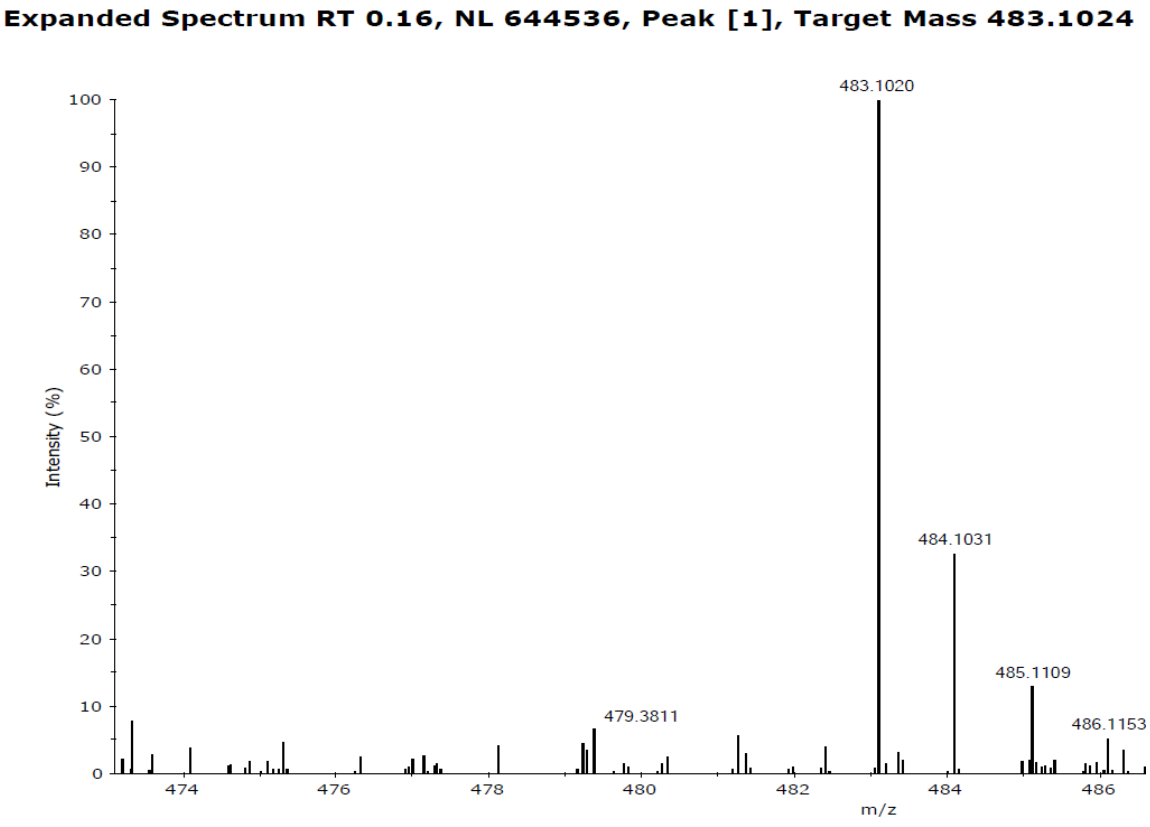

Figure S32: HRMS spectrum of **13**.

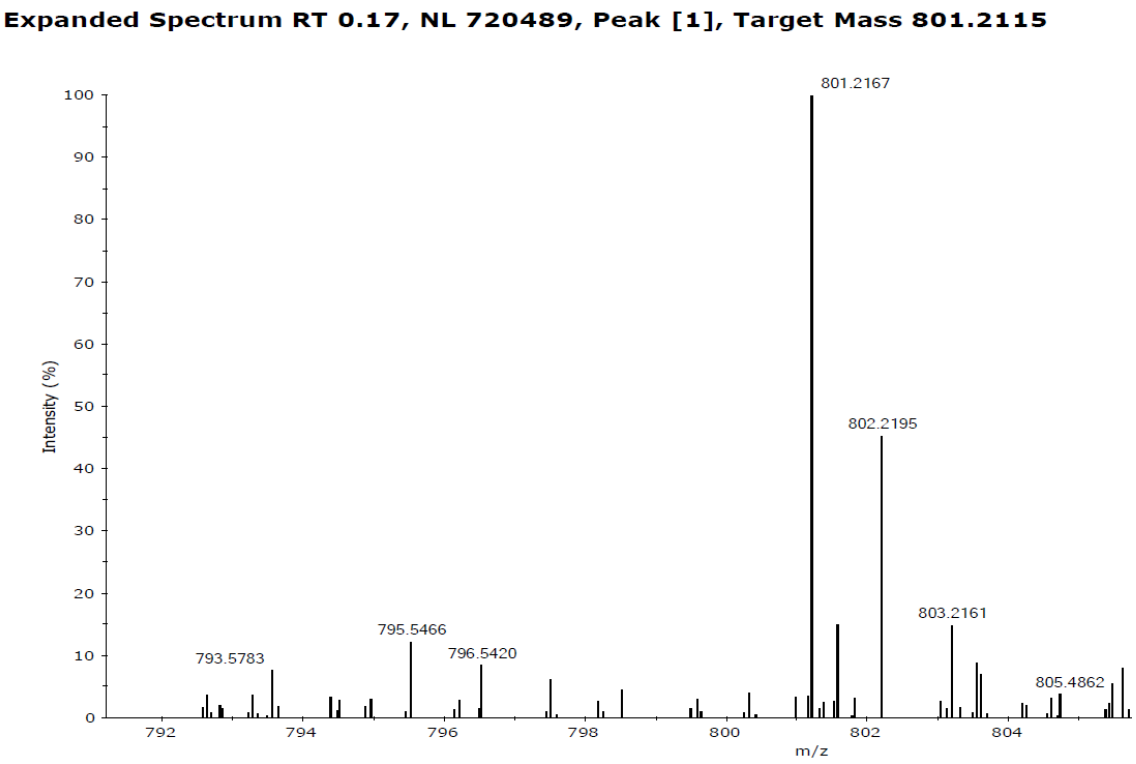

Figure S33: HRMS spectrum of **1b**.

III. Anion Binding Studies

For transporters 1-4:

^{1}H NMR titration experiments was carried out at room temperature on Bruker 500 MHz spectrometer. The residual solvent signal (DMSO-d_6, δ_H = 2.5) was considered as an internal reference to calibrate spectra. TBACl and receptor were dried under a high vacuum before use. The titrations were performed by the addition of aliquots from the solution of TBACl (0.25 M in DMSO-d_6) to the solution of receptors either of **1-5** or **1a-1b,** (2.0 mM) respectively. All NMR data were processed using MestReNova 6.0 and the collected data analysed using BindFit v0.5.[2]

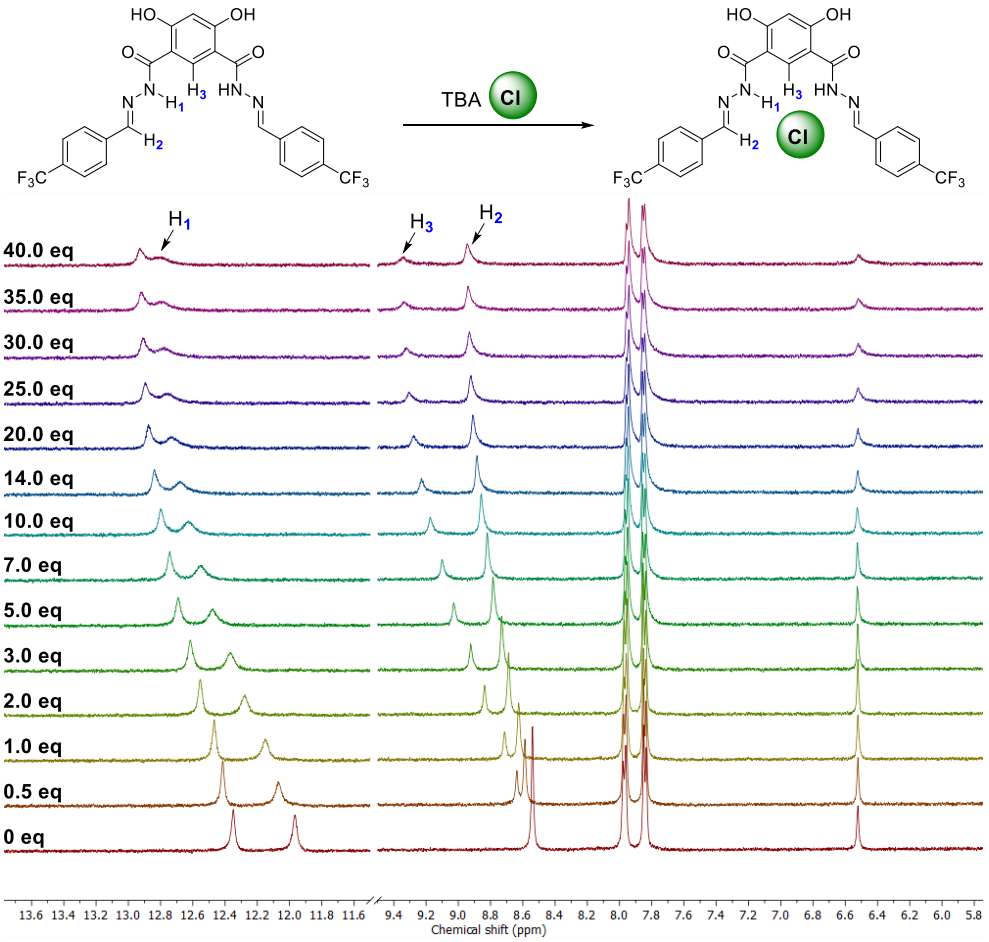

Figure S34. ^{1}H NMR titration spectra for **1** (2.0 mM) with stepwise addition of TBACl in DMSO-d_6. The equivalents of added TBACl are shown on the stacked spectra.

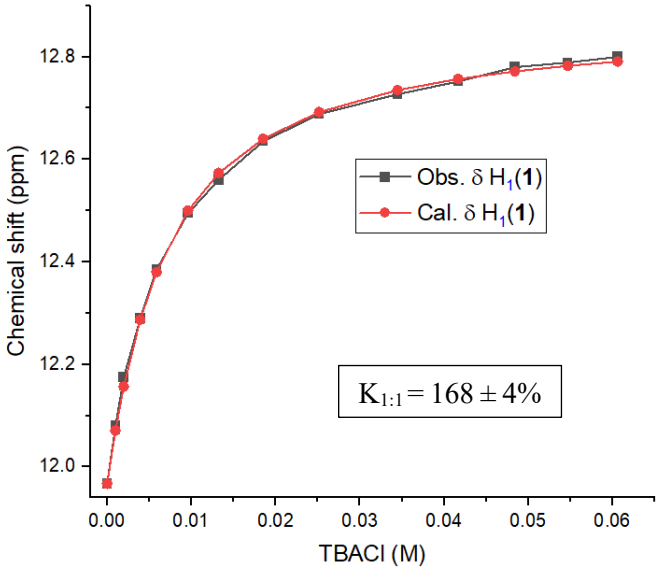

Figure S35. The plot of chemical shift (δ) of H_1 proton *vs* concentration of TBACl added, fitted to 1:1 binding model of BindFit v0.5.

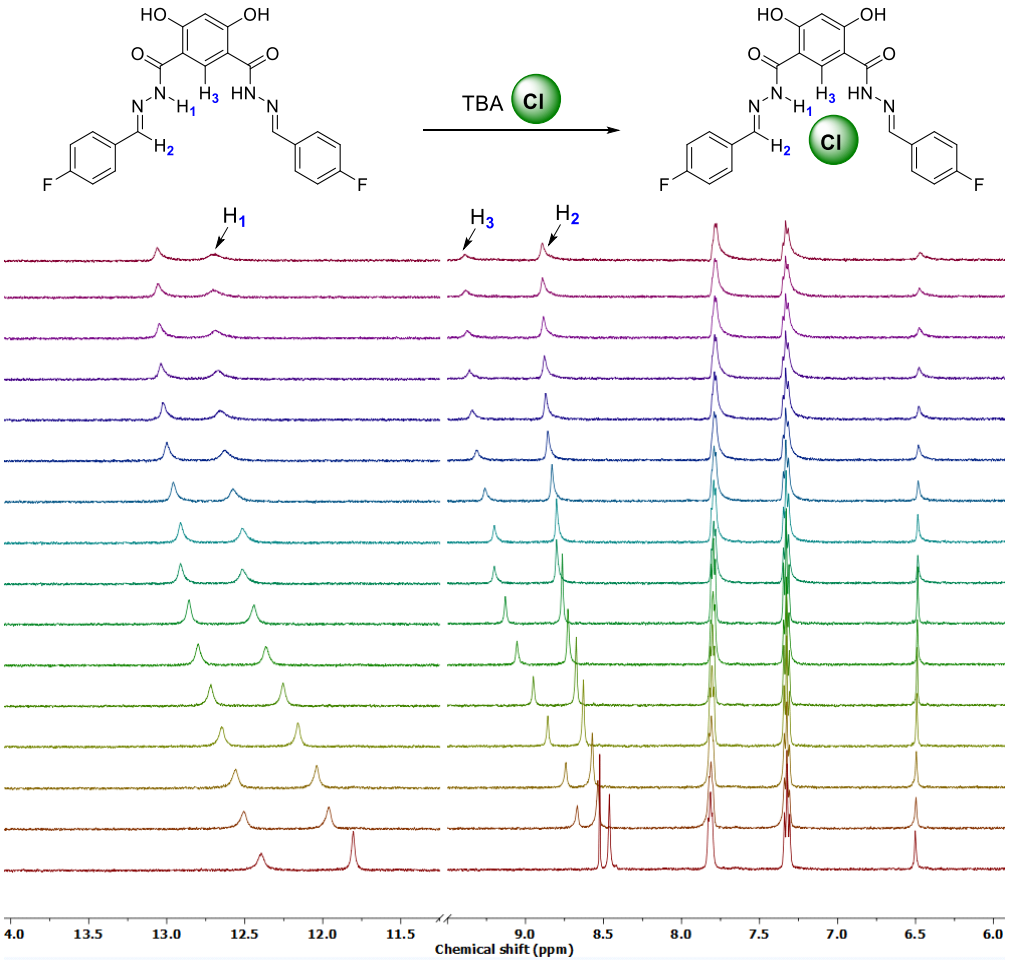

Figure S36. ^{1}H NMR titration spectra for **2** (2.0 mM) with stepwise addition of TBACl in DMSO-d_6. The equivalents of added TBACl are shown on the stacked spectra

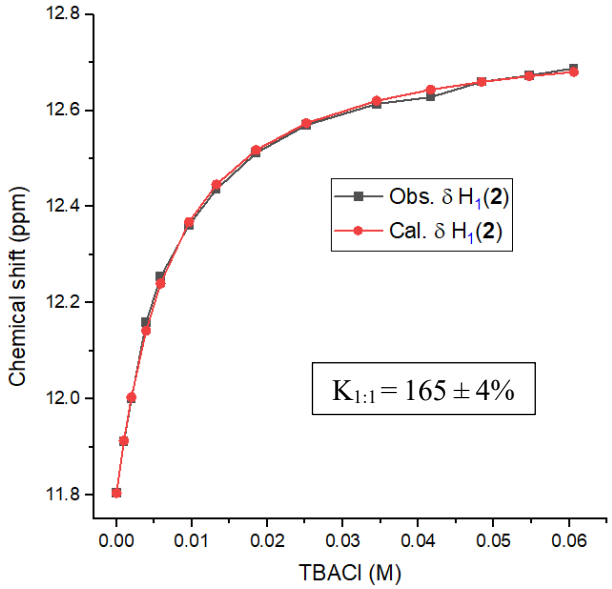

Figure S37. The plot of chemical shift (δ) of H_1 proton *vs* concentration of TBACl added, fitted to 1:1 binding model of BindFit v0.5.

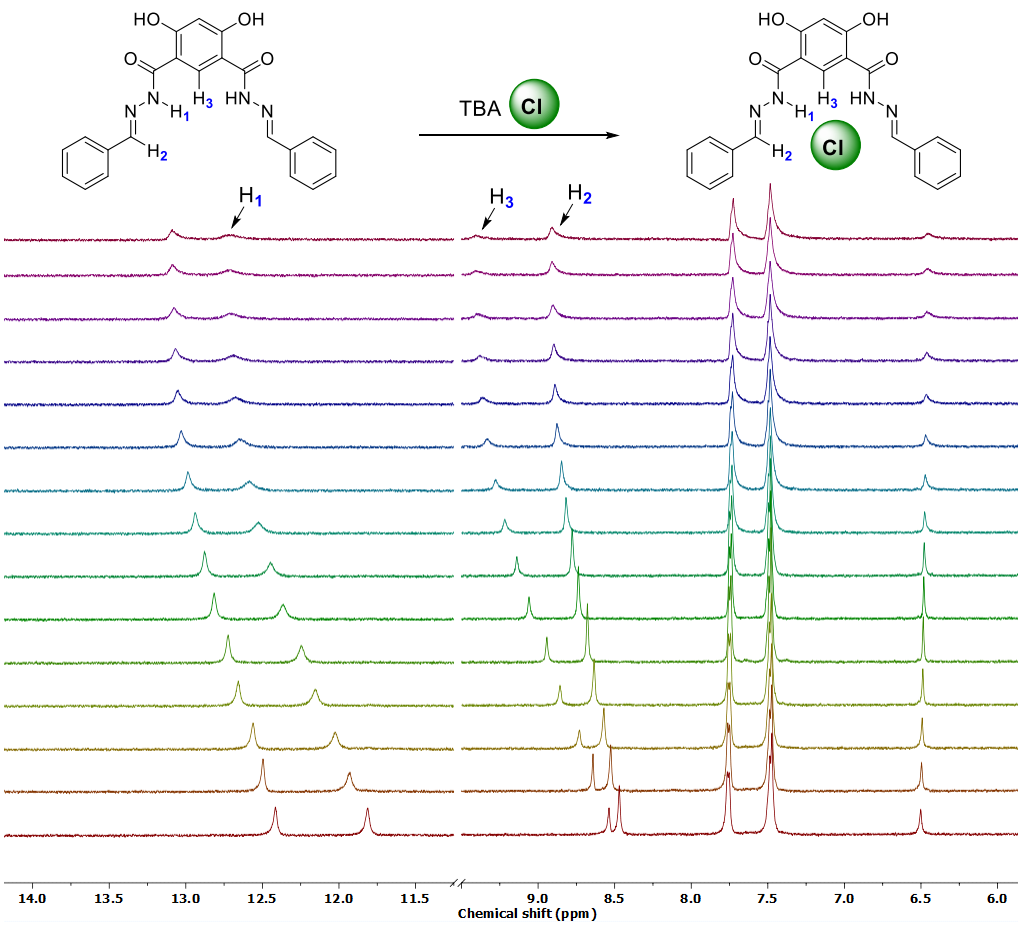

Figure S38. ^{1}H NMR titration spectra for **3** (2.0 mM) with stepwise addition of TBACl in DMSO-d_6. The equivalents of added TBACl are shown on the stacked spectra.

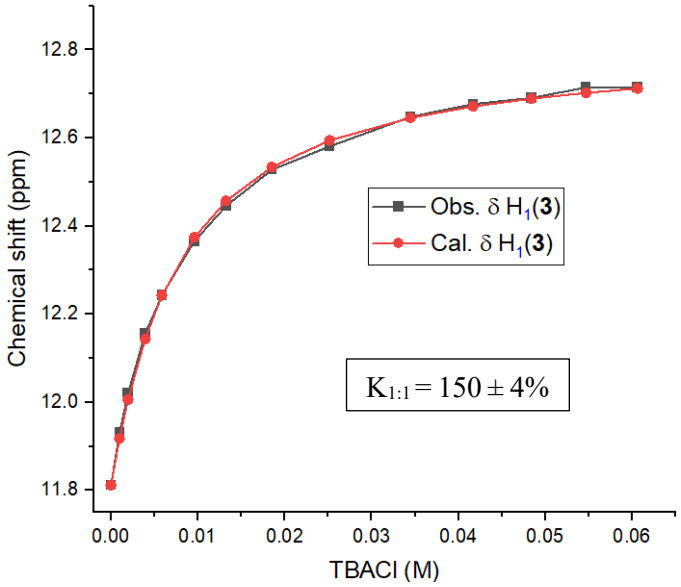

Figure S39. The plot of chemical shift (δ) of H_1 proton *vs* concentration of TBACl added, fitted to 1:1 binding model of BindFit v0.5.

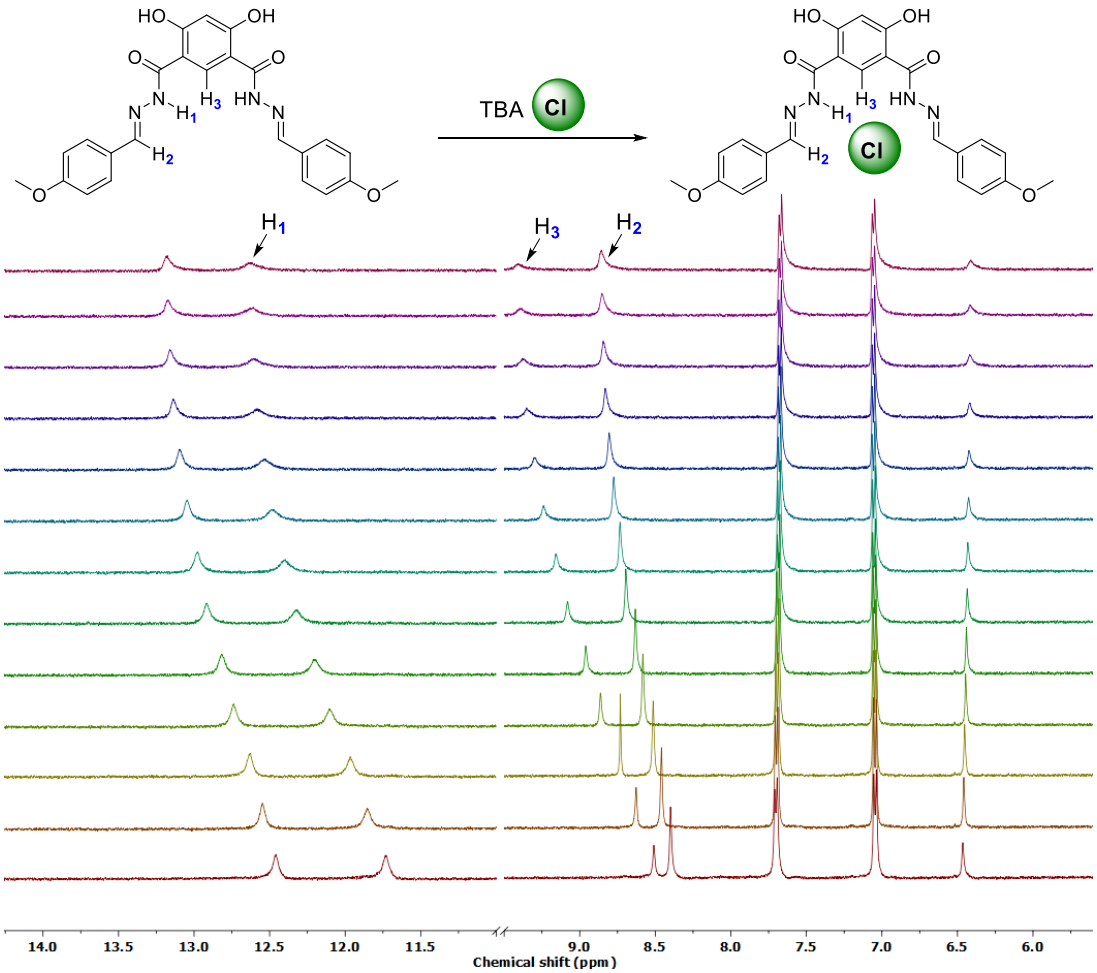

Figure S40. ^{1}H NMR titration spectra for **4** (2.0 mM) with stepwise addition of TBACl in DMSO-d_6. The equivalents of added TBACl are shown on the stacked spectra.

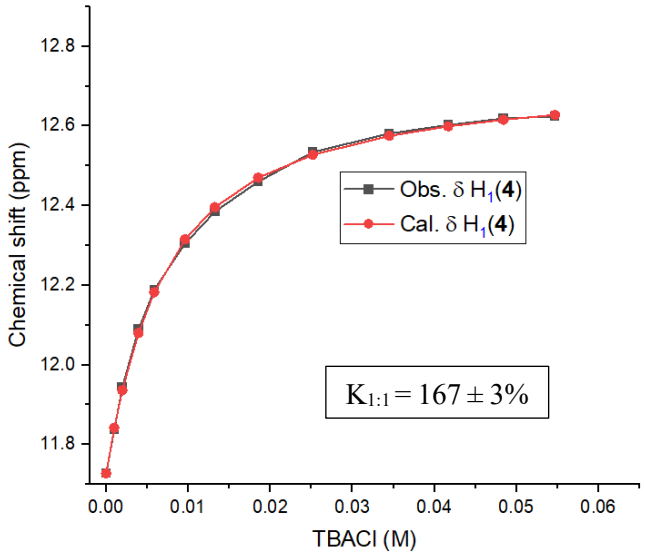

Figure S41. The plot of chemical shift (δ) of H_1 proton *vs* concentration of TBACl added, fitted to 1:1 binding model of BindFit v0.5.

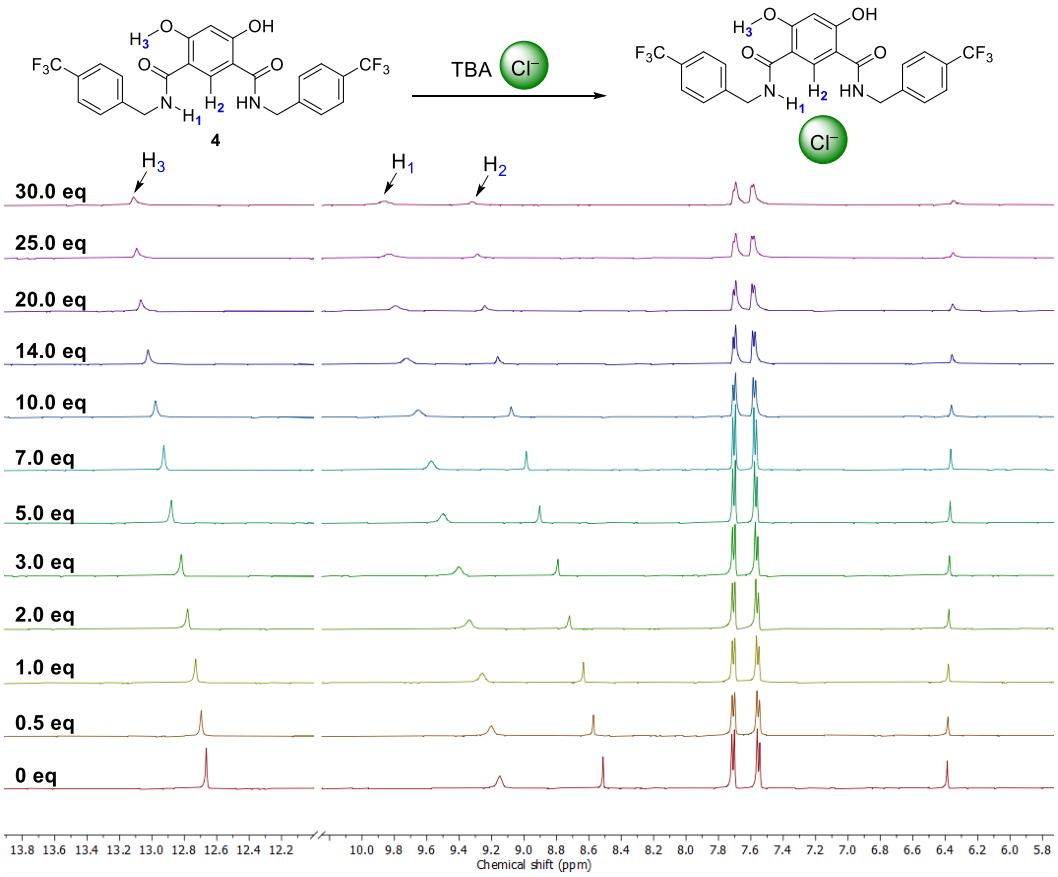

Figure S42. ^{1}H NMR titration spectra for **5** (2.0 mM) with stepwise addition of TBACl in DMSO-d_6. The equivalents of added TBACl are shown on the stacked spectra.

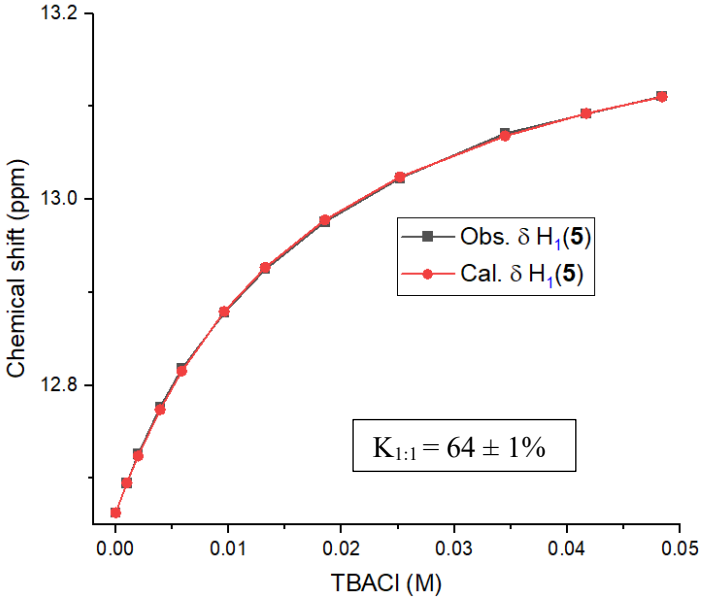

Figure S43. The plot of chemical shift (δ) of H_1 proton *vs* concentration of TBACl added, fitted to 1:1 binding model of BindFit v0.5.

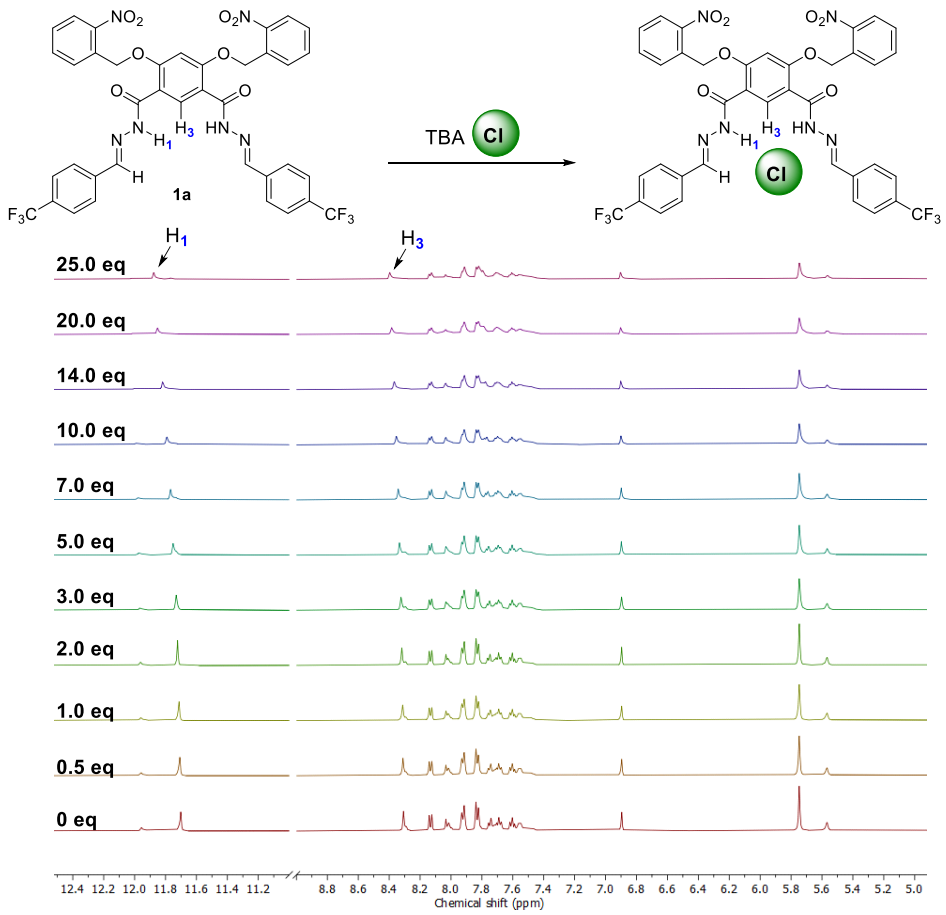

Figure S44. ^{1}H NMR titration spectra for **1a** (2.0 mM) with stepwise addition of TBACl in DMSO-d_6. The equivalents of added TBACl are shown on the stacked spectra.

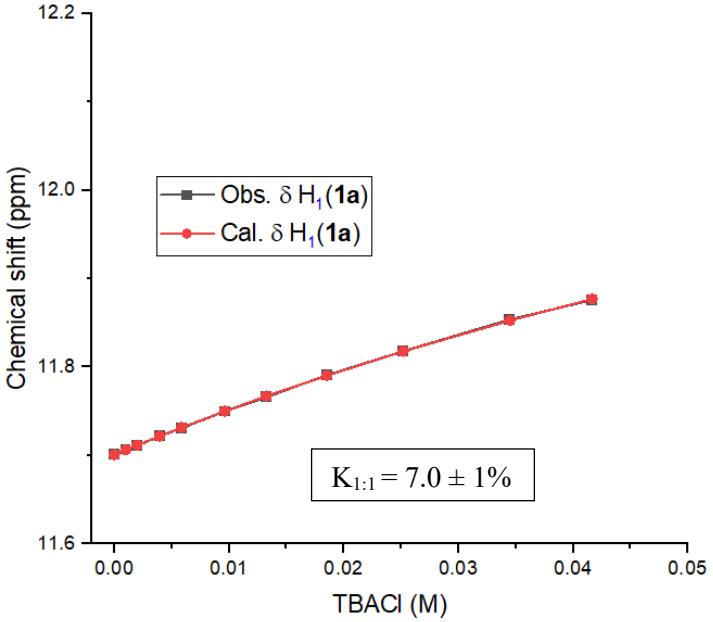

Figure S45. The plot of chemical shift (δ) of H_1 proton *vs* concentration of TBACl added, fitted to 1:1 binding model of BindFit v0.5.

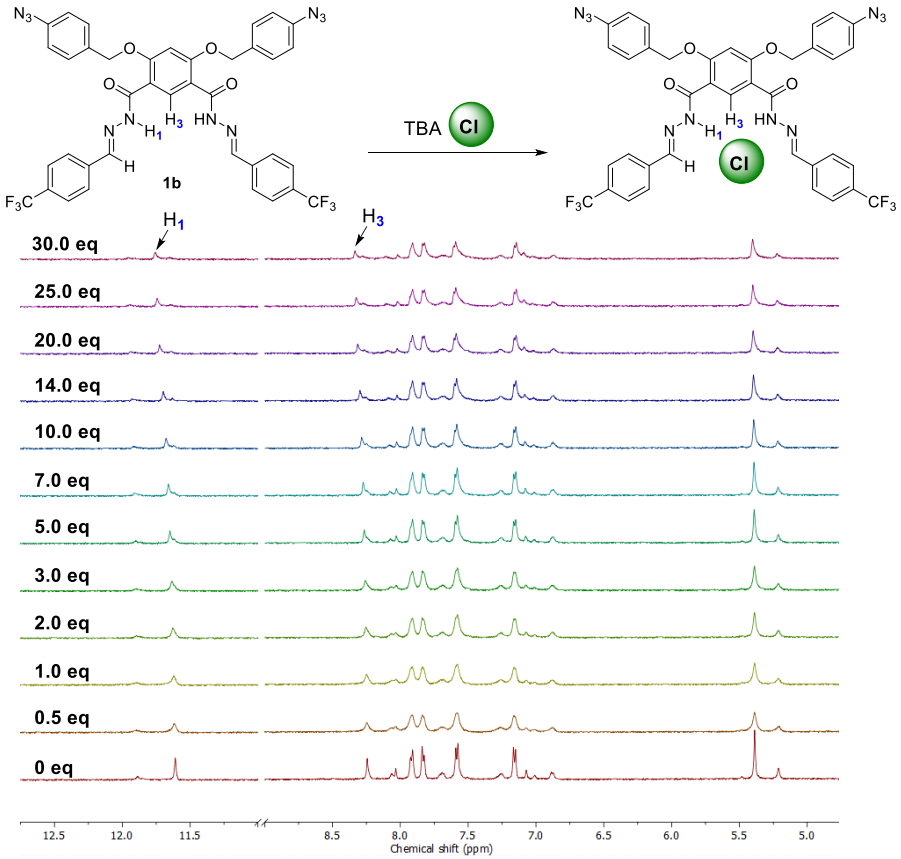

Figure S46. ^{1}H NMR titration spectra for **1b** (2.0 mM) with stepwise addition of TBACl in DMSO-d_6. The equivalents of added TBACl are shown on the stacked spectra.

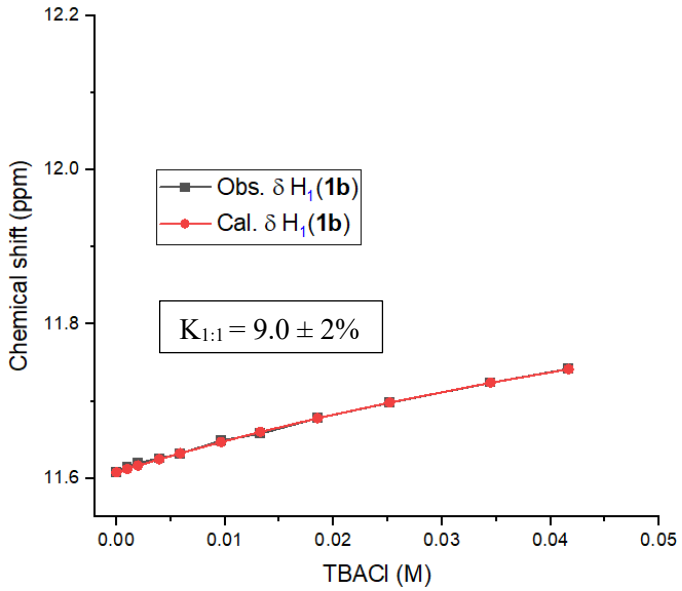

Figure S47. The plot of chemical shift (δ) of H_1 proton *vs* concentration of TBACl added, fitted to 1:1 binding model of BindFit v0.5.

IV. Chloride transport activity across POPC-LUVs⊃lucigenin vesicles

Preparation of POPC-LUVs⊃lucigenin vesicles: In 10 mL clean and dry round bottom flask, the thin transparent film of POPC was formed by drying 1.0 mL 1-palmitoyl-2-oleoyl-sn-glycero-3-phosphocholine (POPC, 25 mg/mL in $CHCl_3$) whilst providing continuous rotation and purging nitrogen. The transparent thin film was kept under a high vacuum for 4 hours to remove all traces of $CHCl_3$, before it was hydrated with 1.0 mL aqueous $NaNO_3$ (200 mM, 1.0 mM Lucigenin) with pH of 6.5 using 10 mM phosphate buffer with occasional vortexing at 10 min intervals for 1 h. The resulting suspension was subjected to freeze and thaw cycles (≥ 10 liquid nitrogen, 55 °C water bath) and 21 times extrusion through 200 nm pore size polycarbonate membrane. Size exclusion chromatography (using Sephadex G-50) was performed to remove extravesicular dye using 200 mM $NaNO_3$ solution as eluent. The collected vesicles suspension was diluted to 4 mL. Final conditions: ~ 5 mM POPC; inside: 200 mM $NaNO_3$, 1 mM lucigenin, pH = 6.5; outside: 200 mM $NaNO_3$, pH = 6.5.

Ion transport activity by Lucigenin assay

In clean and dry fluorescence cuvette, 200 mM $NaNO_3$ (2890 µL), POPC-LUVs⊃lucigenin (40 µL, 109.6 µM) and ion transporters **1-5** (20 µL from DMF solution) were added. This suspension was placed in a slowly stirring condition in a fluorescence instrument equipped with a magnetic stirrer (at t = 0 s). The fluorescence intensity of lucigenin was monitored at λ_{em} = 535 nm (λ_{ex} = 455 nm) over time. The chloride gradient was created by the addition of 2.0 M NaCl (50 µL) at t = 50 s between intra- and extravesicular solutions. Finally, vesicles were lysed by adding 10% Triton X-100 (40 µL) at t = 200 s for the complete disipation of the chloride gradient.

The time-dependent data were normalized to percent change in fluorescence intensity using Equation S1:

$$I_F = [(I_t - I_0) / (I_\infty - I_0)] \times (-1) \qquad \text{Equation S1}$$

where, I_0 is the initial intensity, I_t is the intensity at time t, and I_∞ is the final intensity after addition of Triton X-100.

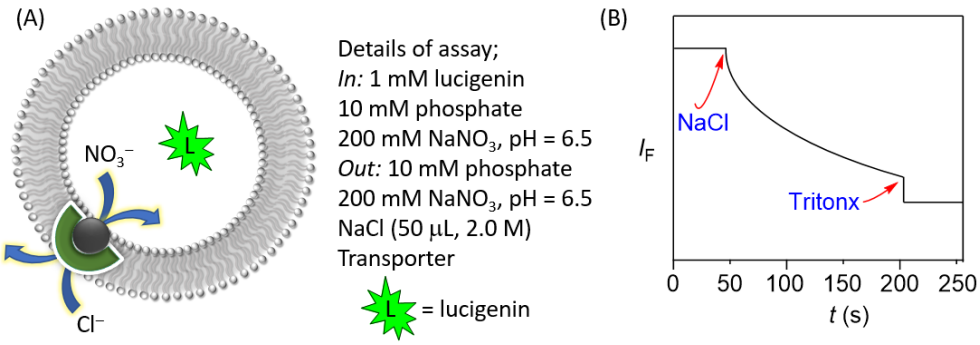

Figure S48. Representation of fluorescence-based ion transport activity assay using POPC-LUVs⊃Lucigenin (A), and illustration of ion transport kinetics showing normalization window (B).

Dose-response activity: The activity of each transporter at different concentrations was studied. The concentration profile data were evaluated from the fluorescence intensity at t = 240 s to afford the effective concentration, EC_{50} (i.e., the concentration of transporter needed to achieve 50% chloride efflux) using the Hill equation (Equation S2):

$$Y = Y_\infty + (Y_0 - Y_\infty) / [1 + (c/EC_{50})^n] \qquad \text{Equation S2}$$

where, Y_0 = fluorescence intensity just before the transporter addition (at t = 0 s), Y_∞ =fluorescence intensity with excess transporter concentration, c = concentration of transporter compound, and n = Hill coefficient (i.e., indicative for the number of monomers needed to form an active supramolecule).

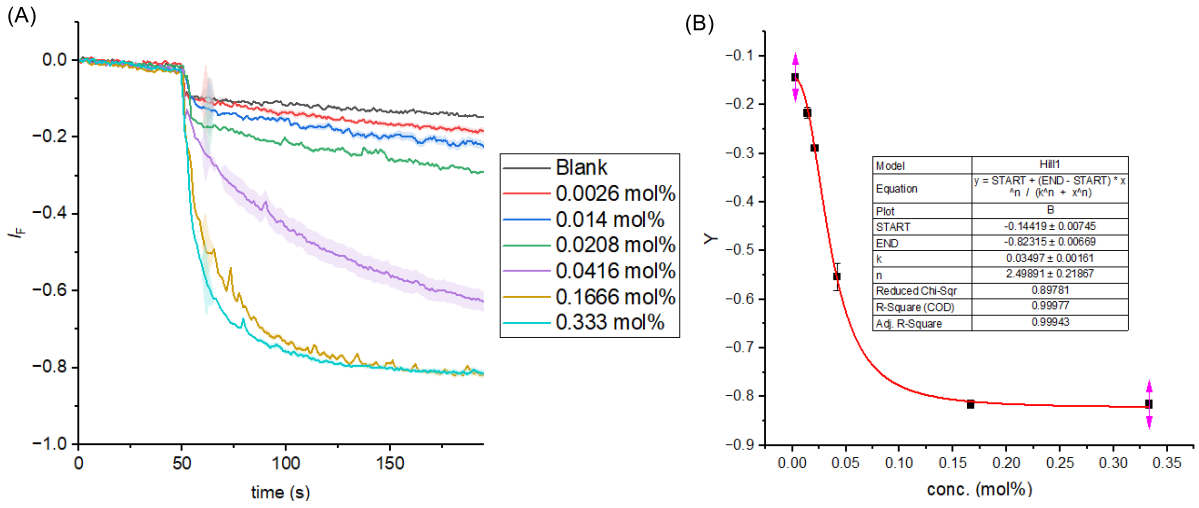

Figure S49: Concentration dependent activity of **1** across POPC-LUVs⊃lucigenin (A). Dose response plot of **1** at 180 s (B).

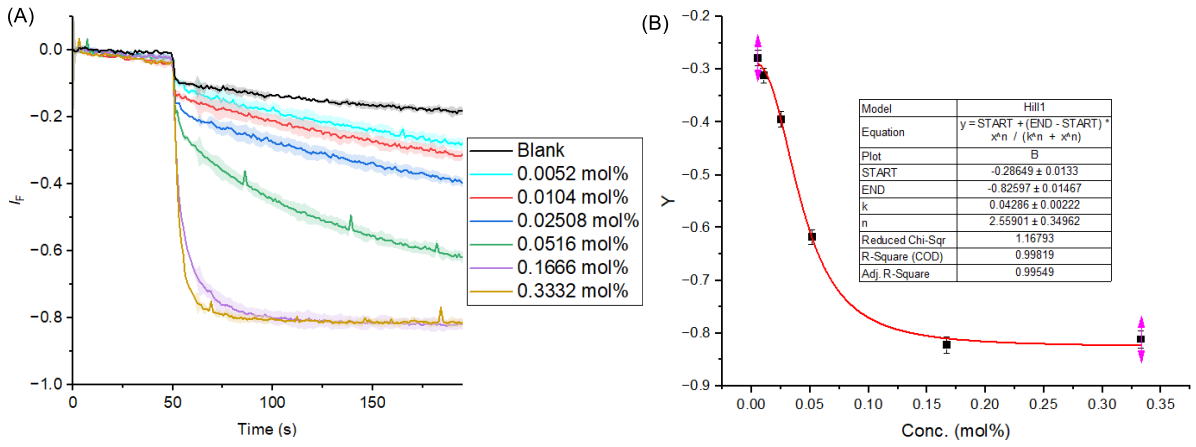

Figure S50: Concentration dependent activity of **2** across POPC-LUVs⊃lucigenin (A). Dose response plot of **2** at 180 s (B).

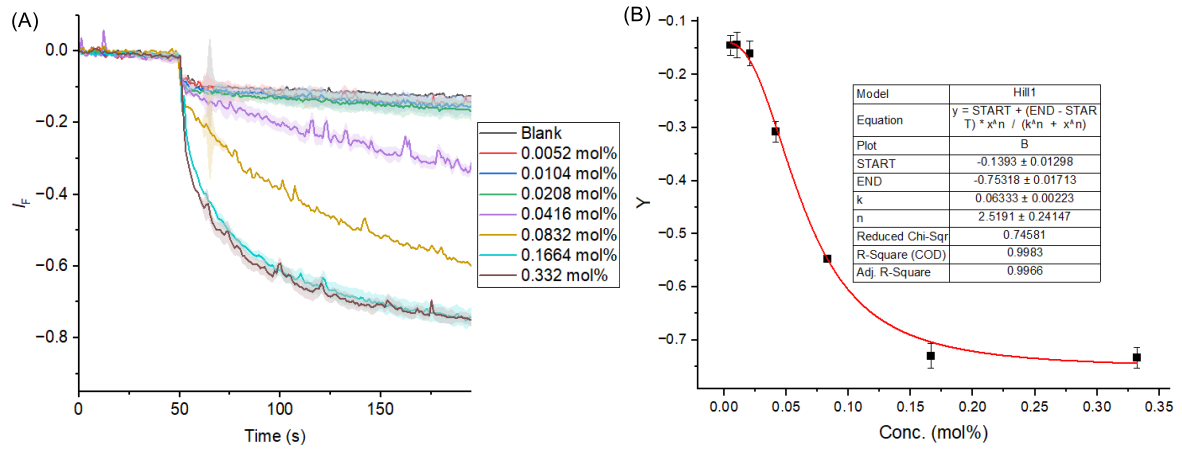

Figure S51: Concentration dependent activity of **3** across POPC-LUVs⊃lucigenin (A). Dose response plot of **3** at 180 s (B).

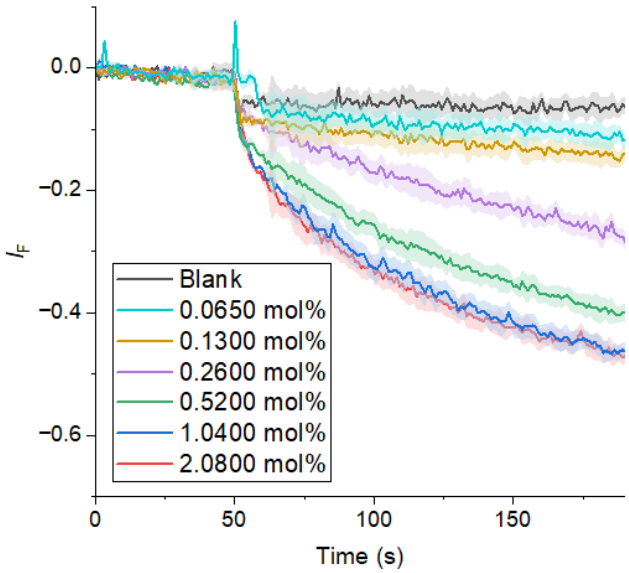

Figure S52: Concentration dependent activity of **4** across POPC-LUVs⊃lucigenin.

Cation selectivity assay across POPC-LUVs⊃lucigenin vesicles

The vesicles were prepared by following the same protocol as stated above. In clean and dry fluorescence cuvette, 200 mM MNO_3 (2890 µL) buffer (M^+ = Li^+, Na^+, K^+, Rb^+, and Cs^+), POPC-LUVs⊃lucigenin (40 µL, 109.6 µM) and **1** (0.06 mol%) were taken. The suspension was kept in slowly stirring condition in a fluorescence instrument equipped with a magnetic stirrer at t = 0 s. The quenching of fluorescence intensity of lucigenin was monitored as a course of time at λ_{em} = 535 nm (λ_{ex} = 455 nm) by addition of 2 M chloride MCl salts (50 µL) (M^+ = Li^+, Na^+, K^+, Rb^+, and Cs^+) at t = 50 s.

Finally, vesicles were lysed by the addition of 10% Triton X-100 (40 µL) at t = 250 s to destruct the applied chloride gradient completely. The time-dependent data were normalized to percent change in fluorescence intensity using Equation S1 respectively.

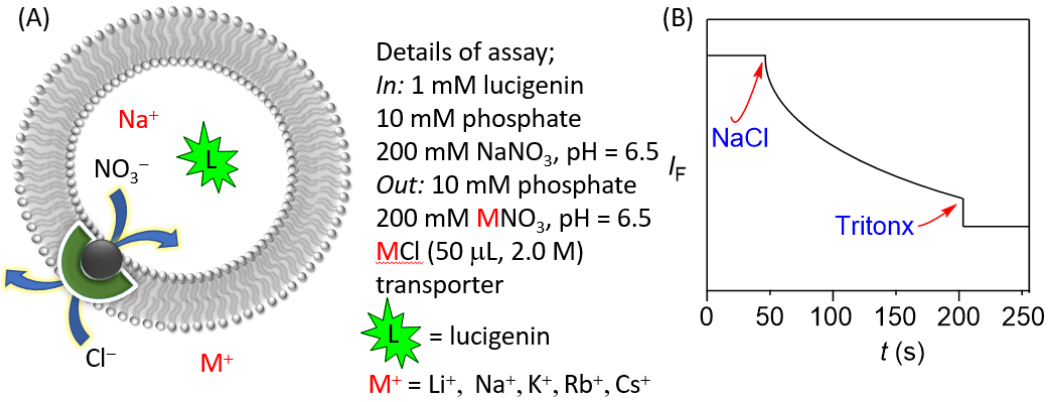

Figure S53. Schematic representation of fluorescence-based cation selectivity assay (A), and illustration of ion transport kinetics showing normalization window (B).

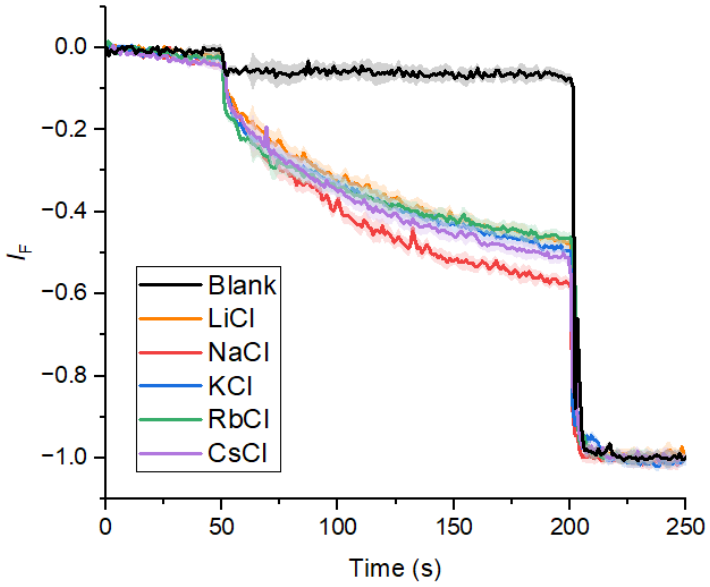

Figure S54: Ion transport activity of **1** (0.05 mmol%) by using different MNO_3 external buffer (200 mM, 2890 µL) (M^+ = Li^+, Na^+, K^+, Rb^+, and Cs^+).

Proof of antiport mechanism by lucigenin assay in the presence of external SO_4^{2-} and NO_3^- anions

Preparation of POPC-LUVs⊃lucigenin vesicles: In a 10 mL clean and dry round bottom flask, the thin transparent film of 1-palmitoyl-2-oleoyl-sn-glycero-3-phosphocholine (POPC) was formed by drying 1.0 mL POPC (25 mg/mL in $CHCl_3$) while providing continuous rotation and purging nitrogen. The transparent thin film was kept under a high vacuum for 4 hours to remove all traces of $CHCl_3$. Then the transparent thin film was hydrated with 1.0 mL aqueous NaCl (200 mM, 1.0 mM Lucigenin) buffered at pH of 6.5 with occasional vortexing at 10 min intervals for 1 h. The resulting suspension was subjected to freeze and thaw cycles (≥ 10 liquid nitrogen, 55 ° C water bath) and 21 times extrusion through 200 nm pore size polycarbonate membrane. The size exclusion chromatography (using Sephadex G-50) was performed to remove extravesicular dye using 200 mM NaCl solution as eluent. The collected vesicles

suspension was diluted to 4 mL. Final conditions: ~ 5 mM POPC; inside: 200 mM NaCl, 1 mM lucigenin, pH 6.5; outside: either 200 mM $NaNO_3$ or 200 mM Na_2SO_4.

Ion transport assay

In a clean and dry fluorescence cuvette, either 200 mM of $NaNO_3$ or 200 mM of Na_2SO_4 (2890 µL) and POPC-LUVs⊃lucigenin (40 µL, 109.6 µM) was added. This suspension was placed in a slowly stirring condition in a fluorescence instrument equipped with a magnetic stirrer (at $t = 0$ s). The fluorescence intensity of lucigenin was monitored at $\lambda_{em} = 535$ nm ($\lambda_{ex} = 455$ nm) as a course of time. The transporter molecule **4** (1.0 mol%) was added at $t = 50$ s. Finally, vesicles were lysed by adding 10% Triton X-100 (40 µL) at $t = 250$ s for the complete disipation of the chloride gradient. NO_3^- transport occurred with the concomitant efflux of Cl^- ions, and on the other hand, SO_4^{2-} being more hydrophilic is not transported easily, suggesting the operation of a Cl^-/NO_3^-antiport mechanism.

The time-dependent data were normalized to percent change in fluorescence intensity using Equation S3.

$$I_F = [(I_t - I_0) / (I_\infty - I_0)] \times (-1) \qquad \text{Equation S3}$$

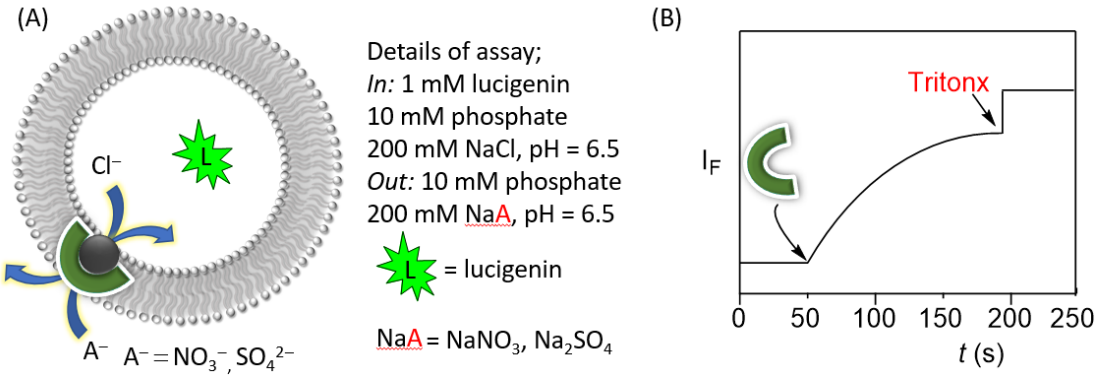

Figure S55. Representation of fluorescence-based antiport assay using POPC-LUVs⊃lucigenin (A) Representation of ion transport kinetics showing normalization window (B)

Proof of carrier mode of ion transport using DPPC vesicles

Preparation of DPPC-LUVs⊃lucigenin vesicles: In a 10 mL clean and dry round bottom flask, the thin transparent film of dipalmitoylphosphatidylcholine (DPPC) was formed by drying 0.5 mL dipalmitoylphosphatidylcholine (DPPC, 25 mg/mL in $CHCl_3$) while providing continuous rotation and purging nitrogen. The transparent thin film was kept under a high vacuum for 5 hours to remove all traces of $CHCl_3$. Then the transparent thin film was hydrated with 1.0 mL aqueous $NaNO_3$ (200 mM, 1.0 mM Lucigenin) buffered at pH of 6.5 using 10 mM of phosphate buffer with occasional vortexing at 10 min intervals for 1 h. The resulting suspension was subjected to freeze and thaw cycles (≥ 10 liquid nitrogen, 55° C water bath) and 21 times extrusion through 200 nm pore size polycarbonate membrane. The size exclusion chromatography (using Sephadex G-50) was performed to remove extravesicular dye using

200 mM $NaNO_3$ solution as eluent. The collected vesicles suspension was diluted to 2 mL. Final conditions: ~ 5 mM DPPC; inside: 200 mM $NaNO_3$, 1 mM lucigenin, pH 6.5 using phosphate buffer (10 mm); outside: 200 mM $NaNO_3$, pH 6.5.

Ion transport assay

In a clean and dry fluorescence cuvette, 200 mM of $NaNO_3$ (2890 μL) and DPPC-LUVs⊃lucigenin (40 μL, 109.6 μM) were added. To this suspension either DMF or **4** (0.6 mol%) were added. This suspension was placed in a slowly stirring condition in a fluorescence instrument equipped with a magnetic stirrer (at $t = 0$ s). The fluorescence intensity of lucigenin was monitored at λ_{em} = 535 nm (λ_{ex} = 455 nm) as a course of time by creating a chloride gradiant across the membrane using 2 M NaCl at $t = 50$ s. Finally, vesicles were lysed by adding 10% Triton X-100 (40 μL) at $t = 250$ s for the complete disipation of the chloride gradient. The chloride transport for **4** was monitored at 25 ^{0}C and 45 ^{0}C. Significant chloride transport was observed at 45 ^{0}C with very little changes at 25 ^{0}C. The time-dependent data were normalized to percent change in fluorescence intensity using Equation S1.

V. Stimulus-responsive triggered activation in the solution phase

Assessment of photolysis of protransporter 1a to give 1 upon irradiation at 405 nm: In a clean and dry NMR tube, the solution of **4a** was taken in DMSO-d_6 (1 mM in 0.5 mL). The ^{1}H NMR spectrum of the sample was recorded first ($t = 0$ min). Then, the NMR tube containing the compound **1a** was photoirradiated using 405 nm LED (1W) for different time intervals. The ^{1}H NMR spectrum of the irradiated samples were recorded at the end of each irradiation. All ^{1}H NMR spectra were processed using MestReNova 6.0 by considering the residual solvent peak as an internal reference. Finally, the NMR spectra of **1a** and the photoirradiated samples were stacked and compared with as synthesized **1** (recorded in DMSO-d_6). Upon photoirradiation, the appearance and disappearance of the different proton peak signals of the protransporter **1a** indicated the release of as-synthesized active transporter **1**.

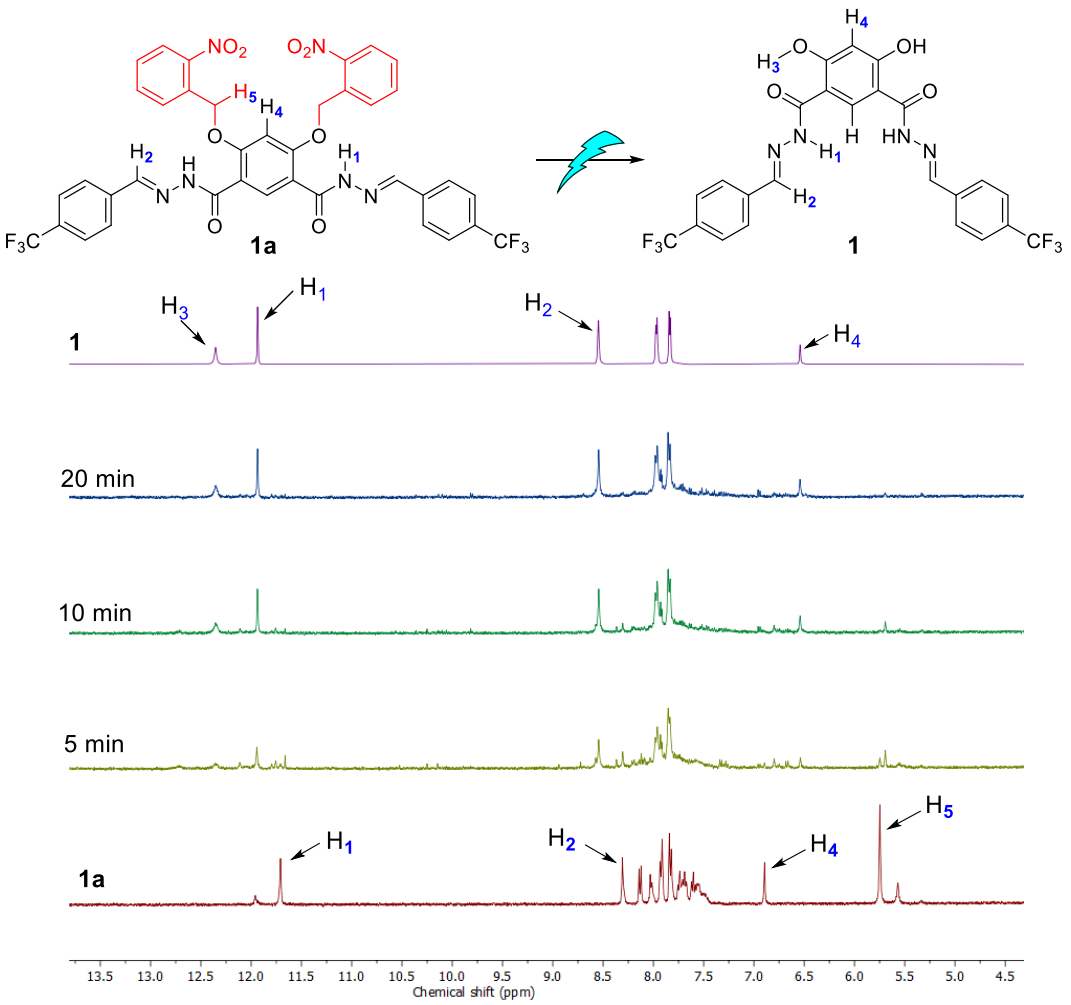

Figure S56. Photo release of active transporter **4** from protransporter upon photoirradiation using 405 nm LEDs (1 W) recorded in DMSO-d_6.

<u>Assessment of photolysis of protransporter 1b to give 1 with H_2S:</u> A stock solution of **1b** (0.2 mM, 2mL) was were prepared in DMF. To this solution, NaSH (10 eq as aqeous solution) was added and kept at 37 °C. At different time intervals 200 µL of this mixture was filtered (Fisher band, PTFE 0.2 uM) and injected in a high-performance liquid chromatography (Thermo Scientific Vanquish Core HPLC). The mobile phase was H_2O/ CH_3CN. The stationary phase was C-18 reverse phase column (Ascentis, 5 µm, 15 cm x 4.6 mm). CH_3CN concentration was increased from 5% to 95% over 7 min and maintained at 95% for another 4 min at a flow rate of 2 mL/min. The formation of active transporter **1** was monitored by a UV detector with excitation at 300 nm. Similarly, pure **1b** and **4** as DMF solutions were also subjected to HPLC analysis. Eventually, Pure **1**, caged **1b**, and decaged traces were staked in Origin2023 (64 bit). The retention time for active transporter **1** and caged protransporter **1b** were found to be 7.44 min and 8.17 min, respectively.

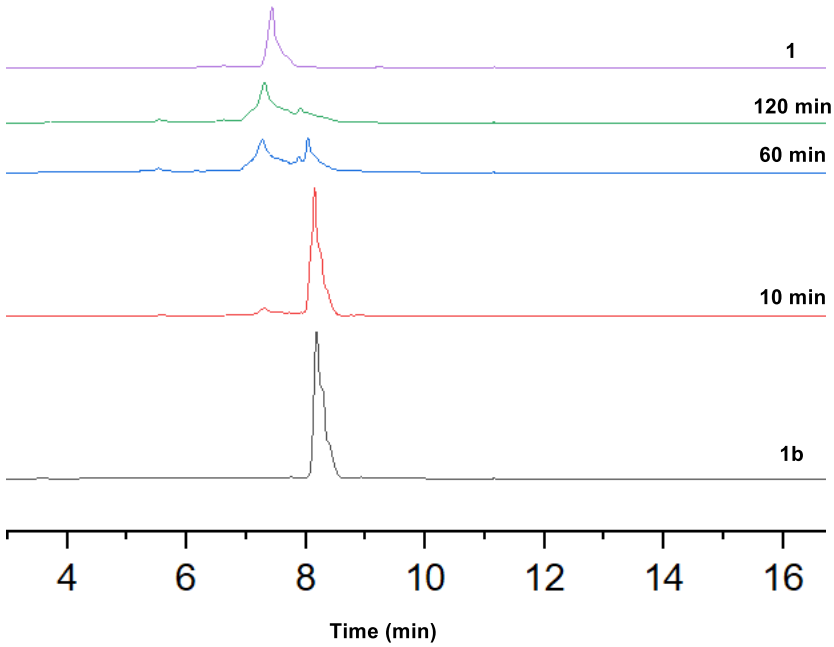

Figure S57. HPLC traces showing the release of **1** by treating **1b** with NaSH.

VI. Stimulus-responsive ion transport activation

Preparation of POPC-LUVs⊃lucigenin vesicles: These vesicles were prepared using the procedure as described above.

Activation with light: In a clean and dry fluorescence cuvette, 200 mM of $NaNO_3$ (2890 µL), POPC-LUVs⊃lucigenin (40 µL, 109.6 µM), and **1a** (0.35 mol%) were taken. The fluorescence intensity of lucigenin was monitored at λ_{em} = 535 nm (λ_{ex} = 455 nm) as a course of time by creating a chloride gradiant across the membrane by adding NaCl at t = 50 s in the external buffer lysed by adding 10% Triton X-100 (40 µL) at t = 250 s for the complete destruction of chloride gradient. Negligible transport activity was observed for **1a**. After that the buffer containing **1a** was initially photoirradiated at 405 nm of light using LEDs and subsequently POPC-LUVs⊃lucigenin (40 µL, 109.6 µM) were added to this photoirradiated cuvette and ion transport was monitored. The same procedure was employed for photoirradiation at different time intervals and at each time vesicles were added after the photoirradiation process.

The time-dependent data were normalized to percent change in fluorescence intensity using Equation S1.

Activation with NaSH: In a clean and dry fluorescence cuvette, 200 mM of $NaNO_3$ (2890 µL), POPC-LUVs⊃lucigenin (40 µL, 109.6 µM), and **1b** (0.35 mol%) were taken. The fluorescence intensity of lucigenin was monitored at λ_{em} = 535 nm (λ_{ex} = 455 nm) as a course of time by creating a chloride gradiant across the membrane by adding NaCl at t = 50 s in the external buffer lysed by adding 10% Triton X-100 (40 µL) at t = 250 s for the complete destruction of chloride gradient. Negligible transport activity was observed for **1b**. Meanwhile, in a separate cuvette NaSH (10.0 eq) was added to **1b** in DMF (57 µM, 2 µL) and 20 µL of this solution at different intervals was added to the fluorescence cuvette containing 200 mM of

$NaNO_3$ (2890 µL) and lucigenin-based vesicles (40 µL, 109.6 µM) and ion transport was monitored each time.

The time-dependent data were normalized to percent change in fluorescence intensity using Equation S1.

VII. Crystallographic studies

General procedure for crystallization

The solution of 1 (10 mg) in DMSO was heated with TBACl salt (05 eq) in a 5 mL of glass vial and then filtered to separate any undissolved component. The solution was then left in a stable place to evaporate slowly. After few days, colourless needle-like crystalline material precipitated from the vial. Suitable crystals were chosen for the X-ray measurement.

X-ray single crystal diffraction analysis

Single crystals suitable for X-ray analysis were coated with perfluoropolyether oil, mounted on a 200 µm MiTeGen loop and placed in a cold nitrogen stream (150 K)[3] on an Oxford Diffraction Supernova X-ray diffractometer. Diffraction intensities were measured using monochromated Cu K_α diffraction. Data collection, indexing, initial cell refinements, frame integration, final cell refinements and absorption corrections were performed using CrysAlisPro. Crystal structures were solved by SuperFlip[4] and refined using the CRYSTALS suite. [5-7] Hydrogen atoms were included into the model at geometrically calculated positions and refined using a riding model.[6] More details are included below and in the accompanying CIF which is part of the supplementary data for this manuscript. This data is also provided free of charge by the joint Cambridge Crystallographic Data Centre and Fachinformationszentrum Karlsruhe Access Structures service www.ccdc.cam.ac.uk/structures with deposition number 2371936-2371937.

Table S1. Selected crystallographic data for reported structures

Compound	**1·TBACl**	**1a**
Formula	$C_{38}H_{29.84}F_6N_6O_{9.92}$	$C_{40}H_{52}ClF_6N_5O_4$
Formula Weight	843.32	816.32
Temp (K)	150	150
Crystal system	triclinic	monoclinic
Space group	*P*-1	$P2_1/n$
a (Å)	7.6159(3)	10.5597(4)
b (Å)	13.8364(7)	10.1486(5)
c (Å)	18.8032(6)	38.667(2)
α	97.114(3)	90
β	100.726(3)	92.415(4)
γ	102.922(3)	90
Cell volume (Å^3)	1868.96(14)	4140.1(3)
Z	2	4
Reflections collected (all)	27879	64452
Reflections (unique)	7743	5946

R_{int}	0.042	0.123
R_1 ($I > 2\sigma(I)$)	0.0557	0.0925
wR_2 (all data)	0.1806	0.2351

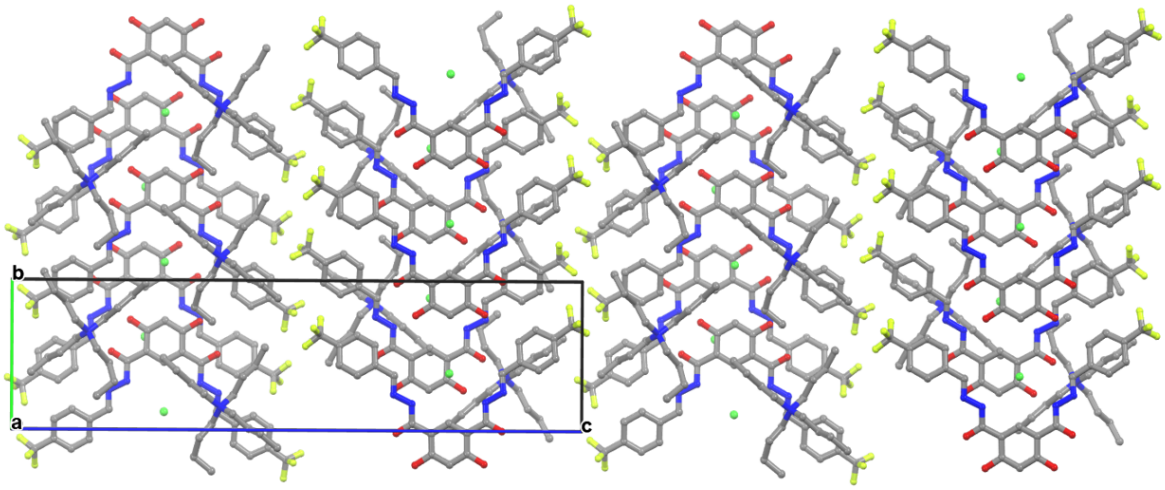

Figure S58. The crystal packing diagram of **1** with TBACl viewing direction of 'a' axis at 100 K.

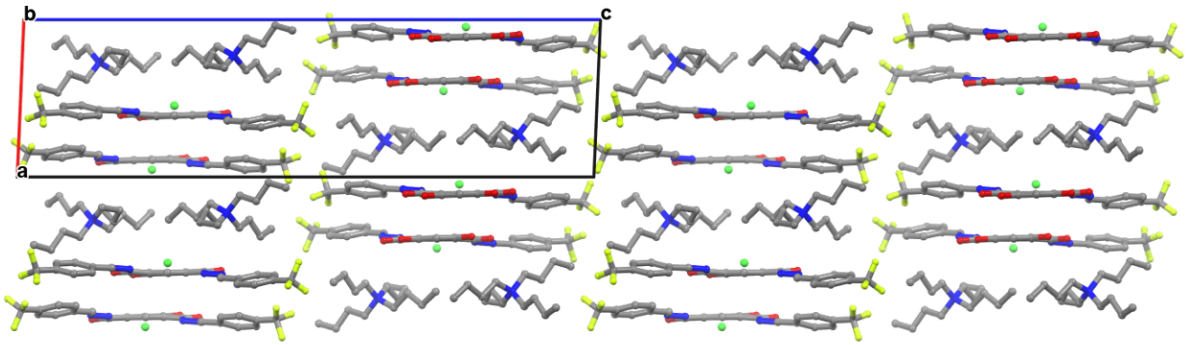

Figure S59. The crystal packing diagram of **1** with TBACl viewing direction of 'b' axis at 100 K.

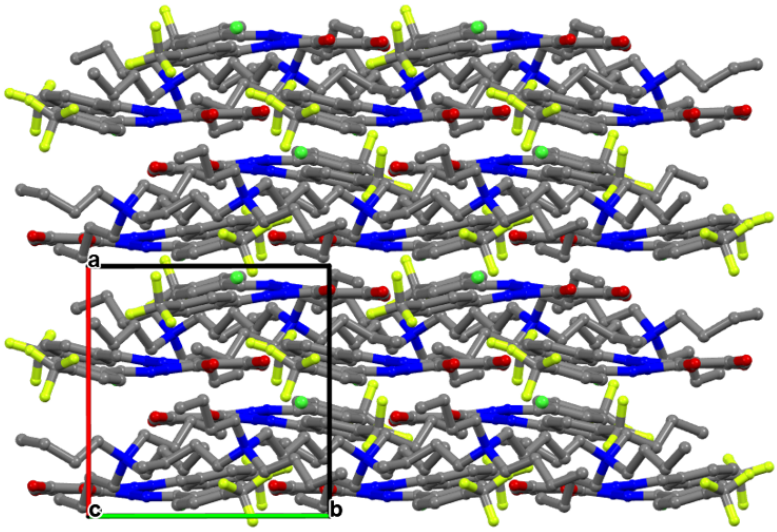

Figure S60. The crystal packing diagram of **1** with TBACl viewing direction of 'c' axis at 100 K.

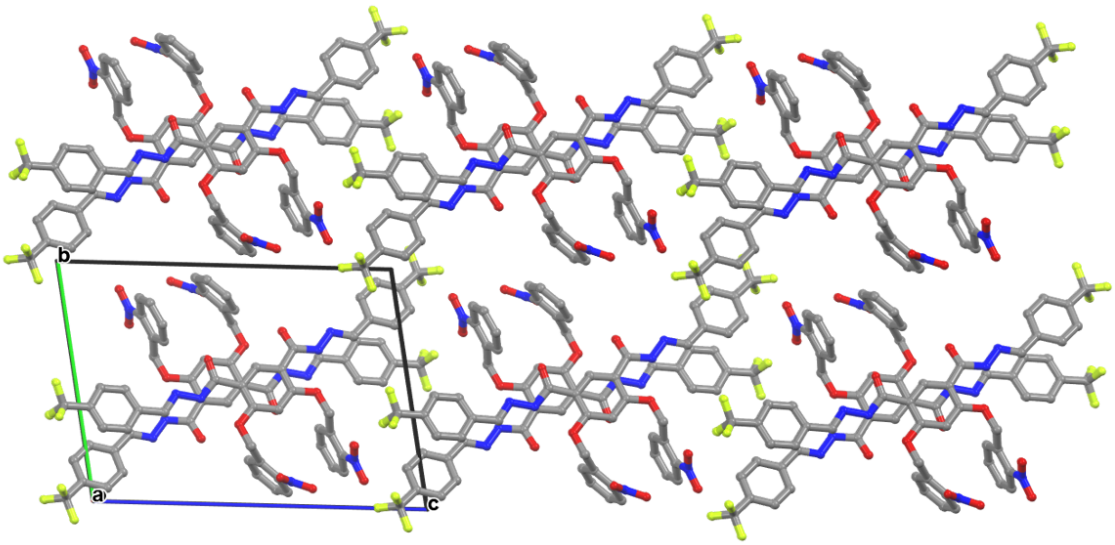

Figure S61. The crystal packing diagram of **1a** viewing direction of 'a' axis at 100 K.

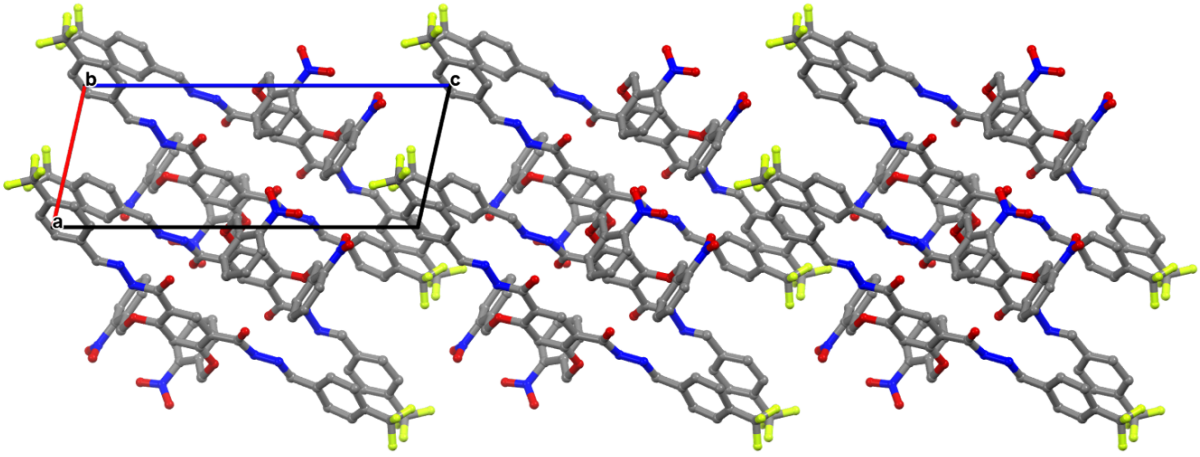

Figure S62. The crystal packing diagram of **1a** viewing direction of 'b' axis at 100 K.

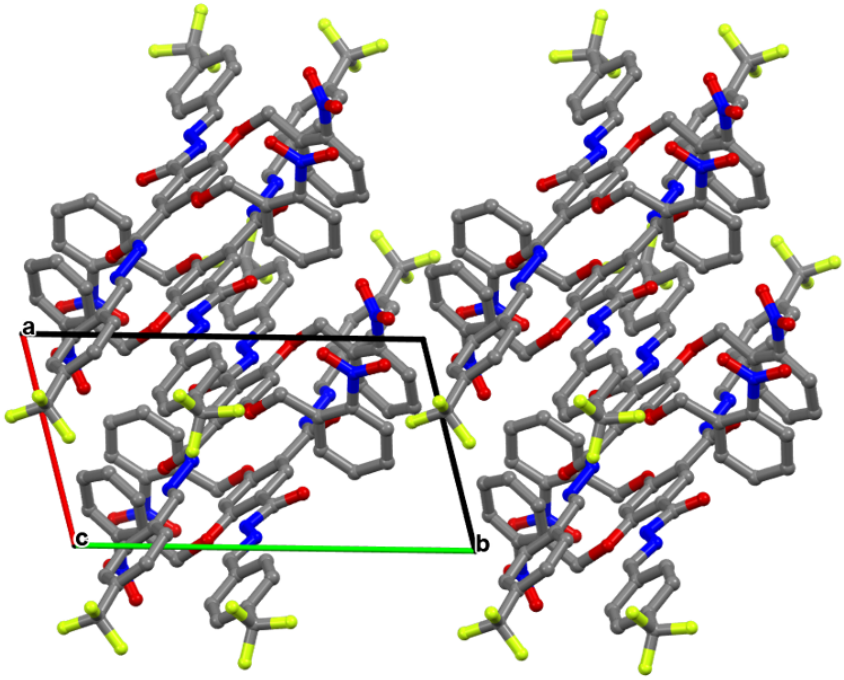

Figure S63. The crystal packing diagram of **1a** viewing direction of 'c' axis at 100 K.

VIII. Computational

DFT Calculations

Starting geometries of transporter **1,** its methyl-capped analogue **1m**, as well as all of their complexes under study were generated in Avogadro (version 1.20), and optimised using the built-in General Amber Force-Field, followed by optimisation using XTB (version 6.4.1).[8-10] A conformer search was carried out using the CREST program (version 2.11) in NCI mode using the default metadynamics parameters, with the lowest energy conformer being used as the input for the calculations described hereafter. [11]

Optimisations and energy calculations were carried out with the ORCA suite of programs (version 5.0.3).[12, 13] Lowest energy conformers were optimised at the CPCM(DMSO)-ωB97X-D3/def2-SVP level of theory, referred here to as Low-Level (**LL**), followed by a frequency calculation at the same level.[14-17] This level of theory has previously been shown to perform well in capturing the energetics of hydrogen bonding interactions.[18, 19] Very tight convergence criteria were employed ($2 * 10^{-7}$ Ha for the optimisation step and 10^{-8} Ha for the SCF energy change). The resolution of identity approximation and chain of sphere integration (RIJCOSX keyword) were used to speed up calculations, using the default auxiliary basis sets.[20] Thermochemistry was calculated using the *otherm* program, using the default quasi-RRHO approximation (ω_0 = 45 cm^{-1}, α = 4, T = 298.15 K).[21] By default, the *otherm* programme corrects the standard state from 1 atm to 1 M, which adds 1.89 kcal mol^{-1} (equivalent to RT·ln(1 mol dm^{-3}/ (1/24.5 mol dm^{-3}))) e.g. [$G_{HL,1M} = G_{HL,1atm} + RTln(24.5)$]. Single point energies at a higher level (HL) were calculated at the CPCM(DMSO)-ωB97X-D3/def2-QZVP

level of theory. In order to approximate the free energies at this level, the thermodynamic contributions from the **LL** level were added to the single point energies at the **HL** level, i.e. $G_{HL} = E_{HL} + (G_{LL} - E_{LL})$. The binding interaction is then calculated as the energy difference of the complex (**1** bound to Cl^- or DMSO) and the energy of the separated **1** and Cl^-/DMSO. To ascertain that there was no significant effect upon addition of diffuse orbitals and change of solvation model from CPCM to SMD, both of which increase the cost of computations, we carried out a small benchmarking study, calculating electronic energies of binding for **1** with Cl^- by carrying out single point calculations on geometries optimised with the **LL** level of theory.[22] **HL** (vide supra) is the standard method we used in the study, **HL_SMD** uses the SMD solvation model instead of the CPCM, **HL_ma** uses the minimally augmented diffuse ma-def2-QZVP basis set instead of the standard def2-QZVP, and **HL_comb** uses both of these additions. Figure **S64** compares the results of all four combinations and shows that there is little impact on the electronic binding energies from increasing the cost of the calculations by employing the more expensive solvation model or the bigger basis set, and no changes at all in the electronic binding energies when both are used in conjunction.

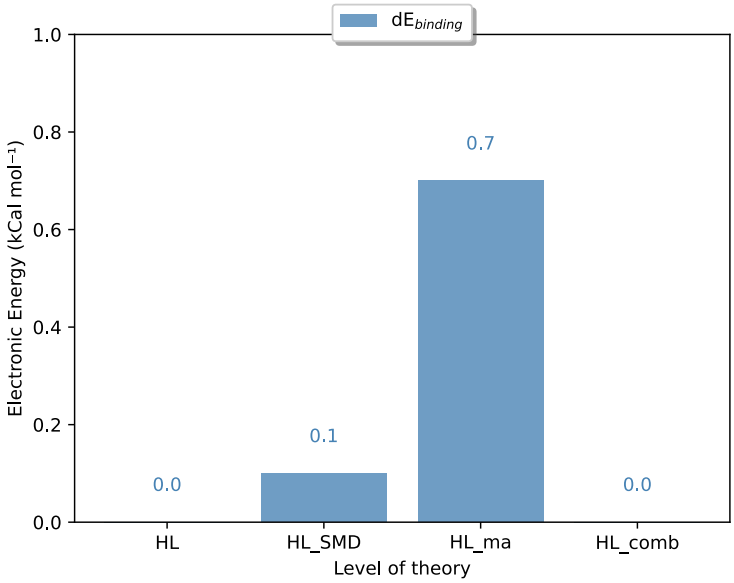

Figure S64: Benchmarking of CPCM and SMD solvation models, as well as the diffuse ma-def2-QZVP basis sets, on the binding process of **1** + $Cl^- \rightarrow [\mathbf{1}\cdot Cl]^-$. The structure of unbound **1** optimised at the **LL** level of theory (the CPCM(DMSO)-ωB97X-D3/def2-SVP), with energy calculations subsequently carried out at the **HL** (CPCM(DMSO)-ωB97X-D3/def2-QZVP), **HL_SMD** (SMD(DMSO)-ωB97X-D3/def2-QZVP), **HL_ma** (CPCM(DMSO)-ωB97X-D3/ma-def2-QZVP), **HL_comb** (SMD(DMSO)-ωB97X-D3/ma-def2-QZVP). All energies are displayed relative to the binding energy at the **HL** level of theory.

Analysis of Complex Interactions

In order to probe both the intra- and inter-molecular interactions of **1** and **1m**, we carried out additional second order perturbation analysis on the final structures of the unbound structures,

as well as complexes [**1**·Cl]⁻, [**1**·DMSO] and [**1m**·Cl]⁻, which gives interaction energies $E^{(2)}$. This was carried out at the **HL** level of theory using NBO 7.0 wrapped in ORCA, using the structures optimised at the **LL** level of theory.[23] The key interactions are summarised in Figure **S65**.

Additionally, in order to ascertain the balance between stabilising and destabilising interactions in all of the studied complexes, distortion interaction analysis was carried out by carrying out single point calculations on the geometries of [**1**·Cl]⁻, [**1**·DMSO] and [**1m**·Cl]⁻, with the host removed.[24] The difference between the energies of the complex in its bound pose and its minimal energy pose is the distortion energy, and quantifies how much energy must be input into the reorganisation of the molecule in order for an interaction to take place (see Figure **8**). The difference between this distortion energy and the overall binding energy is then the interaction energy, which shows how strongly the molecule is able to interact with its guest in its bound conformation.

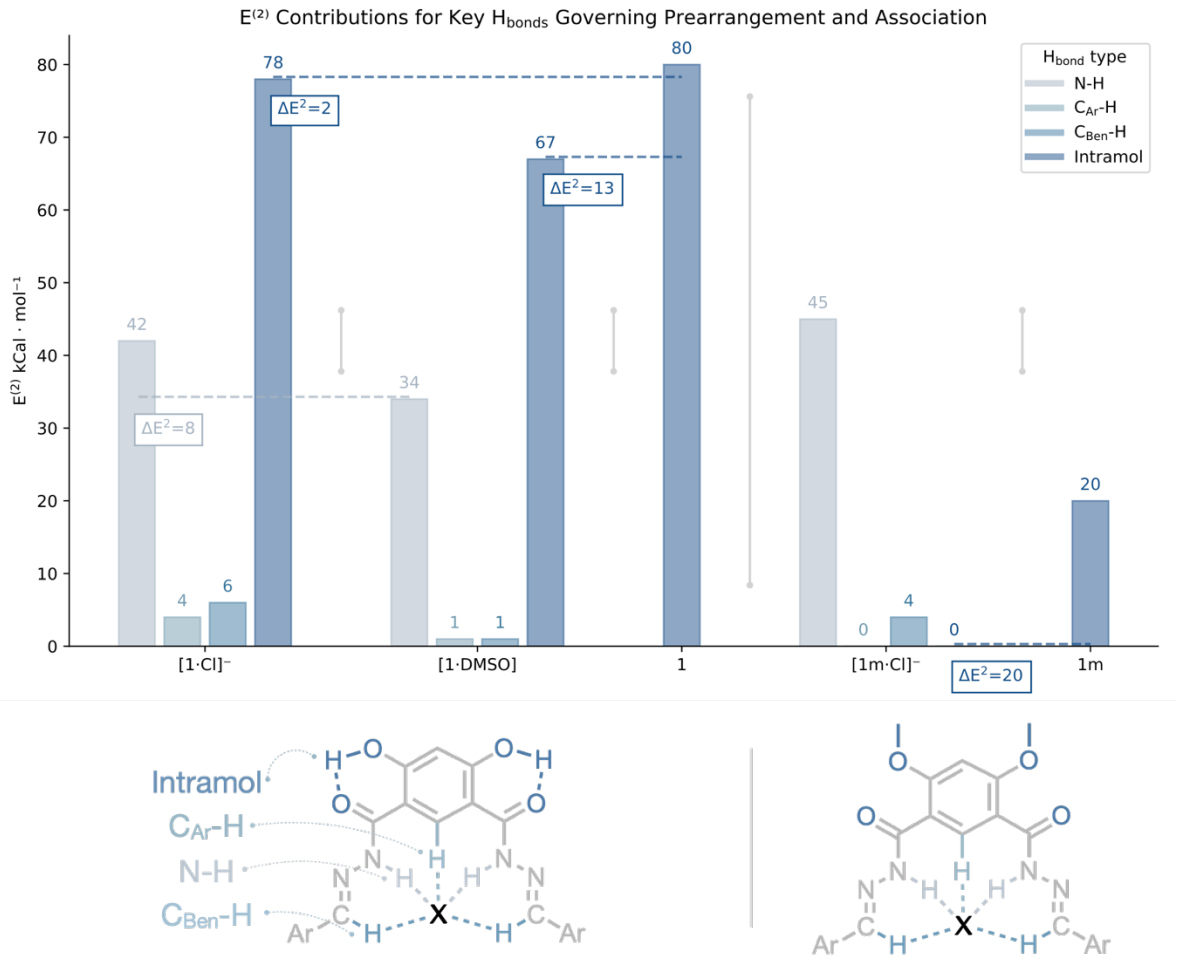

Figure S65: Analysis of the key intra- and inter-moleculer interactions for **1** and **1m** as well as their relevant complexes with X (where X is DMSO or Cl^-), from second order perturbation analysis carried out in NBO. The legend shows the hydrogen bond donors for each interaction.

Energy details of Calculations

Table S2. Complete details of computational calculations, including electronic energy (E_{el}), the zero point energy correction (ZPE), enthalpy (H), quasi-RRHO entropy contribution at 298.1 K (Tqh-S) and the total correction to the electronic energy giving the quasi-RRHO Gibbs free energy (qh-G) calculated at the CPCM(DMSO)-ωB97X-D3/def2-SVP level of theory (**LL**) or CPCM(DMSO)-ωB97X-D3/def2-QZVP// ωB97X-D3/def2-SVP level of theory (**HL**/**LL**). Free energies were calculated at 298.1K and 1M.

	LL						**HL/LL**	
Species	E_{el}	ZPE	H	Tqh-S	Total Corr	qh-G	E_{el}	qh-G
Cl^-	-460.20444	0	-460.20066	0.01438387	-0.0106071	-460.21505	-460.40698	-460.41758
DMSO	-552.90947	0.07986371	-552.82315	0.0316145	0.05471136	-552.85476	-553.28177	-553.22706
1	-2041.168	0.383804	-2040.751	0.093827	0.323318	-2040.845	-2043.573	-2043.25
[**1**·Cl]-	-2501.4152	0.38519313	-2500.9951	0.09727415	0.32284437	-2501.0923	-2503.994	-2503.6712
[**1**·Cl]-	-2041.1671	0.38437994	-2040.7499	0.09253524	0.32465405	-2040.8425	-2043.5717	-2043.2471
[**1**·DMSO]	-2594.1122	0.46656637	-2593.6059	0.10711392	0.39927832	-2593.713	-2596.8747	-2596.4754
[**1**·DMSO] distorted	-2041.1657	0.38377319	-2040.7487	0.09364659	0.323269	-2040.8424	-2043.5708	-2043.2476
1m	-2119.6769	0.43986622	-2119.2001	0.10193909	0.37493069	-2119.302	-2122.1656	-2121.7907
[**1m**·Cl]-	-2579.9086	0.44023261	-2579.4294	0.10673843	0.37247352	-2579.5361	-2582.5774	-2582.2049
[**1m**·Cl]- distorted	-2119.6633	0.43945403	-2119.187	0.10144144	0.37483056	-2119.2885	-2122.1564	-2121.7816

Table S3. Complete details of computational calculations, including electronic energy (E_{el}), the zero point energy correction (ZPE), enthalpy (H), quasi-RRHO entropy contribution at 298.1 K (Tqh-S) and the total correction to the electronic energy giving the quasi-RRHO Gibbs free energy (qh-G) calculated at the CPCM(DMSO)-ωB97X-D3/def2-SVP level of theory (**LL**) or CPCM(DMSO)-ωB97X-D3/def2-QZVP// ωB97X-D3/def2-SVP level of theory (**HL**/**LL**). Free energies were calculated at 298.1K and 1M.

	LL						**HL/LL**	
Process	E_{el}	ZPE	H	Tqh-S	Total Corr	qh-G	E_{el}	qh-G
1 + Cl^- → [**1**·Cl]$^-$	-26.7	0.9	-27.2	-6.9	6.4	-20.3	-8.8	-2.5
[**1**·Cl]- Binding Distortion	0.7	0.4	0.7	-0.8	0.8	1.5	0.8	1.6
1 + DMSO- → [**1**·DMSO]-	-21.7	1.8	-19.9	-11.5	13.3	-8.4	-12.5	0.8
[**1**·DMSO] Binding Distortion	1.6	0.0	1.5	-0.1	0.0	1.6	1.4	1.3
[**1**·DMSO] + Cl^- → [**1**·DMSO] + Cl^-	-5.0	-0.9	-7.3	4.6	-7.0	-12.0	3.7	-3.3
[**1**·Cl]$^-$ from [**1**·DMSO] Binding Distortion	-0.9	0.4	-0.7	-0.7	0.9	0.0	-0.6	0.3
1m + Cl^- → [**1m**·Cl]-	-17.1	0.2	-18.0	-6.0	5.1	-12.0	-3.0	2.1
[**1m**·Cl]- Binding Distortion	8.6	-0.3	8.2	-0.3	-0.1	8.5	5.7	5.7

DFT Minimal Geometries

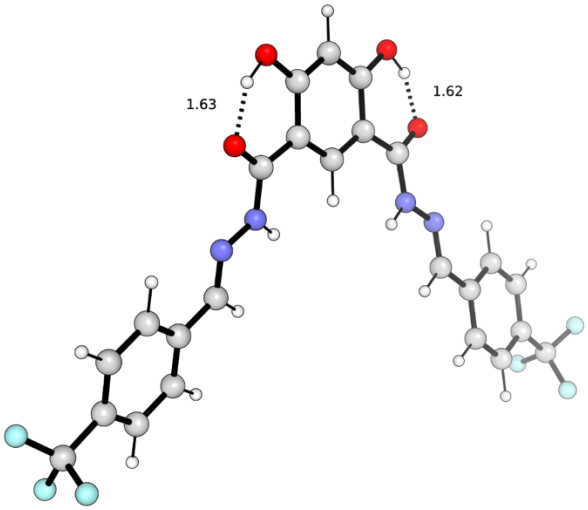

Figure S66: Structure of the minimal energy conformer of unbound **1** optimised at the **LL** level of theory.

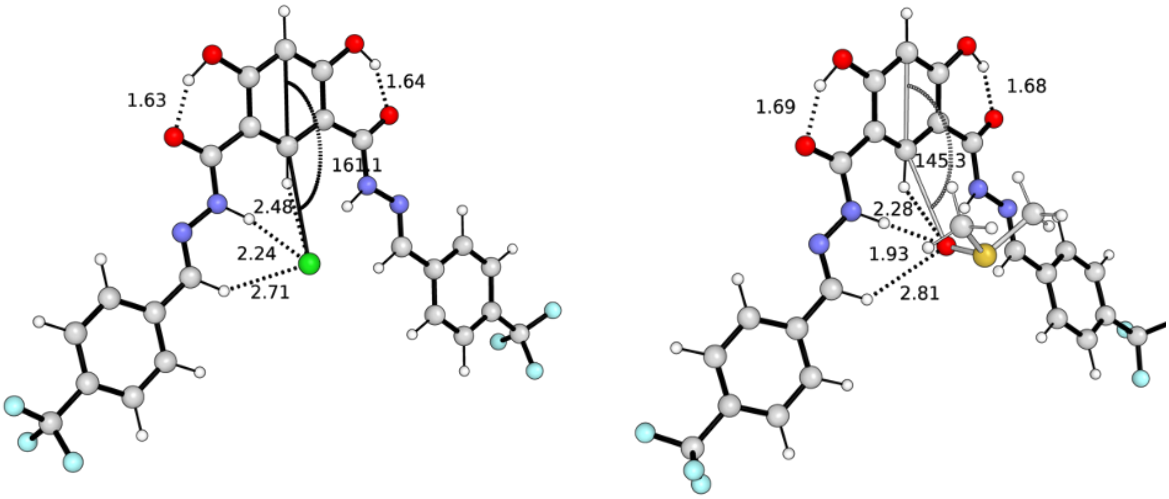

Figure S67: Left: Structure of the minimal energy conformer of the [**1***Cl]$^-$ complex optimised at the **LL** level of theory. Right: Structure of the minimal energy conformer of the [**1***DMSO] complex optimised at the **LL** level of theory.

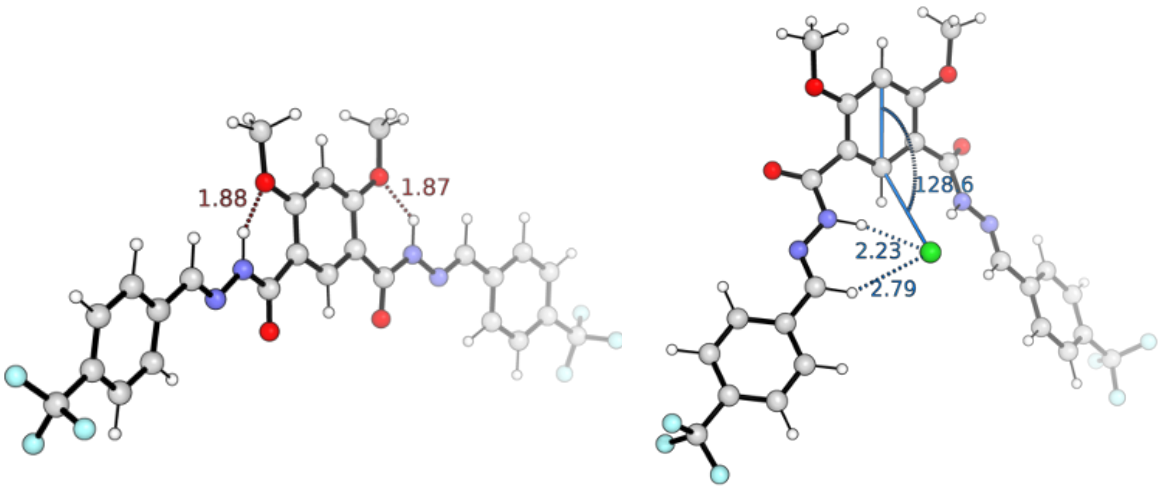

Figure S68: Left: Structure of the minimal energy conformer of unbound **1m** phenol protected analogue of **1**, optimised at the **LL** level of theory. Right Structure of the minimal energy conformer of phenol protected complex [**1m***Cl]$^-$ optimised at the **LL** lower of theory.

Molecular Dynamics Simulations

The minimal energy structure optimised in ORCA at the **LL** level of theory was used as the starting point for the electrostatic potential calculation, which was carried out in Gaussian 09 at the HF/6-31G* level of theory, using the Merz-Singh-Kollman scheme for charge calculation with 6 density points in each layer (IOp(6/33=2, 6/42=6, 6/50=1)).[25-29] RESP fitting was then employed using the antechamber suite, alongside the assignment of GAFF atom types, and the parameters converted into the GROMACS format.[10, 30] Simulations were carried out in the GROMACS simulation software package (v.2021.3 in all subsequent mentions).[31] DMSO parameters were taken from Caleman et al, with chloride parameters taken from Li et al, and default AMBER parameters for sodium.[32, 33]

The structure of [**1**·Cl]$^-$, **1** or **1m** was inserted into a cubic box with a 1 nm buffer to the edge of the box and solvated with DMSO. The system was then neutralised with the insertion of a single sodium ion in the case of [**1**·Cl]$^-$. The systems were minimised using a steepest descent algorithm until the maximum force in the system was below 1000 kJ mol^{-1}. For the unbiased simulations, 500 ps of equilibration in the NPT ensemble (2 fs timestep, 298 K, 1 bar) staring from random velocities sampled from the Maxwell-Boltzmann distribution was followed by 100 ns of NPT production simulations (2 fs timestep, 298 K, 1 bar).

Umbrella sampling was then conducted on [**1**·Cl]$^-$ by altering the distance between the chloride ion and the centre of mass of both sets of N-N-C and H atoms of the hydrazide functionality

on the transporter. The windows were spaced in increments of 1 Å, from 3 to 13. Three repeats of umbrella sampling runs were carried out for each umbrella sampling window, with 500 ps of equilibration in the NPT ensemble (2 fs timestep, 298 K, 1 bar) staring from random velocities sampled from the Maxwell-Boltzmann distribution, followed by 100 ns of NPT production simulations (2 fs timestep, 298 K, 1 bar). Long-range electrostatics were described with the Particle Mesh Ewald (PME) algorithm.[34] Temperature of the system was maintained at 298 K using the V-rescale thermostat.[35] Pressure was controlled by the C-rescale barostat at 1.0 bar, with an isothermal compressibility of $4.5 \cdot 10^{-5}$ bar^{-1}.[36] All bond lengths involving hydrogen atoms were constrained using the LINCS algorithm.[37]

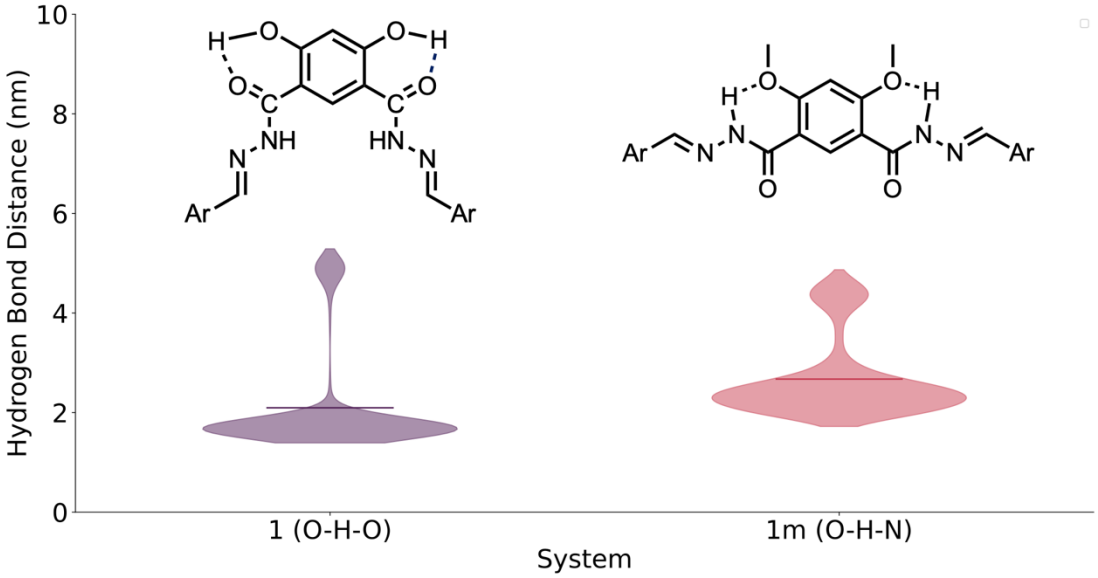

Figure S69: Violin plot showing the distribution of intramolecular HB distances in 1 (O-H-O, left) and 1m (O-H-N, right) from 200 ns of unbiased MD simulations in DMSO.

The first 10 ns of each umbrella sampling window was discarded, and convergence was monitored in increments of 10 ns from this 10 ns starting point using the GROMACS wham utility, which carries out weighted histogram analysis.[38] All of the three repeats of each window were then analysed together from 50 ns to 100 using bootstrapping analysis with 100 bootstraps to give an estimate of the uncertainty. Finally, the entropy uncorrected energy profile in Figure S69 was corrected to account for the entropy loss of distance restrictions, equal to 2*Kb*T*Ln(r), where Kb is the Boltzmann constant, T is equal to 298 K and r is the distance from the binding site.

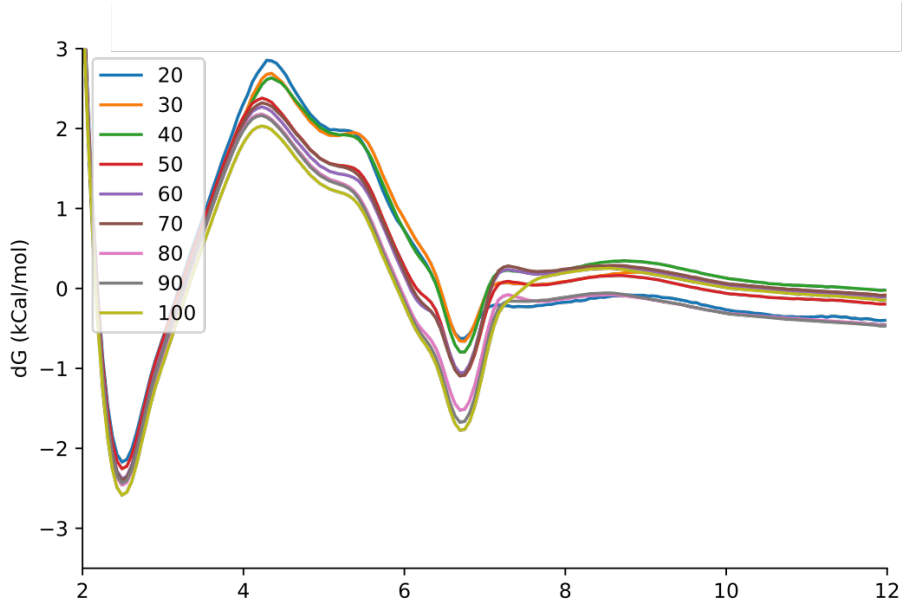

Figure S70: Convergence analysis of the US simulations from 10 ns onwards, in increasing increments of 10 ns, with the line colour indicating the end-point of the wham analysis (e.g. at 100 ns this indicates the whole 10-100 ns).

Free energy perturbation calculations were carried out by performing a thermodynamic cycle of slowly switching on the Van Der Waals and Coulumbic interactions of the chloride ion in DMSO, as well as those same interactions of a chloride ion bound to **1** in DMSO, with the number of DMSO molecules remaining constant in both cases, and the cubic boxes containing a 1 nm buffer between the walls and solute.[39] The Van Der Waals interaction lambda values were turned on in increments of 0.1 first, followed by Coulombic interactions, with the same increment size. Each window was run for a total of 10 ns staring from a pre-equilibrated structure Cl^- in DMSO, or of $[\mathbf{1}\cdot Cl]^-$ in DMSO in the case of the complex, and subsequently the 21 windows of each system with different lambda values were analysed using the BAR utility of GROMACS, with the energies of both processes of turning on Cl^- interactions as well as their uncertainties summarised in Table **S4**. [40]

Table S4. Summary of the energies obtained from the BAR analysis of turning on Cl^- interactions in DMSO only and in DMSO, while bound to 1. The difference between the two is obtained as the binding. All values are presented with the associated uncertainties.

Process	dG (kcal mol^{-1})	Uncertainty (kcal mol^{-1})
Cl^- appearance in DMSO	-70.3	± 0.2
Cl^- appearance with 1 in DMSO	-74.6	± 0.9
Binding	-3.3	± 1.1

IX. References

1. B. Chen, P. Wang, Q. Jin and X. Tang, *Org. Biomol. Chem.*, 2014, **12**, 5629-5633.
2. http://app.supramolecular.org/bindfit/,
3. J. Cosier and A. M. Glazer, *J. Appl. Cryst*, 1986, **19**, 105-107.
4. L. P. a. G. Chapuis, *J. Appl. Cryst.*, 2007, **40**, 786-790.
5. P. W. Betteridge, J. R. Carruthers, R. I. Cooper, K. Prout and D. J. Watkin, *J. Appl. Cryst.*, 2003, **36**, 1487-1487.
6. P. Parois, R. I. Cooper and A. L. Thompson, *Chem. Cent. J.*, 2015, **9**, 30.
7. A. L. T. D. J. W. R. I. Cooper, *J. Appl. Cryst.*, 2010, **43**, 1100-1107.
8. C. Bannwarth, S. Ehlert and S. Grimme, *J. Chem. Theory Comput.* 2019, **15**, 1652-1671.
9. M. D. Hanwell, D. E. Curtis, D. C. Lonie, T. Vandermeersch, E. Zurek and G. R. Hutchison, *J Cheminform*, 2012, **4**, 17.
10. J. Wang, R. M. Wolf, J. W. Caldwell, P. A. Kollman and D. A. Case, *J. Comput. Chem*, 2004, **25**, 1157-1174.
11. S. Grimme, *J. Chem. Theory Comput.*, 2019, **15**, 2847-2862.
12. F. Neese, *WIREs Comput Mol Sci,*, 2012, **2**, 73-78.
13. F. Neese, *WIREs Comput Mol Sci.*, 2022, **12**, e1606.
14. V. Barone and M. Cossi, *J. Phys. Chem. A*, 1998, **102**, 1995-2001.
15. J.-D. Chai and M. Head-Gordon, *Phys. Chem. Chem. Phys.*, 2008, **10**, 6615-6620.
16. Y.-S. Lin, G.-D. Li, S.-P. Mao and J.-D. Chai, *J. Chem. Theory Comput.*, 2013, **9**, 263-272.
17. F. Weigend and R. Ahlrichs, *Phys. Chem. Chem. Phys.*, 2005, **7**, 3297-3305.
18. L. E. Bickerton and M. J. Langton, *Chem. Sci.*, 2022, **13**, 9531-9536.
19. A. D. Boese, *ChemPhysChem*, 2015, **16**, 978-985.
20. F. Neese, F. Wennmohs, A. Hansen and U. Becker, *Chem. Phys*, 2009, **356**, 98-109.
21. d. o. v.-b. Z. T. Young.
22. A. V. Marenich, C. J. Cramer and D. G. Truhlar, *J. Phys. Chem. B*, 2009, **113**, 6378-6396.
23. E. D. Glendening, C. R. Landis and F. Weinhold, *J. Comput. Chem.*, 2013, **34**, 1429-1437.
24. F. M. Bickelhaupt and K. N. Houk, *Angew. Chem. Int. Ed.* , 2017, **56**, 10070-10086.
25. R. Ditchfield, W. J. Hehre and J. A. Pople, *J. Chem. Phys.*, 1971, **54**, 724-728.
26. G. W. T. S10 M. J. Frisch, H. B. Schlegel, G. E. Scuseria, M. A. Robb, J. R. Cheeseman, G. Scalmani, V. Barone, B. Mennucci, G. A. Petersson, H. Nakatsuji, M. Caricato, X. Li, H. P. Hratchian, A. F. Izmaylov, J. Bloino, G. Zheng, J. L. Sonnenberg, M. Hada, M. Ehara, K. Toyota, R. Fukuda, J. Hasegawa, M. Ishida, T. Nakajima, Y. Honda, O. Kitao, H. Nakai, T. Vreven, J. A. Montgomery, J. E. Peralta, F. Ogliaro, M. Bearpark, J. J. Heyd, E. Brothers, K. N. Kudin, V. N. Staroverov, T. Keith, R. Kobayashi, J. Normand, K. Raghavachari, A. Rendell, J. C. Burant, S. S. Iyengar, J. Tomasi, M. Cossi, N. Rega, J. M. Millam, M. Klene, J. E. Knox,

J. B. Cross, V. Bakken, C. Adamo, J. Jaramillo, R. Gomperts, R. E. Stratmann, O. Yazyev, A. J. Austin, R. Cammi, C. Pomelli, J. W. Ochterski, R. L. Martin, K. Morokuma, V. G. Zakrzewski, G. A. Voth, P. Salvador, J. J. Dannenberg, S. Dapprich, A. D. Daniels, O. Farkas, J. B. Foresman, J. V. Ortiz, J. Cioslowski, D. J. Fox, ,Gaussian 09, Revision B.01, Gaussian, Inc., Wallingford, CT, , 2010.

27. C. C. J. Roothaan, *Rev. Mod. Phys.*, 1951, **23**, 69-89.
28. U. C. Singh and P. A. Kollman, *J. Comput. Chem.*, 1984, **5**, 129-145.
29. J. Wang, P. Cieplak and P. A. Kollman, *J. Comput. Chem.*, 2000, **21**, 1049-1074.
30. D. A. Case, H. M. Aktulga, K. Belfon, D. S. Cerutti, G. A. Cisneros, V. W. D. Cruzeiro, N. Forouzesh, T. J. Giese, A. W. Götz, H. Gohlke, S. Izadi, K. Kasavajhala, M. C. Kaymak, E. King, T. Kurtzman, T.-S. Lee, P. Li, J. Liu, T. Luchko, R. Luo, M. Manathunga, M. R. Machado, H. M. Nguyen, K. A. O'Hearn, A. V. Onufriev, F. Pan, S. Pantano, R. Qi, A. Rahnamoun, A. Risheh, S. Schott-Verdugo, A. Shajan, J. Swails, J. Wang, H. Wei, X. Wu, Y. Wu, S. Zhang, S. Zhao, Q. Zhu, T. E. Cheatham, III, D. R. Roe, A. Roitberg, C. Simmerling, D. M. York, M. C. Nagan and K. M. Merz, Jr., *J. Chem. Inf. Model.*, 2023, **63**, 6183-6191.
31. A. Lindahl, Hess and van der Spoel, GROMACS 2021.3 Source code (version 2021.3) Zenodo 2021.
32. C. Caleman, P. J. van Maaren, M. Hong, J. S. Hub, L. T. Costa and D. van der Spoel, *J. Chem. Theory Comput.*, 2012, **8**, 61-74.
33. P. Li, L. F. Song and K. M. Merz, Jr., *J. Phys. Chem. B*, 2015, **119**, 883-895.
34. T. Darden, D. York and L. Pedersen, *J. Chem. Phys.*, 1993, **98**, 10089-10092.
35. G. Bussi, D. Donadio and M. Parrinello, *J. Chem. Phys.*, 2007, **126**, 014101.
36. M. Bernetti and G. Bussi, *J Chem Phys*, 2020, **153**, 114107.
37. B. Hess, Bekker, H., Berendsen, H. J. C., & Fraaije, J. G. E. M., *J. Comput. Chem.* , 1997, **18**, 1463-1472.
38. J. S. Hub, B. L. de Groot and D. van der Spoel, *J. Chem. Theory Comput.*, 2010, **6**, 3713-3720.
39. R. W. Zwanzig, *J. Chem. Phys.*, 1954, **22**, 1420-1426.
40. C. H. Bennett, *J. Comput. Phys.*, 1976, **22**, 245-268.